Synthesis and characterization of vanadium disulfide nanosheets and carbonized iron cations adsorbed onto polyaniline for high-perfomance supercapacitor applications

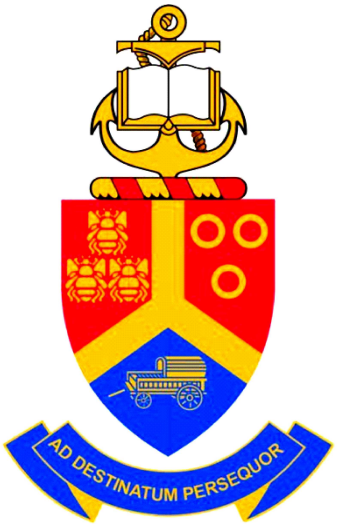

by

Mologadi Nkiyasi Rantho

Submitted in partial fulfilment of the requirements for the degree

Master of Science

in the Department of Physics

in the Faculty of Natural and Agricultural Sciences

University of Pretoria

Pretoria

Supervisor: Prof. N. Manyala

November 2017

University of Pretoria, Pretoria 0028, South Africa

Declaration

I hereby declare that the matter embodied in this thesis, *Synthesis and characterization of vanadium disulfide nanosheets and carbonized iron cations adsorbed onto polyaniline for high-perfomance supercapacitor applications*, is the result of investigations carried out by me under the supervision of Prof. N. Manyala, in the Physics department at the University of Pretoria South Africa and that it has not been submitted elsewhere for the award of any degree or diploma. In keeping with the general practice in reporting scientific observations, due acknowledgement has been made whenever the work described is based on the findings of other investigators.

SIGNATURE STUDENT:..... DATE:.....

Dedication

This thesis is dedicated to my late parents, may the Lord rest their souls in peace. I also dedicate it to all my sisters for their support especially Matshipu Rantho,and for all they provided to help me to achieve this in my life.

Acknowledgements

I would like to express my deep and sincere gratitude to my supervisor Prof. N. Manyala for his effort to ensure the quality of this work, which included innovative suggestions and positive criticisms. His continuous motivation, moral support and parental guidance have been of immense importance.

Many thanks to the sponsors for financial support. This study was sponsored by the South African Research Chairs Initiative of the Department of Science and Technology, National Research Foundation (NRF) of South Africa (Grant No. 97994) and the financial support from the University of Pretoria.

My sincere thanks to Dr. M.J. Madito at the University of Pretoria for proofreading manuscripts and thesis. My sincere thanks to the entire Microscopy centre at the University of Pretoria.

I would like to express my appreciation to Prof. N. Manyala's group members at the University of Pretoria for the assistance, support and useful discussions.

Lastly, I would like to thank my brother, and my sisters for their

encouragements, moral support, love and prayers.

Kind regards

Mologadi Nkiyasi Rantho

Abstract

Due to an urgent need for efficient, clean, and sustainable sources of energy, as well as new technologies associated with energy conversion and storage, the most effective and practical technologies for electrochemical energy conversion and storage are batteries, fuel cells, and electrochemical supercapacitors. In recent years, there have been a large number of research articles and technical reports on the development of electrochemical supercapacitors, motivated by their low energy density and high production cost. Consequently, research focus in supercapacitors is on improving the energy density (i.e. $\approx$5-8 Wh kg^{-1}) without compromising its high power density (i.e. $\approx$5-30 kW kg^{-1}).

In this work, the electrochemical properties of both vanadium disulfide (VS_2) and carbonized iron cations adsorbed onto polyaniline (C-Fe/PANI) electrode materials were investigated for supercapacitor applications. The VS_2 nanosheets electrode material was successfully synthesized by the hydrothermal method, and the C-Fe/PANI electrode material was directly synthesized on a current collector by pyrolysis of the iron-PANI mixture coated on nickel foam in a tube furnace under the N_2 atmosphere. The structural

and morphological characterization of the as-synthesized electrode materials was carried out using X-ray diffraction (XRD), Raman spectrometer, Fourier transform infrared (FT-IR) spectrometer, scanning electron microscopy (SEM), energy-dispersive X-ray spectrometer (EDS), transmission electron microscopy (TEM) and X-ray photoelectron spectroscopy (XPS).

The electrochemical behavior of the C-Fe/PANI electrode was analyzed in both positive and negative potential window in a three-electrode cell configuration using 6 M KOH electrolyte, and thereafter, a C-Fe/PANI symmetric device was successfully fabricated. The C-Fe/PANI symmetric device was found to perform at a high cell voltage of 1.65 V in 6 M KOH. At a current density of 0.5 A g^{-1}, this device exhibited a maximum energy and power densities of 41.3 Wh kg^{-1} and 231.9 W kg^{-1} respectively. The device further showed excellent cycling stability with capacity retention of 72% at a current density of 5 A g^{-1} over 10 000 galvanostatic charge-discharge cycles.

To further evaluate the electrochemical performance of C-Fe/PANI with a metal disulfide material (VS_2), a hybrid (asymmetric) device was successfully fabricated using VS_2 nanosheets as the positive electrode and C-Fe/PANI as a negative electrode. Similarly, the electrochemical behavior of each working electrode was analyzed in a three-electrode cell configuration using 6 M KOH electrolyte, and thereafter, a hybrid (asymmetric) device was successfully fabricated using VS_2 nanosheets as the positive electrode and C-Fe/PANI as a negative electrode. The fabricated VS_2//C-Fe/PANI asymmetric device was

found to perform at a high cell voltage of 1.7 V in 6 M KOH. At a current density of 2 A g^{-1}, this device exhibited high energy and power densities of 27.8 Wh kg^{-1} and 2991.5 W kg^{-1} respectively. In addition, a VS_2//C-Fe/PANI device showed excellent cycling stability with 95% capacity retention over 10 000 galvanostatic charge-discharge cycles at a current density of 5 A g^{-1}.

Table of Contents

List of Figures

List of Tables

PART I

INTRODUCTION

Chapter 1

Introduction

1.1 Background and general motivation

Due to high energy consumption and depleting natural resources globally, the world economy is engaged in the transition to alternative energy to meet the increasing energy demand for the socio-economic development of the society. The need is to:

(i) Urgently adopt sustainable energy generation/resource management that is ecologically beneficial and healthy for present and future generations.

(ii) Move away from the fossil fuels (stop burning carbon in fossil fuels into the atmosphere with its harmful environmental and public health consequences).

Nonrenewable energy sources (natural energy sources) are unsustainable because sooner or later they will run out hence we cannot sustain our reliance on them indefinitely, in fact, as they become more scarce, their scarcity will only lead to rising prices, and the demand will continue to remain high, which sooner or later will become a major issue. However, renewable energy is sustainable and eco-friendly. As much as, renewable energy has attracted significant attention in recent years, there is still little energy consumption by renewable compared to nonrenewable sources, as illustrated in figure 1.1.

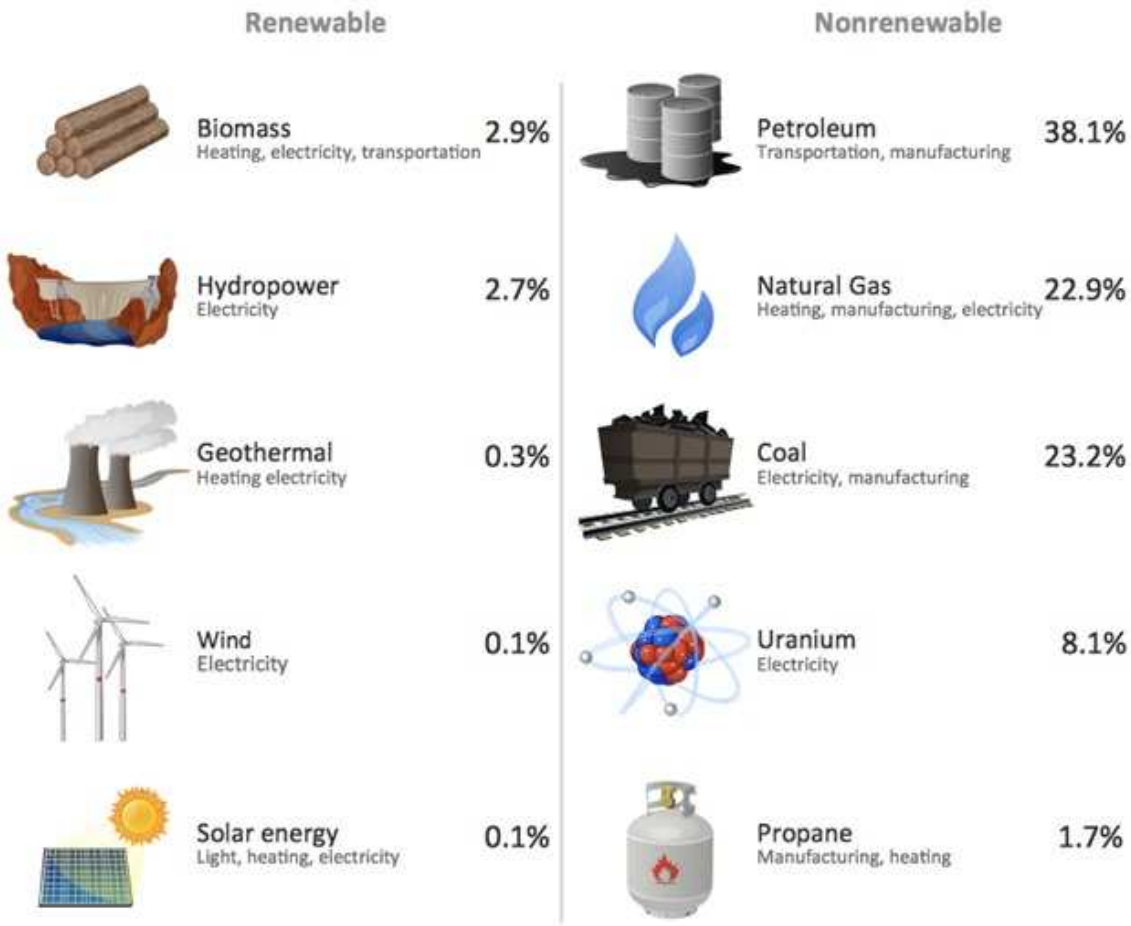

Figure 1.1: The percentage distribution of US energy consumption by renewable and nonrenewable sources [1].

Due to an urgent need for efficient, clean, and sustainable sources of energy, as well as new technologies associated with energy conversion and storage, the most effective and practical technologies for electrochemical energy conversion and storage are batteries, fuel cells, and electrochemical supercapacitors. In recent years, there have been a large number of research articles and technical reports on the development of electrochemical supercapacitors [2-6], mainly motivated by their low energy density. In the approaches to overcome the low energy density of supercapacitors (SCs), one of the most intensive approaches is the development of new materials for SCs electrodes. Hence in energy research, the foundation and the development of the sustainable power conversion and energy storage systems focus on the innovative electrode materials for batteries and supercapacitors and these materials are investigated at the micro- and nano-scale [7,8]. Electrode materials for electrochemical energy storage systems in micro- or rather nano-scale show an increase in the surface area-to-volume ratio which leads to an increase in the amount of interfaces and increased rate of transport phenomena (i.e. enhanced electron and mass transport) yielding electrodes with much higher current densities which is important for electrochemical energy conversion [7,8]. The electrochemical energy conversion process is basically a surface and interface process in which electron exchanges between the surface of an electrode and solution (electrolyte) affecting the electrochemical performance and stability of the energy storage systems.

Furthermore, asymmetric supercapacitors or hybrid supercapacitor devices considered as future energy storage systems combine the best features of metal-ion batteries and electrochemical supercapacitors to achieve enhanced energy, power density, and cyclability at a lower cost (Figure 1.2). Consequently, research focus in SCs is on improving the energy density (i.e. ≈5-8 Wh kg^{-1}) without compromising its high power density (i.e. ≈5-30 kW kg^{-1}) (Figure 1.3), unlike in rechargeable batteries which already have a high energy density in the range of 120-200 Wh kg^{-1}, and hence the focus will be on improving the power density which is in the range of 0.4-3 kW kg^{-1} [8-11].

Among various types of energy storage devices, SCs have attracted great attention for potential applications in electronic circuits, electric vehicles, and backup power generators [13]. Since SCs have attractive properties such as portability, high efficiency, fast charge-discharge capability, long lifecycle stability, operational safety, and high power density [14]. The charge storage mechanism in SCs is divided into two classifications, to be precise, the electric double layer capacitors (EDLCs) and pseudocapacitors [7,8,15]. In EDLCs, energy storage is attained by double-layer capacitance, and in this charge storage process, there is no transfer of charges. Carbon-based materials with a high surface area are usually used as for EDLCs. In pseudocapacitors, the electrical energy is stored faradaically by electron charge transfer between electrode and electrolyte [8]. This is accomplished through electrosorption, reduction-oxidation reactions (redox reactions), and intercalation processes,

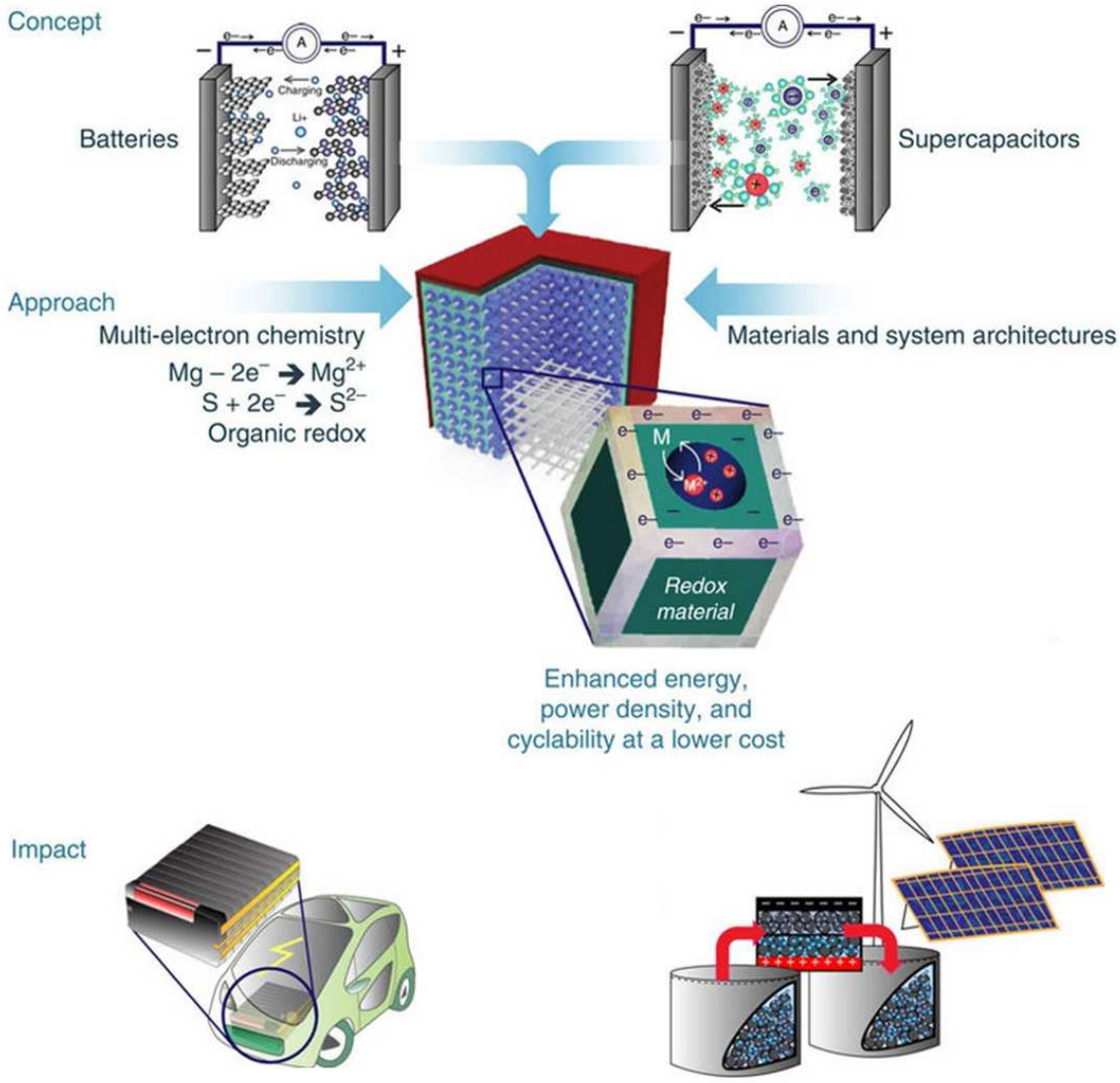

Figure 1.2: Conceptual presentation of the development of fully integrated rechargeable hybrid battery-supercapacitor (supercapbattery) electrical energy storage devices [12].

called pseudocapacitance. The electrically conducting polymers and transition metal oxides/hydroxide/sulfides are normally used in pseudocapacitors [16-19]. In addition, the two charge storage mechanisms of SCs are combined in hybrid capacitors to yield high energy and power density.

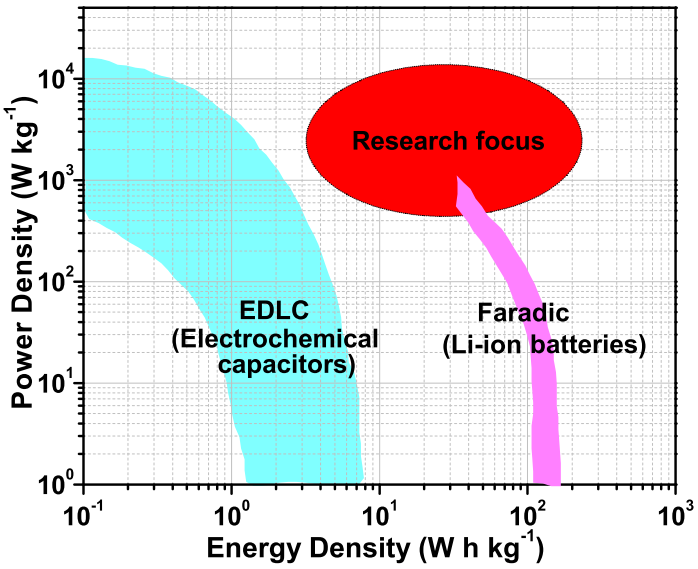

Figure 1.3: Ragone plot showing the relationship between energy and power density regions for electrochemical capacitors (EDLC behavior) and lithium-ion batteries (Faradic behavior), including the research focus region for electrochemical capacitors and lithium-ion batteries.

Furthermore, among various conducting polymers that have been studied, PANI has attracted great attention as one of the most promising pseudocapacitive material suitable for the next generation of supercapacitors due to its high pseudocapacitance, light weight, low cost, controllable electrical conductivity, high energy density, facile synthesis, and environmental friendliness [20-23]. However, PANI experience volume changes, i.e. the pseudocapacitive processes of PANI involve the swelling, shrinkage and cracking of the material during charging/discharging, which could result in cycling instability and poor rate performance [13,24,25]. It is shown in previously published reports that the electrochemical performance of PANI can be improved by use of PANI-carbon composites with carbon materials such

as carbon nanotubes, nanofibers, graphene sheets and powdered activated carbon due to their high stability, good conductivity and high affordability [24-31].

Moreover, the need to develop high-performance supercapacitors has led to the incorporation of metals and metal oxide particles into PANI to enhance its electrical conductivity [32]. It has been shown that iron-containing nitrogen-doped graphitic carbon materials, carbonized PANI in particular, achieve high electrocatalytic performance and exhibit high stability [33,34]. These iron-containing nitrogen-doped PANI materials are synthesized by pyrolysis of carbon materials and PANI, in which the nitrogen-atoms originating from PANI coordinate Fe sites (Fe-PANI/carbon) [33,34]. Other than containing nitrogen, the preference of PANI is as result of its phenyl groups which easily produce a graphitic structure during pyrolysis, thus leading to enhanced electrical conductivity [34]. Although carbonized Fe-PANI/carbon studies have been reported in the literature for fuel cell applications [33,34], there are few studies done on the carbonized Fe adsorbed onto PANI (C-Fe/PANI) as a binder-free electrode material directly synthesized on current collector for supercapacitor applications.

Until now, transition metal oxides/sulfides and layered transition-metal dichalcogenides (TMDs) such as MoS_2, VS_2, WS_2, FeS_2, CoS_2, and NiS_2, have been successfully established as a new paradigm in the chemistry of nanomaterials especially for nanotubes and fullerene-like nanostructures as

well as the graphene analogs, have been extensively investigated as the positive electrode materials for SCs due to their high faradic capacitance [35-39]. On the other hand, VS_2 has not received much attention in two electrode supercapacitor devices. However, it has been investigated for applications in SCs due to its promising electrochemical performance. Recently, Feng *et al.* [40], reported all-in-solution route to synthesize VS_2 phase for the first time, taking advantage of an intermediate intercalated compound precursor of $VS_2{\cdot}NH_3$. This report clearly demonstrated that VS_2 nanosheets are highly conductive and have a high specific capacitance, showing promising signs for 2D material to be utilized in energy storage devices. Masikhwa *et al.* [41], reported the design of an asymmetric supercapacitor based on 3D interconnected activated carbon as the negative electrode and mesoporous VS_2 nanosheets as the positive electrode material. The report suggests that pairing hybrid materials could be an excellent method to produce SCs with high energy and power densities.

1.2 Aims and objectives

The aim and objectives of the study are divided into two parts:

Part 1: The study is aimed at investigating the structural, composition and morphological characteristics of the as-synthesized electrode material, and the electrochemical properties of C-Fe/PANI symmetric device.

Part 2: Although studies about VS_2 electrode for supercapacitor applications have been reported in the literature, there are few studies done on the binder-free electrode material based on carbonized Fe cations adsorbed onto PANI (C-Fe/PANI) and until now there are no reports on VS_2//C-Fe/PANI asymmetric cell device. Herein, we report on asymmetric supercapacitor based on VS_2 nanosheets as a cathode and C-Fe/PANI as an anode. This study is focused on structural and morphological characterization of the as-synthesized electrode materials and the electrochemical properties of VS_2//C-Fe/PANI asymmetric device.

1.2.1 Specific research objectives:

(i) Synthesis of C-Fe/PANI by pyrolysis of the iron-PANI mixture coated on nickel foam in a tube furnace under the N_2 atmosphere.

(ii) Synthesis of VS_2 nanosheets using a hydrothermal method.

(iii) Structural, and morphological characterization of the as-synthesized electrode materials using X-ray diffraction (XRD), Raman spectrometer, Fourier transform infrared (FTIR) spectrometer, scanning electron microscopy (SEM), energy-dispersive X-ray spectrometer (EDS), transmission electron microscopy (TEM) and X-ray photoelectron spectroscopy (XPS).

(iv) Electrochemical characterization of the active electrodes using Biologic

VMP-300 potentiostat (Knoxville TN 37,930, USA) controlled by the EC-Lab V10.37 software at room temperature.

1.3 Outline of the thesis:

PART I: INTRODUCTION

Chapter 1: This chapter presents the general introduction of energy storage systems, the aim and the objectives of the study.

PART II: LITERATURE OVERVIEW

Chapter 2: This chapter presents literature overview on supercapacitors.

PART III: EXPERIMENT AND PROCEDURE

Chapter 3: This chapter presents the synthesized materials characterized using various techniques, namely, XRD, Raman spectroscopy, FTIR spectroscopy, SEM, EDS, TEM and XPS and this chapter presents an introductory overview of these techniques.

Chapter 4: This chapter presents the experimental procedures and techniques used for the synthesis and characterizations of as-synthesized materials. The first part of this chapter focuses on the synthesis of C-Fe/PANI and VS_2 nanosheets, including the characterization techniques used for structural, morphological and electrochemical analysis of the as-synthesized materials. The last part of this chapter focuses on the fabrication of electrodes

for three-electrode and two-electrode setup.

PART IV: RESULTS, DISCUSSIONS AND CONCLUSIONS

Chapter 5: This chapter presents experimental findings on the structural and morphological characterization of the as-synthesized C-Fe/PANI electrode in comparison to annealed and unannealed PANI electrode and includes the electrochemical properties of the fabricated C-Fe/PANI symmetric device.

Chapter 6: This chapter presents the experimental findings on the structural and morphological characterization of the as-synthesized electrode materials (i.e. VS_2 nanosheets and C-Fe/PANI) and the electrochemical properties of the electrodes and fabricated VS_2//C-Fe/PANI asymmetric device.

Chapter 7: This chapter draws a general conclusion outlining the results obtained in this study, including a brief discussion on the possible future work.

Bibliography

1. U.S. Energy Consumption By Source/Visual.ly, https://visual.ly/community/infographic/business/us-energy-consumption-source (accessed October 1, 2017).

2. E. Frackowiak, Carbon materials for supercapacitor application., Phys. Chem. Chem. Phys. 9 (2007) 1774-85. doi:10.1039/b618139m.

3. L.L. Zhang, X.S. Zhao, Carbon-based materials as supercapacitor electrodes., Chem. Soc. Rev. 38 (2009) 2520-31. doi:10.1039/b813846j.

4. H. Pan, J. Li, Y.P. Feng, Carbon Nanotubes for Supercapacitor, Nanoscale Res. Lett. 5 (2010) 654-668. doi:10.1007/s11671-009-9508-2.

5. E. Frackowiak, F. Béguin, Carbon materials for the electrochemical storage of energy in capacitors, Carbon. 39 (2001) 937-950. doi:10.1016/S0008-6223(00)00183-4.

6. S.W. Zhang, G.Z. Chen, Manganese oxide based materials for supercapacitors, Energy Mater. 3 (2008) 186-200. doi:10.1179/174892409X427940.

7. G. Feng, S. Li, V. Presser, P.T. Cummings, Molecular Insights into Carbon Supercapacitors Based on Room-Temperature Ionic Liquids, J. Phys. Chem. Lett. 4 (2013) 3367-3376. doi:10.1021/jz4014163.

8. P. Simon, Y. Gogotsi, Materials for electrochemical capacitors, Nat. Mater. 7 (2008) 845-854. doi:10.1038/nmat2297.

9. X. Rui, H. Tan, Q. Yan, Nanostructured metal sulfides for energy storage, Nanoscale. 6 (2014) 9889. doi:10.1039/C4NR03057E.

10. B.E. Conway, Electrochemical Supercapacitors Scientific Fundamentals and Technological Applications, Kluwer Academic Publishers, Plenum Press: New York, 1999.

11. J.R.J. Miller, A.F.A. Burke, Electrochemical capacitors: challenges and opportunities for real-world applications, Electrochem. Soc. Interface. 17 (2008) 53.

12. M.R. Lukatskaya, B. Dunn, Y. Gogotsi, Multidimensional materials and device architectures for future hybrid energy storage, Nat. Commun. 7 (2016) 12647. doi:10.1038/ncomms12647.

13. S.K. Simotwo, C. Delre, V. Kalra, Supercapacitor Electrodes Based on High-Purity Electrospun Polyaniline and Polyaniline-Carbon Nanotube Nanofibers, ACS Appl. Mater. Interfaces. 8 (2016) 21261-21269. doi:10.1021/acsami.6b03463.

14. S. Mondal, U. Rana, S. Malik, Reduced Graphene Oxide/Fe_3O_4/Polyaniline Nanostructures as Electrode Materials for an All-Solid-State Hybrid Supercapacitor, J. Phys. Chem. C. 121 (2017) 7573-7583. doi:10.1021/acs.jpcc.6b10978.

15. G. Zhang, M. Kong, Y. Yao, L. Long, M. Yan, One-pot synthesis of γ-MnS/ reduced graphene oxide with enhanced performance for aqueous asymmetric supercapacitors, Nanotechnology 28 (2017) 065402. doi:10.1088/1361-6528/aa52a5.

16. X. Wang, J. Deng, X. Duan, D. Liu, J. Guo, P. Liu, Crosslinked polyaniline nanorods with improved electrochemical performance as electrode material for supercapacitors, J. Mater. Chem. A. 2 (2014) 12323. doi:10.1039/C4TA02231A.

17. V. Kumar, P.S. Lee, Redox Active Polyaniline-h-MoO_3 Hollow Nanorods for Improved Pseudocapacitive Performance, J. Phys. Chem. C. 119 (2015) 9041-9049. doi:10.1021/acs.jpcc.5b00153.

18. X. Zheng, J. Luo, W. Lv, D.W. Wang, Q.H. Yang, Two-dimensional porous carbon: Synthesis and ion-transport properties, Adv. Mater. 27 (2015) 5388-5395. doi:10.1002/adma.201501452.

19. M.H. Bai, T.Y. Liu, F. Luan, Y. Li, X.X. Liu, Electrodeposition of vanadium oxide-polyaniline composite nanowire electrodes for high energy density supercapacitors, J. Mater. Chem. A. 2 (2014)

10882-10888. doi:10.1039/c3ta15391f.

20. M. Sawangphruk, M. Suksomboon, K. Kongsupornsak, J. Khuntilo, P. Srimuk, Y. Sanguansak, et al., High-performance supercapacitors based on silver nanoparticle-polyaniline-graphene nanocomposites coated on flexible carbon fiber paper, J. Mater. Chem. A. 1 (2013) 9630. doi:10.1039/c3ta12194a.

21. K.S. Ryu, K.M. Kim, N.G. Park, Y.J. Park, S.H. Chang, Symmetric redox supercapacitor with conducting polyaniline electrodes, J. Power Sources. 103 (2002) 305-309. doi:10.1016/S0378-7753(01)00862-X.

22. S. Zhou, H. Zhang, Q. Zhao, X. Wang, J. Li, F. Wang, Graphene-wrapped polyaniline nanofibers as electrode materials for organic supercapacitors, Carbon. 52 (2013) 440-450. doi:10.1016/j.carbon.2012.09.055.

23. M. Sawangphruk, T. Kaewsongpol, Direct electrodeposition and superior pseudocapacitive property of ultrahigh porous silver-incorporated polyaniline films, Mater. Lett. 87 (2012) 142-145. doi:10.1016/j.matlet.2012.07.103.

24. G.A. Snook, P. Kao, A.S. Best, Conducting-polymer-based supercapacitor devices and electrodes, J. Power Sources. 196 (2010) 1-12. doi:10.1016/j.jpowsour.2010.06.084.

25. S. Bose, T. Kuila, A.K. Mishra, R. Rajasekar, N.H. Kim, J.H.

Lee, Carbon-based nanostructured materials and their composites as supercapacitor electrodes, J. Mater. Chem. Mater. Chem. 22 (2012) 767-784. doi:10.1039/c1jm14468e.

26. H. Mi, X. Zhang, S. An, X. Ye, S. Yang, Microwave-assisted synthesis and electrochemical capacitance of polyaniline/multi-wall carbon nanotubes composite, Electrochem. Commun. 9 (2007) 2859-2862. doi:10.1016/j.elecom.2007.10.013.

27. M. Wu, G.A. Snook, V. Gupta, M. Shaffer, D.J. Fray, G.Z. Chen, Electrochemical fabrication and capacitance of composite films of carbon nanotubes and polyaniline, J. Mater. Chem. 15 (2005) 2297. doi:10.1039/b418835g.

28. M.J. Bleda-Martinez, C. Peng, S. Zhang, G.Z. Chen, E. Morallon, D. Cazorla-Amoros, Electrochemical Methods to Enhance the Capacitance in Activated Carbon/Polyaniline Composites, J. Electrochem. Soc. 155 (2008) A672. doi:10.1149/1.2956969.

29. D. Salinas-Torres, J.M. Sieben, D. Lozano-Castellï£¡, D. Cazorla-Amorï£¡s, E. Morallï£¡n, Asymmetric hybrid capacitors based on activated carbon and activated carbon fibre-PANI electrodes, Electrochim. Acta. 89 (2013) 326-333. doi:10.1016/j.electacta.2012.11.039.

30. K.S. Ryu, Y.G. Lee, K.M. Kim, Y.J. Park, Y.S. Hong, X. Wu, et

al., Electrochemical capacitor with chemically polymerized conducting polymer based on activated carbon as hybrid electrodes, Synth. Met. 153 (2005) 89-92. doi:10.1016/j.synthmet.2005.07.167.

31. F. Chen, P. Liu, Q. Zhao, Well-defined graphene/polyaniline flake composites for high performance supercapacitors, Electrochim. Acta. 76 (2012) 62-68. doi:10.1016/j.electacta.2012.04.154.

32. S.S. Umare, B.H. Shambharkar, R.S. Ningthoujam, Synthesis and characterization of polyaniline-Fe3O4 nanocomposite: Electrical conductivity, magnetic, electrochemical studies, Synth. Met. 160 (2010) 1815-1821. doi:10.1016/j.synthmet.2010.06.015.

33. H. Peng, Z. Mo, S. Liao, H. Liang, L. Yang, F. Luo, et al., High Performance Fe- and N- Doped Carbon Catalyst with Graphene Structure for Oxygen Reduction, Sci. Rep. 3 (2013) 1765. doi:10.1038/srep01765.

34. N. Daems, X. Sheng, Y. Alvarez-Gallego, I.F.J. Vankelecom, P.P. Pescarmona, Iron-containing N-doped carbon electrocatalysts for the cogeneration of hydroxylamine and electricity in a H_2-NO fuel cell, Green Chem. 18 (2016) 1547-1559. doi:10.1039/C5GC02197A.

35. Y. Tang, T. Chen, S. Yu, Y. Qiao, S. Mu, J. Hu, et al., Synthesis of graphene oxide anchored porous manganese sulfide nanocrystals via the nanoscale Kirkendall effect for supercapacitors, J. Mater. Chem. A. 3

(2015) 12913-12919. doi:10.1039/C5TA02480C.

36. P.C. Chen, G. Shen, Y. Shi, H. Chen, C. Zhou, Preparation and Characterization of Flexible Asymmetric Supercapacitors Based on Transition-Metal-Oxide Nanowire/Single-Walled Carbon Nanotube Hybrid Thin-Film Electrodes, ACS Nano. 4 (2010) 4403-4411. doi:10.1021/nn100856y.

37. Y. Tang, T. Chen, S. Yu, Y. Qiao, S. Mu, S. Zhang, et al., A highly electronic conductive cobalt nickel sulphide dendrite/quasi-spherical nanocomposite for a supercapacitor electrode with ultrahigh areal specific capacitance, J. Power Sources. 295 (2015) 314-322. doi:10.1016/j.jpowsour.2015.07.035.

38. Y. Tang, T. Chen, S. Yu, Morphology controlled synthesis of monodispersed manganese sulfide nanocrystals and their primary application in supercapacitors with high performances, Chem. Commun. 51 (2015) 9018-9021. doi:10.1039/C5CC01700A.

39. L. Dong, C. Xu, Y. Li, Z.H. Huang, F. Kang, Q.H. Yang, et al., All-solid-state high performance asymmetric supercapacitors based on novel MnS nanocrystal and activated carbon materials, Sci. Rep. 6 (2016) 23289. doi:10.1038/srep23289.

40. J. Feng, X. Sun, C. Wu, L. Peng, C. Lin, S. Hu, et al., Metallic few-layered VS_2 ultrathin nanosheets: High two-dimensional

conductivity for in-plane supercapacitors, J. Am. Chem. Soc. (2011). doi:10.1021/ja207176c.

41. T.M. Masikhwa, F. Barzegar, J.K. Dangbegnon, A. Bello, M.J. Madito, D. Momodu, et al., Asymmetric supercapacitor based on VS_2 nanosheets and activated carbon materials, RSC Adv. (2016). doi:10.1039/C5RA27155J.

PART II

LITERATURE OVERVIEW

Chapter 2

Literature overview on supercapacitors

2.1 Introduction

This study focuses on the application of supercapacitors for electrochemical energy storage. This chapter presents an overview of the different types of suppercapacitors as well as the parameters that are involved in their evaluation such as energy and power densities (Ragone plot), electrode materials and electrolytes. A brief discussion on testing and fabrication of an electrochemical cell and evaluation of electrode materials for electrochemical capacitors is also presented.

2.2 Supercapacitors

Supercapacitors (SCs) which are also referred to as electrochemical capacitors (ECs) have attracted great interest because of their important application

in the area of electrochemical energy storage such as digital communication, electric vehicles and other electric devices at high pulse power level [1-3]. SCs are high power-delivery storage devices which are able to charge-discharge in a shorter time by exploiting their fast surface or near surface reactions and delivering high power compared to conventional batteries [4-7]. Though, SCs are high power-delivery storage devices (have high power density) they have low energy density especially compared to rechargeable batteries (e.g. Li-ion batteries) [4,8]. Accordingly, research focus in SCs is on improving the energy density which at the moment is within ≈5-8 Wh kg^{-1} without compromising its high power density (i.e. ≈5-30 kW kg^{-1}), unlike in rechargeable batteries which already have a high energy density (120-200 Wh kg^{-1}), but low power density (0.4-3 kW kg^{-1}) [4-6,9]. Recently, asymmetric (hybrid) systems have been explored to increase the operating voltage to improve the energy density of the SCs. Figure 2.1 is the Ragone plot showing variation of energy density versus power density for different energy storage systems.

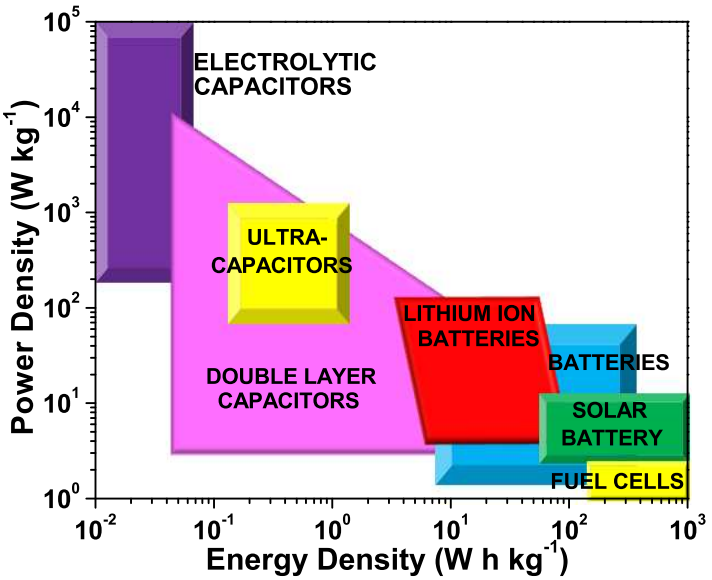

Figure 2.1: Ragone plot of various energy density and power density for different energy storage systems (Adopted from Ref. [4]).

2.3 Principle of energy storage in SCs

Generally, the behavior of the SCs is mainly influenced by the charge storage mechanism which is divided into three classifications [10-12]:

(i) Electric double layer capacitors (EDLCs)

(ii) Pseudocapacitors or electrochemical capacitors (RECs)

(iii) Hybrid capacitors

The flow chart in figure 2.2 is showing an overview of each of these classes of supercapacitors depending on charge storage mechanism.

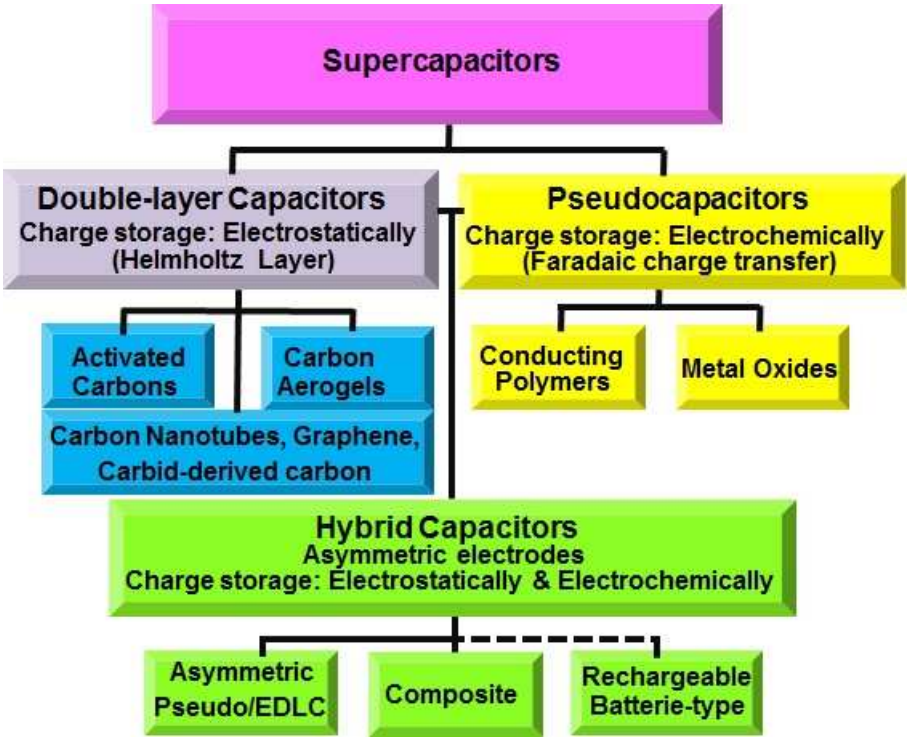

Figure 2.2: The classification of electrochemical capacitors depending on the charge storage mechanism (Adopted from Ref. [12]).

2.3.1 Electric double layer capacitors (EDLCs)

The energy storage of the EDLCs is generally achieved through a double-layer capacitance and in this charge storage process; there is no transfer of charges across the electrode/electrolyte interface. This implies that during the charging process, the electrons travel from the negative electrode to the positive electrode through an external circuit and during the discharging process, the reverse processes take place. As demonstrated in figure 2.3, SCs consist of a positive and negative electrode, an electrolyte, and a separator. Generally, in EDLC cell the applied potential on the negative electrode attracts the positive ions in the electrolyte, similarly, when the same potential is

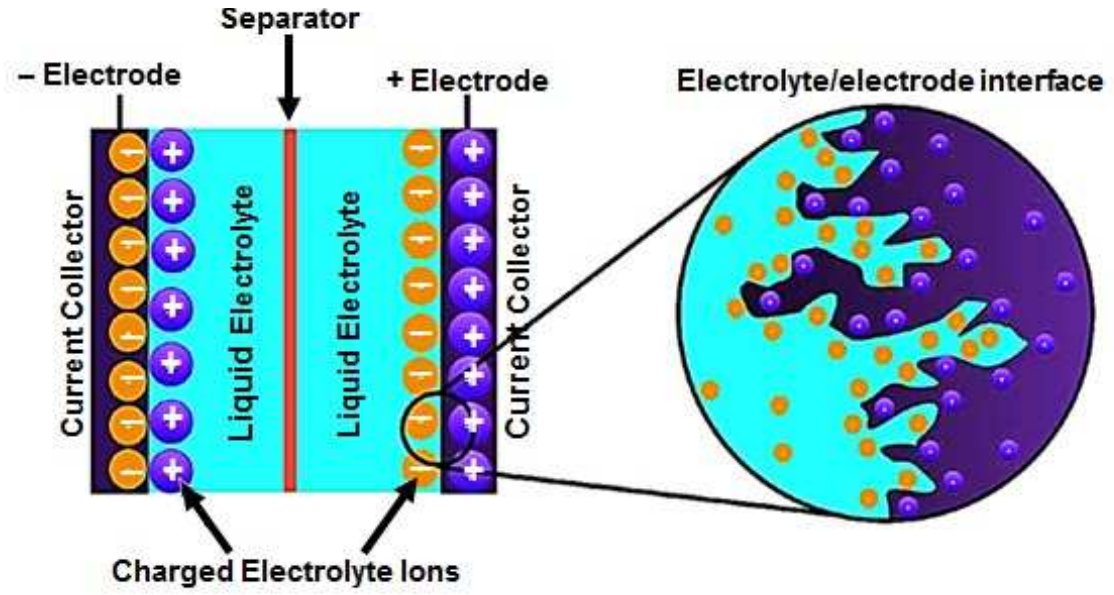

Figure 2.3: Schematic illustration of energy storage mechanism in EDLCs (Adopted from Ref. [13]).

applied to the positive electrode, it attracts the negative ions. Typically, the electrodes used for EDLCs are carbon materials and are separated by a dielectric separator which prevent short-circuit of the device [13]. Charge separation occurs upon polarization at the electrode/electrolyte interface producing the EDLC. As a result, the EDLCs store charge based on pure electrostatic charge accumulation at the electrode/electrolyte interface, as illustrated in figure 2.3 [13]. Hence, this interface can be seen as a capacitor with an electrical double-layer capacitance, which can be expressed as [13]:

$$C = \frac{A\varepsilon}{4\pi d} \tag{2.1}$$

where A is the surface area of the electrode, ε is the is the local dielectric constant of the electrolyte ($\varepsilon = 1$ for a vacuum and $\varepsilon > 1$ for all other materials),

and d is the effective thickness of the electrical double layer.

From equation 2.1 it can be seen that the electrodes with high surface area and high porosity could have a large capacitance hence EDLCs store a very large amount of energy as compared to normally electrolytic capacitors, this is due to their porous surface structure of the electrode, electrolyte composition and the potential field between the charges at the interface [13].

It is worth noting that in EDLCs there is no chemical reaction involved in the energy storage mechanism. The EDLCs are electrochemically stable due to the energy storage mechanism which is physical and are highly reversible. Subsequently, the amount of charge and discharging mechanism in the EDLCs are only reliant on the movement of ions hence the EDLCs can store and release energy faster than batteries that relies on slower chemical reactions.

2.3.2 Pseudocapacitors

Pseudocapacitors differ from the EDLCs by means of charge storage mechanism. In pseudocapacitors, the electrical energy is stored faradaically by electron charge transfer between electrode and electrolyte. This is accomplished through electro-sorption processes, reduction-oxidation reactions (redox reactions) and intercalation process, as demonstrated in figure 2.4 [4]. The electrochemical adsorption of ions onto the surface or near the surface of an electrode material accompanied with a related faradaic charge transfer is described as redox pseudocapacitance while intercalation

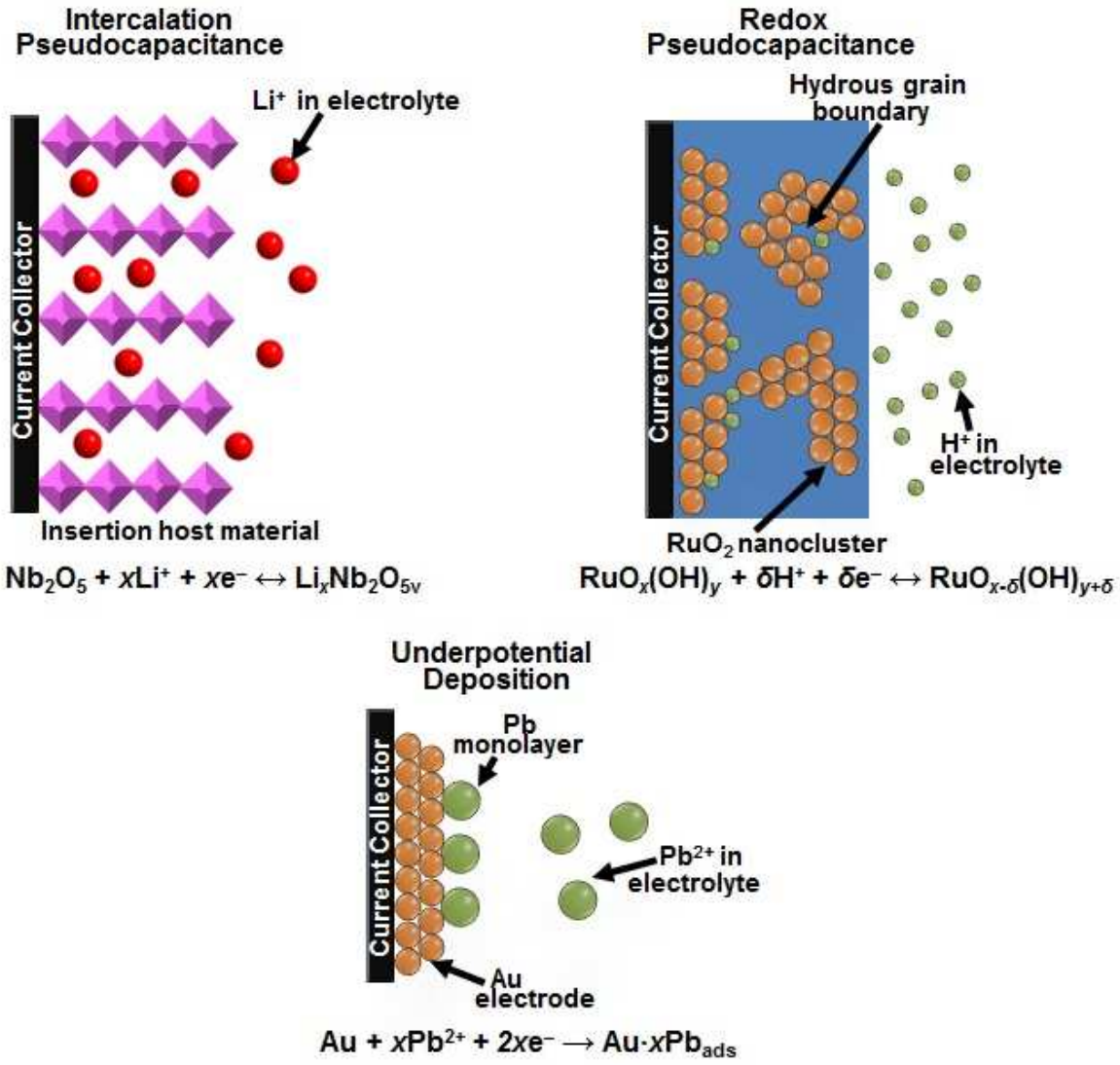

Figure 2.4: Schematic illustration of different redox mechanisms that give rise to pseudocapacitors (Adopted from Ref. [4]).

pseudocapacitance arises from the intercalation of ions into the layers or pores of pseudocapacitive materials accompanied with a faradaic charge transfer with no crystallographic phase change [4]. The formation of adsorbed surface monolayer from ions contained within the electrolyte on the electrode composed of a different metal which has a redox potential and is termed underpotential deposition [4].

Generally, Pseudocapacitors fill the gap between batteries and double layer capacitors and are capable of charging and discharging from tens of seconds to several minutes. Their main advantage is that they can store as much charge as some batteries while operating much faster.

2.3.3 Hybrid capacitors

Apart from capacitance, the other two important parameters of the capacitor are its energy and power densities. Since EDLCs have high power density, but lower energy density compared to faradaic materials which have high energy density but lower power density to achieve a high electrochemical performance (e.g. high energy and power densities) hybrid capacitors integrate both EDLC and faradaic energy storage mechanisms. Generally, hybrid capacitors refer to the combination of both EDLC and faradaic materials. In hybrid capacitors, both EDLC and faradaic capacitance mechanisms occur simultaneously, however, one of them is dominating to achieve high capacitance and/or high operating potential window. In these mechanisms, the essential properties of the electrode materials are a large surface area, appropriate pore-size distribution, and high conductivity. The most common fabrication of hybrid capacitor consists of a battery-type electrode (e.g., faradaic or intercalating metal oxide) and the EDLC-type electrode. Hybrid capacitors can also be fabricated using two different mixed metal oxide or doped conducting polymer materials. For instance, a composite hybrid capacitor consists of an electrode

fabricated from a carbon material incorporated into a conducting polymer or metal oxide material. Moreover, it can also be fabricated using the EDLC-type material as an anode electrode and faradiac-type material as cathode electrode (i.e. asymmetric capacitor). Therefore, hybrid capacitors can be categorized into three classes, namely battery-type, composite and asymmetric hybrids [10-12]. Typically, the charger-discharge characteristics of hybrid capacitors are nonlinear.

Hybrid devices are considered as future energy storage systems since they combine the best properties (energy storage mechanisms) of faradaic and EDLC electrode materials to achieve enhanced energy, power density, and cyclability.

2.4 Electrode material for supercapacitor

As had been shown in figure 2.3, SCs consist of three essential components, viz., electrode, electrolyte and the separator. However, electrode material is the most important component of a supercapacitor. It plays an important role in determining the energy and power densities of supercapacitors. Its electrochemical performances strongly depend on factors like electrical conductivity, surface area, wetting of electrode and permeability of electrolyte solutions.

The electrode materials of SCs can be categorized into three types:

(i) Carbon materials (e.g. activated carbon, carbon aerogels, carbon nanotubes, graphene etc.) [14,15].

(ii) Conducting polymers (e.g. polyaniline, polypyrrole and polythiophene) [16-19].

(iii) Metal oxides/hydroxides (e.g. RuO_2, IrO_2, MnO_2, NiO and MoO etc.) [20-26] and two-dimensional (2D) layered transition-metal dichalcogenides (e.g. MoS_2, CoS_2, VS_2 and NiS_2) [27-30].

Carbon materials are widely used for supercapacitor applications due to their low cost and versatile existing forms (e.g. powders, fibers, felts, composites, mats, monoliths, and foils), good electronic conductivity, high chemical stability, and wide operating temperature range [31,32]. As mentioned earlier, the storage mechanism used by carbon materials is electrochemical double layer formed at the interface between the electrode and electrolyte. Having high specific surface area in the case of carbon materials, results in a high capability for charge accumulation at the interface of electrode and electrolyte. When improving specific capacitance for carbon materials, apart from pore size and high specific surface area, surface functionalization must be considered. The presence of functional groups on the surface of carbonaceous materials may induce faradaic redox reactions on the surface of the material leading to an increase in the total capacitance of the electrode [33]. Another way to increase the capacitance and also enhance stability is to synthesis

carbon-supported transition metal oxides composites.

Conducting polymers have been considered for electrochemical energy storage applications due to their low cost, high conductivity in a doped state, high voltage window and high storage capacity/porosity/reversibility [32,34-36]. Due to the high content of functional groups in conducting polymers, they offer capacitance through the redox process. During the redox reactions which involve the entire polymer, ions are transferred to the polymer backbone during oxidation, and from the polymer backbone into the electrolyte during reduction hence the processes are highly reversible [37]. The common conducting polymers in supercapacitor applications are polyaniline, polypyrrol, polythiophene [38-41]. However, due to swelling and shrinking of conducting polymers which may occur during the charging/discharging process the electrode may experience a fading electrochemical performance during cycling. This compromises conducting polymers as electrode materials for supercapacitor applications. To improve the challenge of low stability, few approaches have been investigated. For instance, improving conducting polymer materials' structures and morphologies [42] and fabricating composite electrode materials [43-50]. The electrochemical performance of conducting polymers can be greatly enhanced by preparing a conducting polymer-based composite using carbon, inorganic oxides/hydroxides, and metal compounds.

Metal oxides/hydroxides/sulfides (layered transition-metal dichalcogenides) as

electrode materials in SCs have received attention due to their potential to attain high capacitance, and also due to their excellent physico-chemical properties and cycling stability. In supercapacitor applications, the main requirements for metal oxides/hydroxides/sulfides as electrode materials are: (1) they should be electronically conductive, (2) the metal can exist in two or more oxidation states with no phase changes, and (3) the protons can freely intercalate into and out of the oxide/sulfide lattice on reduction and oxidation respectively [32,51]. In general, metal oxides/hydroxides/sulfides in SCs provide high capacitance than carbon materials and better electrochemical stability than conducting polymer materials. Because of the electrochemical faradaic reactions between electrode materials and ions within appropriate potential windows [52-58].

2.5 Electrolytes for supercapacitor

The electrolyte which is placed between a supercapacitor's anode and cathode plays a very important role in supercapacitors (Figure 2.3). Basically, it contains ions necessary for charge transport and charge storage. It is worth mentioning that in two-electrode setup the electrolyte is between two electrodes and its ions are transported through a separator between two electrodes, however, in three-electrode setup, the electrodes (i.e. working, reference and counter electrode) are immersed in the electrolyte. For the electrolyte to be suitable in supercapacitors it has to meet the requirements

such as having wide voltage window, high electrochemical stability, high ionic conductivity and small solvated ionic radius, low resistivity, low viscosity, low volatility, low toxicity, low cost as well as availability at high purity [32]. The electrolyte used in supercapacitors can be classified into three types: aqueous, organic, and ionic liquids (ILs) electrolytes.

In this study, aqueous electrolytes (such as H_2SO_4, KOH, Na_2SO_4 and NH_4Cl aqueous solution and so on) are preferred compared to organic electrolytes, since they can provide a higher ionic conductivity. In addition, Aqueous electrolytes can be prepared and utilized without stringently controlling the preparing processes and conditions, while organic ones need strict processes and conditions to obtain ultra-pure electrolytes.

Supercapacitors containing aqueous electrolyte may display higher capacitance and higher power than those with organic electrolytes, probably due to higher ionic conductivity and smaller ionic radius [32]. However, the aqueous electrolytes have a limited operating voltage of 1.23 eV (theoretical value) due to the decomposition of water at high applied voltages which might limit the potential window of the supercapacitor. Nonetheless, SCs using aqueous electrolytes have shown the capability to reach higher operating voltages, $\approx$2.0 eV, due to the synergy between the electrodes and the electrolyte [59-61].

2.6 Testing an electrochemical cell

For research purposes, the electrochemical performance of the single electrode is first evaluated in three electrode configuration to obtain the electrochemical properties of each electrode, then in two-electrode setup. Typically in three-electrode setup, the device is referred to as a half-cell and in the two-electrode setup as a full-cell. Figure 2.5 illustrates the schematic diagram of three electrode setup. The three electrode setup consists of a working electrode (WE), a counter electrode (CE) and a reference electrode (RE). The type of counter and reference electrode depend on the electrolyte used. The WE is usually made of active materials pasted on the current collector which serve as a platform where the electrochemical reaction occurs. The RE electrode which has a stable and known electrode potential is usually used as a benchmark in the determination of the potential of a WE without allowing current through it while the counter electrode is used to complete the circuit and it allows the required amount of current through the circuit to balance the current generated at the WE. In the three-electrode system depending on the electrolyte used, e.g. in an acidic electrolyte, a CE can be a glassy carbon plate or platinum and silver/silver chloride electrode (Ag/AgCl) or saturated calomel electrode (SCE) serves as the reference electrode. In neutral electrolyte, the same configuration is used and nickel foil or foam can be used as a current collector.

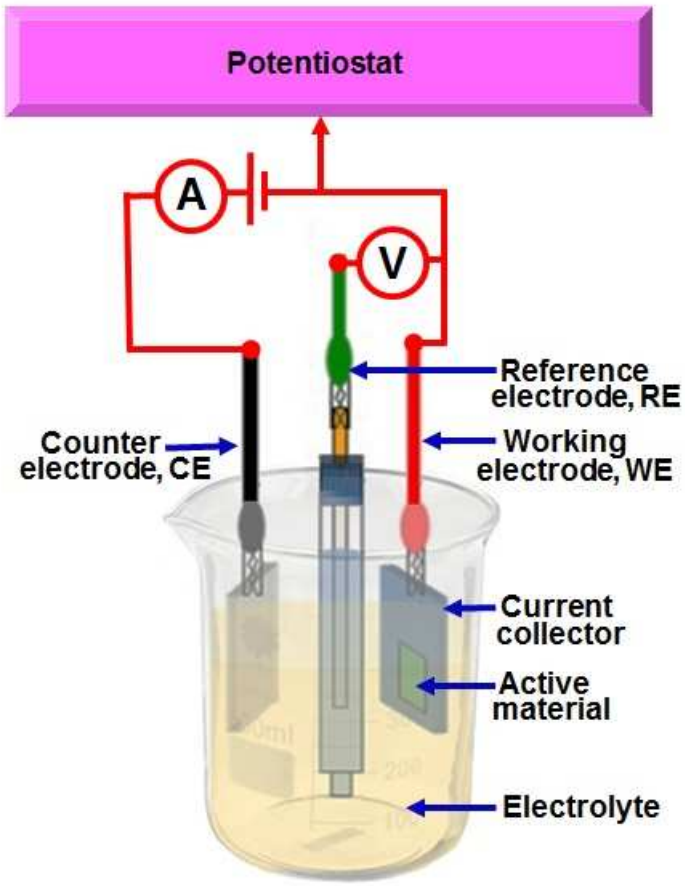

Figure 2.5: Schematic diagram of three electrode cell setup.

The two electrode cell setup is illustrated in figure 2.6. As it can be seen from the figure, the current and sense (S) leads are connected together: The CE and RE are connected on one of the electrodes while the WE and S are also connected on the opposite electrode. In this setup, the potential across the complete cell is measured, including contributions from the electrolyte/CE interface and electrolyte itself. The S leads measure the voltage dropped by the current across the working electrode, electrolyte, and counter electrode, i.e. a whole cell. Typically this setup is used with energy storage or conversion devices.

Furthermore, the two electrode cell can either be symmetric or asymmetric. As shown in figure 2.6, the asymmetric device it generally refers to any combination of positive and negative electrodes, when the two electrodes differ in mass, thickness, type of material and so on. On the other hand, the symmetric device they refer to the combination of positive and negative, when the two electrodes are made from the same material, having the same mass, thickness and other similar electrochemical properties. However, it is important to note that symmetric devices are not the best when comes to designing the supercapacitors. This is due to the fact that electrodes that are made of different materials can be used to expand the operating potential window. In a hybrid/asymmetric device, different charge storage mechanisms are applied in the positive and negative electrode materials [62] which is the focus on the special case of asymmetric devices. Thus, this idea of asymmetric device is exciting, since it allows us to produce combination of positive and negative electrode materials and to perform smart' balancing of their weight/volume, so that overall device performance can be improved significantly in terms of voltage window, capacitance and longevity in comparison with their symmetric counterparts [62,63].

The electrochemical performance of the cell is determined by an electrode, which is the main engine of the cell. To mention a few, this is determined in terms of life expectancy, self-discharge, capacity and resistance. The electrode fabrication including an active material coating process is the most important

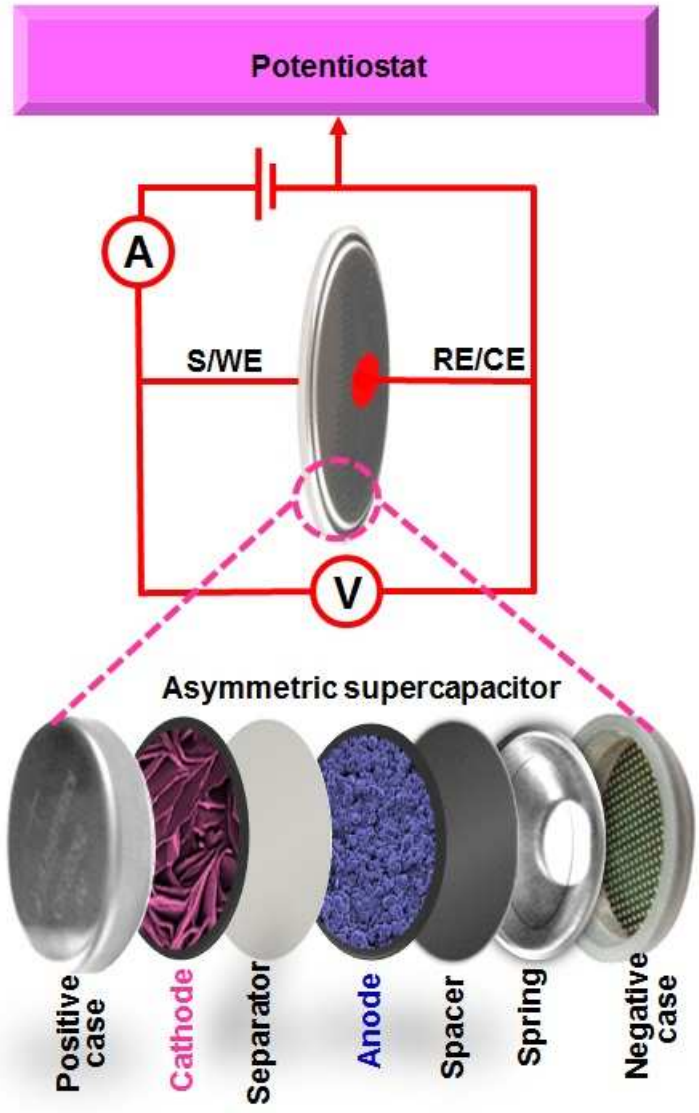

Figure 2.6: The schematic view of the two electrode cell setup including the design of the assembled structure of supercapacitor devices.

step. As a result, a strict control of the preparation process is necessary for achieving both high performance and durability. Recently, nickel foam has been used as a current collector to study the electrochemical performance of electrodes for supercapacitor applications [64-68]. The nickel foam is actually preferred as the current collector because of its high electrical conductivity,

chemical stability in the electrolyte and the mechanical strength since these are the requirements of a current collector in supercapacitor applications.

In the process of coating electrodes (fabricating electrodes), firstly, binders, active materials and conductive additives are mixed to obtain a homogeneous slurry with the desired density, and then the slurry is coated onto annealed nickel foam, followed by drying the electrode and roll pressing to achieve a uniform electrode coating layer. A pair of such electrodes, with a separator layer inserted between them, is wound around a central mandrel into the desired shape. Then the electrolyte is filled into this separator. The electrolyte-filling process generally requires special care. The amount of electrolyte in the cell is critical, because excess electrolyte can lead to excessive gassing and leakage in operation. After the completion of electrolyte filling and sealing of the cell, the cell is subjected to cycling test.

2.7 Evaluation of electrode material for electrochemical capacitors

The electrochemical performance of the electrodes is evaluated using cyclic voltammetry (CV), galvanostatic chronopotentiometry (GCP) and electrochemical impedance spectroscopy (EIS).

2.7.1 Cyclic voltammetry (CV)

CV is a potentiodynamic electroanalytical technique that provides qualitative information on the thermodynamics of redox processes, kinetics of heterogeneous electron transfer reactions and adsorption processes that occur at the electrode/electrolyte interphase in an electrochemical cell. The CV measurements are performed by cycling the potential of a WE and measuring the resulting current. Therefore, a CV curve is a plot of a current response versus the applied potential, as shown in figure 2.7, which describe the nature of the processes that can occur at the electrode/electrolyte interphase. For instance, in figure 2.7, the CV plot reveals the behavior of the electrode as either electrochemical double layer capacitive (i.e. rectangular CV curve) or pseudocapacitive (i.e. CV curve with redox peaks due to faradic reactions) [69]. In electrochemical double layer capacitive behavior, the reverse scan of an ideal EDLC electrode is a mirror image of the forward scan, suggesting that the measured current in CV is independent of the applied potential [70]. However, in the pseudocapacitive electrode, the charge accumulation on the electrode (the measured current) is dependent on the applied potential [71]. In CV, there are three electron transfer processes that occur at the surface of the electrode depending on the nature of the material evaluated, namely, reversible, quasi-reversible or irreversible.

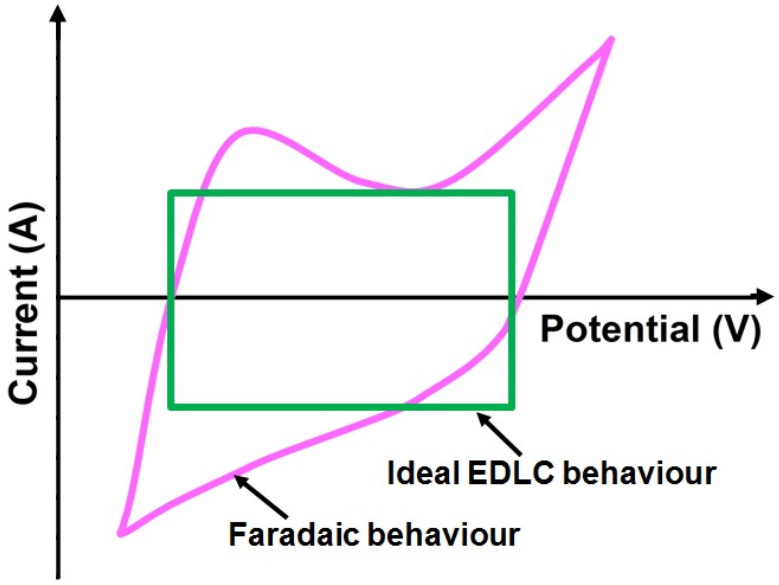

Figure 2.7: Typical CV curves of an ideal EDLC electrode and pseudocapacitive electrode.

Furthermore, using CV curves the specific capacitance (C_S) of the electrodes can be calculated using the following equation [4,72,73]:

$$C_S(Fg^{-1}) = \frac{\int I(V)dV}{m\nu\Delta V} \tag{2.2}$$

where m is the total mass of the active material (g), ν is the scan rate (V s^{-1}), $\Delta V = V_f - V_i$, and V_f and V_i are the integration potential limits of the CV curve (V), and $I(V)$ is the current (A).

Since in two electrode asymmetric device there is difference in the specific capacitance of the two electrodes, a charge balance, $Q_+ = Q_-$ can be done, where Q_+ and Q_- are charge stored in both positive and negative electrodes

respectively, expressed as

$$Q = C_S m \Delta V \tag{2.3}$$

The charge balance is necessary in order to acquire the optimal performance of the device. Based on charge balancing, the mass balance between the positive and negative electrode can be expressed using the following equation [40]:

$$\frac{m_+}{m_-} = \frac{C_{S(-)} \Delta V_-}{C_{S(+)} \Delta V_+} \tag{2.4}$$

where $C_{S(+)}$ and $C_{S(-)}$ are the specific capacitance of the electrodes in positive and negative potential window respectively, m_+ and m_- are the masses of the electrodes in positive and negative potential window, and ΔV_+ and ΔV_- are the positive and negative potential windows of the working electrodes respectively.

2.7.2 Galvanostatic charge-discharge (GCD)

The GCD is one of the most important characterization tool for the determination of the electrochemical performance of the supercapacitors electrodes. This test is carried out by applying a controlled current pulse (I) between the working electrode and the counter electrode and the corresponding generated voltage (V) is measured relative to reference electrode as function of time, as shown in figure 2.8. In GCD measurements, upper and lower potential limits are set for the working electrodes. Once one of

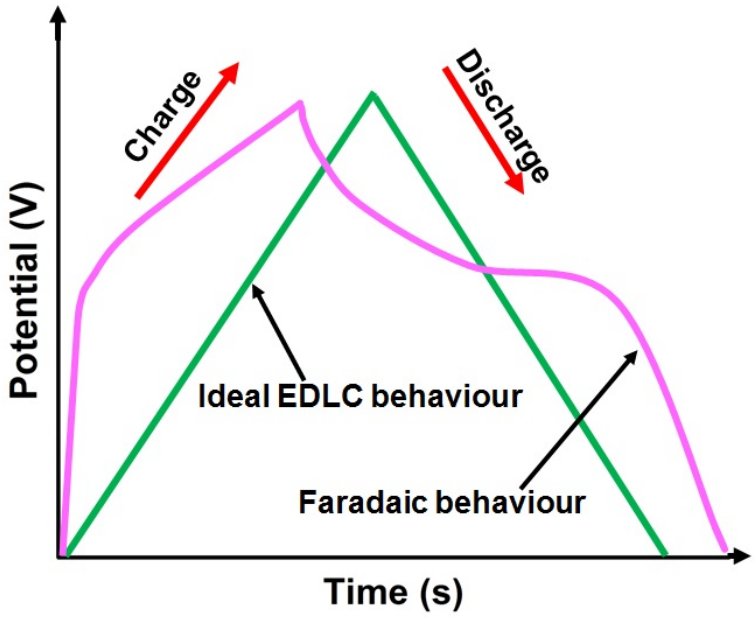

Figure 2.8: Typical CD curves of an ideal EDLC electrode and faradaic electrode.

the limits is reached the charge-discharge curve stop and the current reverses and the next step in the cycle begins (Figure 2.8. Similar to the CV plot, the CD curve reveals the behavior of the electrode as either electrochemical double layer capacitive (i.e. linear CD curve) or faradaic (i.e. non-linear CD curve due to faradic reactions) [69] as shown in figure 2.8.

The specific capacitance can also be calculated from GCD curves depending on the behavior the material is displaying. In GCD curves, the specific capacitance of the EDLC electrode can be calculated using the following equation [4,72-75]:

$$C_S = \frac{I \times \Delta t}{m \times \Delta V} \tag{2.5}$$

where Δt is the time taken for a complete discharge cycle (s), m is the total mass of the active material (g), ΔV is the potential window (V), and I is the current (A). In this case, specific capacitance is linear with time within the working potential window.

Moreover, if the working electrode show faradaic behavior the specific capacitance can be calculated by integrating the area under the GCD curve using the following equation:

$$C_S = \frac{2I}{mV^2} \int V dt \tag{2.6}$$

In this case, the specific capacitance is non-linear with time, hence it is preferred to report the specific capacity (Q_S) of faradaic material. The specific capacity of the electrodes can be calculated from the GCD curves, using the following equation [4,72-75]:

$$Q_S(mAhg^{-1}) = \frac{I}{m}\frac{t}{3.6} \tag{2.7}$$

where I is the applied current (A), m is the total mass of the active material (g), and t is the time taken for a complete discharge cycle (s).

Moreover, the energy density, E_d and the power density, P_d can be calculated

from the GCD curves, using the following equations:

$$E_d(Whkg^{-1}) = \frac{I}{m}\frac{\int V(t)dt}{3.6} \tag{2.8}$$

$$P_d(Wkg^{-1}) = \frac{3.6E_d}{\Delta t} \tag{2.9}$$

where I is the applied current (A), m is the total mass of the active material (g), $\int V(t)dt$ is the integral under the discharge curve from CD of the device, and Δt is the discharge time (s). The maximum power density of the device can further be calculated to show the maximum power the device can deliver. This can be calculated using the following equation:

$$P_{max} = \frac{V^2}{4mR_S} \tag{2.10}$$

where V is the potential window, m is the total mass of the active material, and R_S is solution resistance.

2.7.3 Electrochemical impedance spectroscopy (EIS)

To further evaluate the electrochemical behavior of the electrode materials (i.e., the conductivity and charge transport properties at the electrode/electrolyte interface) the EIS is used. EIS is a tool used for analyzing a single parameter and evaluation of mechanism of electrode

materials. It can be carried out at different voltages and thus analyzing the response of the material at different stages in the pure double layer range or in the redox regime. This is often represented as the Nyquist plot (imaginary component, Z'' versus the real component, Z' of the impedance), as shown in figure 2.9. EIS has attracted the attention of many researchers due to the concept of electrical resistance in electrical systems. Electrical resistance is basically the ability of the circuit element to resist the flow of electrical current. In addition, the EIS has also gained popularity since it can measure and give feedback on the electrical resistance in systems such as supercapacitors and Li-ion batteries(LIBs). In EIS, the broad range of physical and chemical phenomena is characterized by running a single experiment which covers a sufficient range of frequencies. The Bode plot is one of the important EIS plot which shows the impedance phase angle dependence on a frequency. As shown in figure 2.9, the Nyquis plot consists of the low-frequency region and the high-frequency region.

In the high-frequency region, the equivalent series (solution) resistance, R_S and the charge transfer resistance, R_{CT}, can be obtained [76]. The R_S and R_{CT} values represent the ohmic resistance of the electrodes and the charge-transfer kinetics (fast ion transport) respectively. In the low-frequency region, an ideal supercapacitor exhibits a vertical line parallel to the imaginary axis, however, in practice supercapacitors show deviation from this ideal behavior which is attributed to a leakage resistance, R_L arising from the faradaic charge transfer

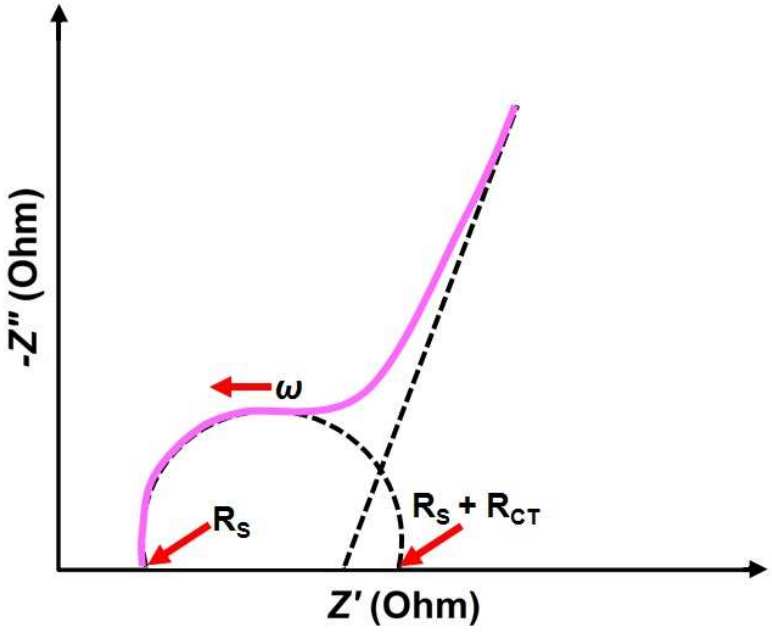

Figure 2.9: Nyquist impendance plot.

process [77,78]. The small R_S and R_{CT} values, i.e. $\approx$1 Ω indicate fast ion diffusion and low charge transfer resistance which suggest nearly an ideal capacitive performance of the electrodes/cell.

Furthermore, in the low-frequency region, the frequency dependence of the real and imaginary part of the capacitances ($C'(\omega)$ and $C''(\omega)$) can be evaluated using a complex capacitance model presented by the following equations [30,79]:

The impedance, $Z(\omega)$ given by

$$Z(\omega) = \frac{1}{j\omega \times C(\omega)} \tag{2.11}$$

can be written in the complex form as

$$Z(C) = Z'(\omega) + jZ''(\omega) \tag{2.12}$$

Therefore, equation 2.11 and 2.12 gives:

$$C(\omega) = \frac{1}{\omega \times (jZ'(\omega) - Z''(\omega))} = \frac{-(Z''(\omega) - jZ'(\omega))}{\omega |Z(\omega)|^2} \tag{2.13}$$

Thus, $C(\omega)$ in the complex form can be written as:

$$C(\omega) = C'(\omega) - jC''(\omega) \tag{2.14}$$

which gives

$$C'(\omega) = \frac{Z''(\omega)}{\omega |Z(\omega)|^2} \tag{2.15}$$

$$C''(\omega) = \frac{Z'(\omega)}{\omega |Z(\omega)|^2} \tag{2.16}$$

where Z' and Z'' are the real and the imaginary parts of the impedance, respectively, defined as

$$|Z(\omega)|^2 = Z'(\omega)^2 + Z''(\omega)^2 \tag{2.17}$$

and $\omega = 2\pi f$. $C'(\omega)$ is the real accessible capacitance that can be delivered and $C''(\omega)$ corresponds to energy loss by the irreversible process of the electrodes [79].

Bibliography

1. Y. Xie, Z. Song, S. Yao, H. Wang, W. Zhang, Y. Yao, et al., High capacitance properties of electrodeposited PANI-Ag nanocable arrays, Mater. Lett. 86 (2012) 77-79. doi:10.1016/j.matlet.2012.07.026.

2. W. Sun, X. Chen, Fabrication and tests of a novel three dimensional micro supercapacitor, Microelectron. Eng. 86 (2008) 1307-1310. doi:10.1016/j.mee.2008.12.010.

3. D.P. Dubal, S. V Patil, W.B. Kim, C.D. Lokhande, Supercapacitors based on electrochemically deposited polypyrrole nanobricks, Mater. Lett. 65 (2011) 2628-2631. doi:10.1016/j.matlet.2011.05.114.

4. P. Simon, Y. Gogotsi, Materials for electrochemical capacitors, Nat. Mater. 7 (2008) 845-854. doi:10.1038/nmat2297.

5. B.E. Conway, Electrochemical Supercapacitors Scientific Fundamentals and Technological Applications, Kluwer Academic Publishers, Plenum Press: New York, 1999.

6. J.R.J. Miller, A.F.A. Burke, Electrochemical capacitors: challenges and

opportunities for real-world applications, Electrochem. Soc. Interface. 17 (2008) 53.

7. A. Burke, R&D considerations for the performance and application of electrochemical capacitors, Electrochim. Acta. 53 (2007) 1083-1091. doi:10.1016/j.electacta.2007.01.011.

8. G. Feng, S. Li, V. Presser, P.T. Cummings, Molecular Insights into Carbon Supercapacitors Based on Room-Temperature Ionic Liquids, J. Phys. Chem. Lett. 4 (2013) 3367-3376. doi:10.1021/jz4014163.

9. X. Rui, H. Tan, Q. Yan, Nanostructured metal sulfides for energy storage, Nanoscale. 6 (2014) 9889. doi:10.1039/C4NR03057E.

10. G. Zhang, M. Kong, Y. Yao, L. Long, M. Yan, One-pot synthesis of γ-MnS/ reduced graphene oxide with enhanced performance for aqueous asymmetric supercapacitors, Nanotechnology 28 (2017) 065402. doi:10.1088/1361-6528/aa52a5.

11. G. Feng, S. Li, V. Presser, P.T. Cummings, Molecular Insights into Carbon Supercapacitors Based on Room-Temperature Ionic Liquids, J. Phys. Chem. Lett. 4 (2013) 3367-3376. doi:10.1021/jz4014163.

12. P. Simon, Y. Gogotsi, Materials for electrochemical capacitors, Nat. Mater. 7 (2008) 845-854. doi:10.1038/nmat2297.

13. G. Wang, L. Zhang, J. Zhang, A review of electrode materials for

electrochemical supercapacitors, Chem. Soc. Rev. 41 (2012) 797-828. doi:Doi 10.1039/C1cs15060j.

14. E. Frackowiak, S. Delpeux, K. Jurewicz, K. Szostaka, D. Cazorla-Amoros, F. Béguin, Enhanced capacitance of carbon nanotubes through chemical activation, Chem. Phys. Lett. 361 (2002) 35-41. doi:10.1016/S0009-2614(02)00684-X.

15. V. Ruiz, C. Blanco, E. Raymundo-Piñero, V. Khomenko, F. Béguin, R. Santamaría, Effects of thermal treatment of activated carbon on the electrochemical behaviour in supercapacitors, Electrochim. Acta. 52 (2007) 4969-4973. doi:10.1016/J.ELECTACTA.2007.01.071.

16. C. Peng, S. Zhang, D. Jewell, G.Z. Chen, Carbon nanotube and conducting polymer composites for supercapacitors, Prog. Nat. Sci. 18 (2008) 777-788. doi:10.1016/J.PNSC.2008.03.002.

17. C. Peng, J. Jin, G.Z. Chen, A comparative study on electrochemical co-deposition and capacitance of composite films of conducting polymers and carbon nanotubes, Electrochim. Acta. 53 (2007) 525-537. doi:10.1016/J.ELECTACTA.2007.07.004.

18. A. Malinauskas, J. Malinauskiene, A. Ramanavi?ius, Conducting polymer-based nanostructurized materials: electrochemical aspects, Nanotechnology. 16 (2005) R51-R62. doi:10.1088/0957-4484/16/10/R01.

19. S. Il Cho, S.B. Lee, Fast Electrochemistry of Conductive Polymer Nanotubes: Synthesis, Mechanism, and Application, Acc. Chem. Res. 41 (2008) 699-707. doi:10.1021/ar7002094.

20. Y.R. Ahn, M.Y. Song, S.M. Jo, C.R. Park, D.Y. Kim, Electrochemical capacitors based on electrodeposited ruthenium oxide on nanofibre substrates, Nanotechnology. 17 (2006) 2865-2869. doi:10.1088/0957-4484/17/12/007.

21. V.D. Patakea, C.D. Lokhandea, O.S. Joo, Electrodeposited ruthenium oxide thin films for supercapacitor: Effect of surface treatments, Appl. Surf. Sci. 255 (2009) 4192-4196. doi:10.1016/J.APSUSC.2008.11.005.

22. C.C. Hu, Y.H. Huang, K.H. Chang, Annealing effects on the physicochemical characteristics of hydrous ruthenium and ruthenium-iridium oxides for electrochemical supercapacitors, J. Power Sources. 108 (2002) 117-127. doi:10.1016/S0378-7753(02)00011-3.

23. J. Yan, T. Wei, J. Cheng, Z. Fan, M. Zhang, Preparation and electrochemical properties of lamellar MnO2 for supercapacitors, Mater. Res. Bull. 45 (2010) 210-215. doi:10.1016/J.MATERRESBULL.2009.09.016.

24. J. Jiang, A. Kucernak, Electrochemical supercapacitor material based on manganese oxide: preparation and characterization, Electrochim. Acta. 47 (2002) 2381-2386. doi:10.1016/S0013-4686(02)00031-2.

25. P.A. Nelson, J.R. Owen, A High-Performance Supercapacitor/Battery Hybrid Incorporating Templated Mesoporous Electrodes, J. Electrochem. Soc. 150 (2003) A1313. doi:10.1149/1.1603247.

26. M. Nakayama, A. Tanaka, Y. Sato, T. Tonosaki, K. Ogura, Electrodeposition of Manganese and Molybdenum Mixed Oxide Thin Films and Their Charge Storage Properties, Langmuir 21 (2005) 5907-5913. doi:10.1021/LA050114U.

27. K. Krishnamoorthy, G.K. Veerasubramani, S. Radhakrishnan, S.J. Kim, Supercapacitive properties of hydrothermally synthesized sphere like MoS2 nanostructures, Mater. Res. Bull. 50 (2014) 499-502. doi:10.1016/J.MATERRESBULL.2013.11.019.

28. J. Feng, X. Sun, C. Wu, L. Peng, C. Lin, S. Hu, et al., Metallic Few-Layered VS 2 Ultrathin Nanosheets: High Two-Dimensional Conductivity for In-Plane Supercapacitors, J. Am. Chem. Soc. 133 (2011) 17832-17838. doi:10.1021/ja207176c.

29. P. Justin, G.R. Rao, CoS spheres for high-rate electrochemical capacitive energy storage application, Int. J. Hydrogen Energy. 35 (2010) 9709-9715. doi:10.1016/J.IJHYDENE.2010.06.036.

30. T.M. Masikhwa, F. Barzegar, J.K. Dangbegnon, A. Bello, M.J. Madito, D. Momodu, et al., Asymmetric supercapacitor based on VS 2 nanosheets and activated carbon materials, RSC Adv. 6 (2016) 38990-39000.

doi:10.1039/C5RA27155J.

31. Y. Zhang, H. Feng, X. Wu, L. Wang, A. Zhang, T. Xia, H. Dong, X. Li, L. Zhang, Progress of electrochemical capacitor electrode materials: A review, Int. J. Hydrogen Energy. 34 (2009) 4889-4899. doi:10.1016/J.IJHYDENE.2009.04.005.

32. G. Wang, L. Zhang, J. Zhang, A review of electrode materials for electrochemical supercapacitors, Chem. Soc. Rev. 41 (2012) 797-828. doi:10.1039/C1CS15060J.

33. R. Kotz, M. Carlen, Principles and applications of electrochemical capacitors, Electrochim. Acta. 45 (2000) 2483-2498. doi:10.1016/S0013-4686(00)00354-6.

34. K.R. Prasad, K.K.N. Miura, Electrochemical Deposition of Nanostructured Indium Oxide: High-Performance Electrode Material for Redox Supercapacitors, Chem. Mater. 16 (2004) 1845-1847. doi:10.1021/CM0497576.

35. M. Kalaji, P.J. Murphy, G.O. Williams, The study of conducting polymers for use as redox supercapacitors, Synth. Met. 102 (1999) 1360-1361. doi:10.1016/S0379-6779(98)01334-4.

36. Y. Zhou, B. He, W. Zhou, J. Huang, X. Li, B. Wu, H. Li, Electrochemical capacitance of well-coated single-walled carbon nanotube with

polyaniline composites, Electrochim. Acta. 49 (2004) 257-262. doi:10.1016/J.ELECTACTA.2003.08.007.

37. P. Sharma, T.S. Bhatti, A review on electrochemical double-layer capacitors, Energy Convers. Manag. 51 (2010) 2901-2912. doi:10.1016/J.ENCONMAN.2010.06.031.

38. K.S. Ryu, K.M. Kim, N.G. Park, Y.J. Park, S.H. Chang, Symmetric redox supercapacitor with conducting polyaniline electrodes, J. Power Sources. 103 (2002) 305-309. doi:10.1016/S0378-7753(01)00862-X.

39. A. Clemente, S. Panero, E. Spila, B. Scrosati, Solid-state, polymer-based, redox capacitors, Solid State Ionics. 85 (1996) 273-277. doi:10.1016/0167-2738(96)00070-7.

40. A. Laforgue, P. Simon, C. Sarrazin, J.F. Fauvarque, Polythiophene-based supercapacitors, J. Power Sources. 80 (1999) 142-148. doi:10.1016/S0378-7753(98)00258-4.

41. C. Arbizzani, M. Mastragostino, F. Soavi, New trends in electrochemical supercapacitors, J. Power Sources. 100 (2001) 164-170. doi:10.1016/S0378-7753(01)00892-8.

42. Y.G. Wang, H.Q. Li, Y.Y. Xia, Ordered Whiskerlike Polyaniline Grown on the Surface of Mesoporous Carbon and Its Electrochemical Capacitance Performance, Adv. Mater. 18 (2006) 2619-2623.

doi:10.1002/adma.200600445.

43. H. Mi, X. Zhang, S. An, X. Ye, S. Yang, Microwave-assisted synthesis and electrochemical capacitance of polyaniline/multi-wall carbon nanotubes composite, Electrochem. Commun. 9 (2007) 2859-2862. doi:10.1016/j.elecom.2007.10.013.

44. M. Wu, G.A. Snook, V. Gupta, M. Shaffer, D.J. Fray, G.Z. Chen, Electrochemical fabrication and capacitance of composite films of carbon nanotubes and polyaniline, J. Mater. Chem. 15 (2005) 2297. doi:10.1039/b418835g.

45. M.J. Bleda-Martínez, C. Peng, S. Zhang, G.Z. Chen, E. Morallón, D. Cazorla-Amorós, Electrochemical Methods to Enhance the Capacitance in Activated Carbon/Polyaniline Composites, J. Electrochem. Soc. 155 (2008) A672. doi:10.1149/1.2956969.

46. D. Salinas-Torres, J.M. Sieben, D. Lozano-Castello, D. Cazorla-Amoros, E. Morallon, Asymmetric hybrid capacitors based on activated carbon and activated carbon fibre-PANI electrodes, Electrochim. Acta. 89 (2013) 326-333. doi:10.1016/j.electacta.2012.11.039.

47. K.S. Ryu, Y.-G. Lee, K.M. Kim, Y.J. Park, Y.-S. Hong, X. Wu, et al., Electrochemical capacitor with chemically polymerized conducting polymer based on activated carbon as hybrid electrodes, Synth. Met. 153 (2005) 89-92. doi:10.1016/j.synthmet.2005.07.167.

48. F. Chen, P. Liu, Q. Zhao, Well-defined graphene/polyaniline flake composites for high performance supercapacitors, Electrochim. Acta. 76 (2012) 62-68. doi:10.1016/j.electacta.2012.04.154.

49. G.A. Snook, P. Kao, A.S. Best, Conducting-polymer-based supercapacitor devices and electrodes, J. Power Sources. 196 (2010) 1-12. doi:10.1016/j.jpowsour.2010.06.084.

50. S. Bose, T. Kuila, A.K. Mishra, R. Rajasekar, N.H. Kim, J.H. Lee, Carbon-based nanostructured materials and their composites as supercapacitor electrodes, J. Mater. Chem. Mater. Chem. 22 (2012) 767-784. doi:10.1039/c1jm14468e.

51. C. Korzeniewski, B. E. Conway, Proceedings of the Symposium on the Electrochemical Double Layer, The Electrochemical Society, Inc., New Jersey: USA, 1997.

52. A.A. Khaleed, A. Bello, J.K. Dangbegnon, M.J. Madito, O. Olaniyan, F. Barzegar, K. Makgopa, K.O. Oyedotun, B.W. Mwakikunga, S.C. Rayd, N. Manyala, Solvothermal synthesis of surfactant free spherical nickel hydroxide/graphene oxide composite for supercapacitor application, J. Alloys Compd. 721 (2017) 80-91. doi:10.1016/J.JALLCOM.2017.05.310.

53. D.D. Zhao, S.J. Bao, W.J. Zhou, H.L. Li, Preparation of hexagonal nanoporous nickel hydroxide film and its application for electrochemical capacitor, Electrochem. Commun. 9 (2007) 869-874.

54. Y. Tang, T. Chen, S. Yu, Y. Qiao, S. Mu, J. Hu, et al., Synthesis of graphene oxide anchored porous manganese sulfide nanocrystals via the nanoscale Kirkendall effect for supercapacitors, J. Mater. Chem. A. 3 (2015) 12913-12919. doi:10.1039/C5TA02480C.

55. P.C. Chen, G. Shen, Y. Shi, H. Chen, C. Zhou, Preparation and Characterization of Flexible Asymmetric Supercapacitors Based on Transition-Metal-Oxide Nanowire/Single-Walled Carbon Nanotube Hybrid Thin-Film Electrodes, ACS Nano. 4 (2010) 4403-4411. doi:10.1021/nn100856y.

56. Y. Tang, T. Chen, S. Yu, Y. Qiao, S. Mu, S. Zhang, et al., A highly electronic conductive cobalt nickel sulphide dendrite/quasi-spherical nanocomposite for a supercapacitor electrode with ultrahigh areal specific capacitance, J. Power Sources. 295 (2015) 314-322. doi:10.1016/j.jpowsour.2015.07.035.

57. Y. Tang, T. Chen, S. Yu, Morphology controlled synthesis of monodispersed manganese sulfide nanocrystals and their primary application in supercapacitors with high performances, Chem. Commun. 51 (2015) 9018-9021. doi:10.1039/C5CC01700A.

58. L. Dong, C. Xu, Y. Li, Z.H. Huang, F. Kang, Q.H. Yang, et al., All-solid-state high performance asymmetric supercapacitors based on novel MnS nanocrystal and activated carbon materials, Sci. Rep. 6

(2016) 23289. doi:10.1038/srep23289.

59. F.O. Ochai-Ejeh, A. Bello, J. Dangbegnon, A.A. Khaleed, M.J. Madito, F. Bazegar, et al., High electrochemical performance of hierarchical porous activated carbon derived from lightweight cork (Quercus suber), J. Mater. Sci. 52 (2017) 10600-10613. doi:10.1007/s10853-017-1205-4.

60. A.A. Mirghni, M.J. Madito, T.M. Masikhwa, K.O. Oyedotun, A. Bello, N. Manyala, Hydrothermal synthesis of manganese phosphate/graphene foam composite for electrochemical supercapacitor applications, J. Colloid Interface Sci. (2017). doi:10.1016/j.jcis.2017.01.098.

61. F. Barzegar, A. Bello, D. Momodu, M.J. Madito, J. Dangbegnon, N. Manyala, Preparation and characterization of porous carbon from expanded graphite for high energy density supercapacitor in aqueous electrolyte, J. Power Sources. 309 (2016) 245-253. doi:10.1016/j.jpowsour.2016.01.097.

62. M.R. Lukatskaya, B. Dunn, Y. Gogotsi, Multidimensional materials and device architectures for future hybrid energy storage, Nat. Commun. 7 (2016) 12647. doi:10.1038/ncomms12647.

63. K. Naoi, W. Naoi, S. Aoyagi, J. Miyamoto, T. Kamino, New Generation "Nanohybrid Supercapacitor", Acc. Chem. Res. 46 (2013) 1075-1083. doi:10.1021/ar200308h.

64. K. Chen, D. Xue, Electrochemically Stabilized Porous Nickel Foam as Current Collector and Counter Electrode in Alkaline Electrolyte for Supercapacitor, J. Nanoeng. Nanomanufacturing. 4 (2014) 50-55. doi:10.1166/jnan.2014.1168.

65. Y.F. Yuan, X.H. Xia, J.B. Wu, J.L. Yang, Y.B. Chen, S.Y.Guo, Nickel foam-supported porous Ni(OH)2/NiOOH composite film as advanced pseudocapacitor material, Electrochim. Acta. 56 (2011) 2627-2632. doi:10.1016/J.ELECTACTA.2010.12.001.

66. Y. Zhao, K. Chen, C. Sun, K. Li, C. Meng, D. Xue, Pseudocapacitance Performances of Naked Porous Nickel Foams, Mater. Focus. 2 (2013) 239-243. doi:10.1166/mat.2013.1081.

67. L. Jiang, R. Zou, W. Li, J. Sun, X. Hu, Y. Xue, et al., $Ni(OH)_2$ /CoO/reduced graphene oxide composites with excellent electrochemical properties, J. Mater. Chem. A. 1 (2013) 478-481. doi:10.1039/C2TA00265E.

68. Y. Zhang, C. Sun, P. Lu, K. Li, S. Song, D. Xue, Crystallization design of MnO_2 towards better supercapacitance, CrystEngComm. 14 (2012) 5892. doi:10.1039/c2ce25610j.

69. D. Weingarth, M. Zeiger, N. Jockel, M. Aslan, G. Feng, V. Presser, Graphitization as a Universal Tool to Tailor the Potential-Dependent Capacitance of Carbon Supercapacitors, Adv. Energy Mater. 4 (2014) 1400316. doi:10.1002/aenm.201400316.

70. R. Signorelli, D.C. Ku, J.G. Kassakian, J.E. Schindall, Electrochemical Double-Layer Capacitors Using Carbon Nanotube Electrode Structures, Proc. IEEE. 97 (2009) 1837-1847. doi:10.1109/JPROC.2009.2030240.

71. B.E. Conway, W.G. Pell, Double-layer and pseudocapacitance types of electrochemical capacitors and their applications to the development of hybrid devices, J. Solid State Electrochem. 7 (2003) 637-644. doi:10.1007/s10008-003-0395-7.

72. B. Akinwolemiwa, C. Peng, G.Z. Chen, Redox electrolytes in supercapacitors, J. Electrochem. Soc. 162 (2015) A5054-A5059. doi:10.1149/2.0111505jes.

73. A. Laheoor, P. Przygocki, Q. Abbas, F. Boguin, Appropriate methods for evaluating the efficiency and capacitive behavior of different types of supercapacitors, 2015. doi:10.1016/j.elecom.2015.07.022.

74. K.O. Oyedotun, M.J. Madito, A. Bello, D.Y. Momodu, A.A. Mirghni, N. Manyala, Investigation of graphene oxide nanogel and carbon nanorods as electrode for electrochemical supercapacitor, Electrochim. Acta. (2017). doi:10.1016/j.electacta.2017.05.150.

75. G. Godillot, L. Guerlou-Demourgues, P.-L. Taberna, P. Simon, C. Delmas, Original Conductive Nano-Co3O4 Investigated as Electrode Material for Hybrid Supercapacitors, Electrochem. Solid-State Lett. 14 (2011) A139. doi:10.1149/1.3609259.

76. Y. Zhou, H. Xu, N. Lachman, M. Ghaffari, S. Wu, Y. Liu, et al., Advanced asymmetric supercapacitor based on conducting polymer and aligned carbon nanotubes with controlled nanomorphology, Nano Energy. 9 (2014) 176-185.

77. W. Sun, X. Chen, Preparation and characterization of polypyrrole films for three-dimensional micro supercapacitor, 193 (2009) 924-929. doi:10.1016/j.jpowsour.2009.04.063.

78. H. Li, J. Wang, Q. Chu, Z. Wang, F. Zhang, S. Wang, Theoretical and experimental specific capacitance of polyaniline in sulfuric acid, 190 (2009) 578-586. doi:10.1016/j.jpowsour.2009.01.052.

79. P.L. Taberna, P. Simon, J.-F.F. Fauvarque, Electrochemical Characteristics and Impedance Spectroscopy Studies of Carbon-Carbon Supercapacitors, J. Electrochem. Soc. 150 (2003) A292-300. doi:10.1149/1.1543948.

PART III

EXPERIMENTAL DETAILS

Chapter 3

Characterization techniques

3.1 Introduction

The synthesized materials that were investigated in this study were characterized using various techniques (X-ray diffraction (XRD), Raman spectroscopy, Fourier transform infrared (FTIR) spectroscopy, scanning electron microscopy (SEM), energy-dispersive X-ray spectrometer (EDS), transmission electron microscopy (TEM) and X-ray photoelectron spectroscopy (XPS)) and this chapter provides an introductory overview of these techniques. The structure, morphology and elemental composition of the materials were investigated using XRD, Raman spectroscopy, FTIR spectroscopy, SEM, TEM and EDS, respectively. The chemical state of the elements of the synthesized materials was investigated using XPS. In materials characterization, these techniques have proven to be complementary to each other for detail analyses.

3.2 X-ray diffraction

X-ray powder diffraction is an analytical technique (non-destructive technique) primarily used for bulk phase identification (i.e., crystal structures and atomic spacing (d-spacing)) of crystalline samples. It can also be used in studying grains sizes, lattice constants, and degree of crystallinity in a mixture of amorphous and crystalline materials [1].

During XRD operation, X-rays generated by a cathode ray tube (X-ray tube) are filtered (to produce monochromatic radiation), collimated and directed towards the sample (Figure 3.1(a)). The interaction of the incident X-rays with the sample produces diffracted rays (constructive interference) when conditions satisfy Bragg's Law. Briefly, considering the incident and diffracted X-rays from the atomic layers, as shown in figure 3.1(b), where the angle of incidence is given by θ, and the angle 2θ gives the experimentally measured diffraction angle. The total path difference, x, between the X-rays marked 1 and 2 when they arrive at the detector, point A and B respectively, is given by [1]

$$x = 2d\sin\theta \tag{3.1}$$

For constructive interference the path difference is equal to a whole number of wavelengths, $n\lambda$, where n is a whole number. As a result, equation 3.1 becomes

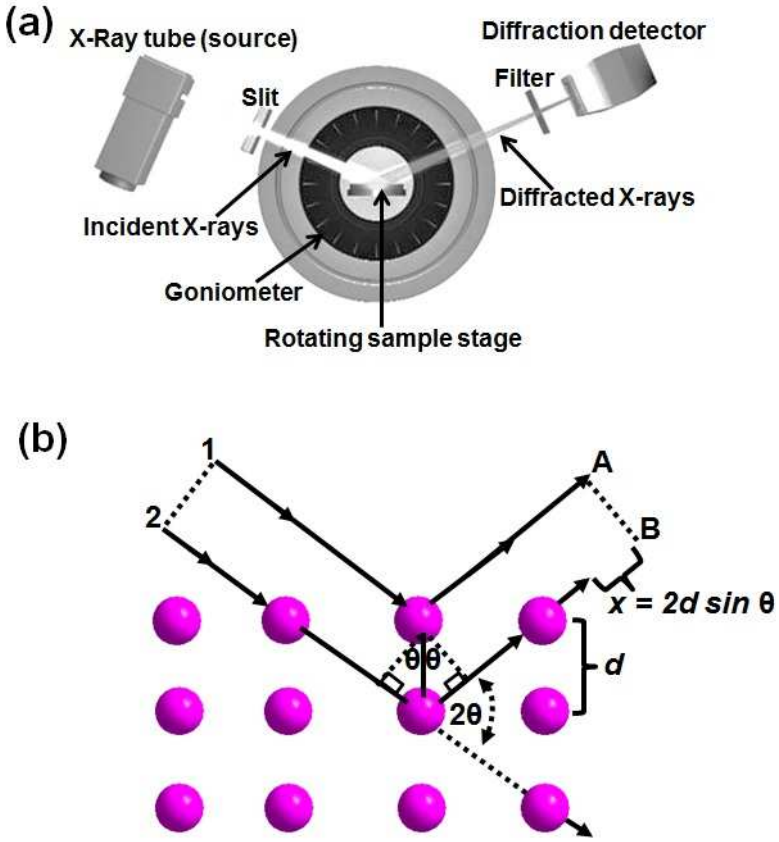

Figure 3.1: (a) Basic components of X-ray diffractometers showing the X-Ray source/tube and detector relative to the sample. (b) Schematic illustration of the diffraction of incident X-rays by atomic planes.

Bragg's Law

$$n\lambda = 2d\sin\theta \tag{3.2}$$

where n is a positive integer, λ is the wavelength of incident X-rays, d is the interplanar spacing and θ is the scattering angle.

Since the wavelength of the incident X-rays is known, e.g. for Cu $\lambda =$ 0.15406 nm and for Co $\lambda = 0.17890$ nm, and the angles at which constructive

interference occurs are measured by goniometer (Figure 3.1(a)), the use of the Bragg's equation 3.2 allows determining the d spacing of the materials. Therefore, the XRD result is a plot of scattered X-ray intensity versus the scattering angle 2θ which is unique for each material (see figure 3.2 for VS_2).

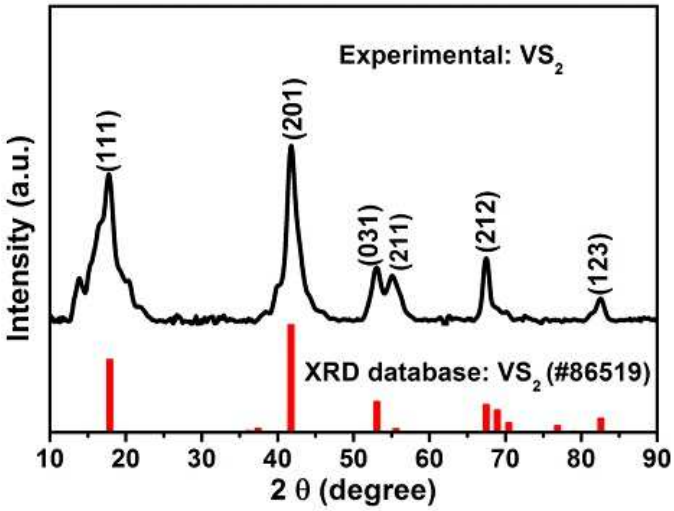

Figure 3.2: The XRD pattern of the VS_2 nanosheets and the best matching ICSD card from XRD database. (Adopted from this study).

Usually, to obtain the phase data of the material which is analysed with XRD, the measured XRD pattern is compared to the database patterns to find the best matching standard (Figure 3.2). On the other hand, the matching standard can be used to generate a unit cell or a molecule using appropriate software, e.g. diamond crystal and molecular structure visualization software, as shown for VS_2 in figure 3.3.

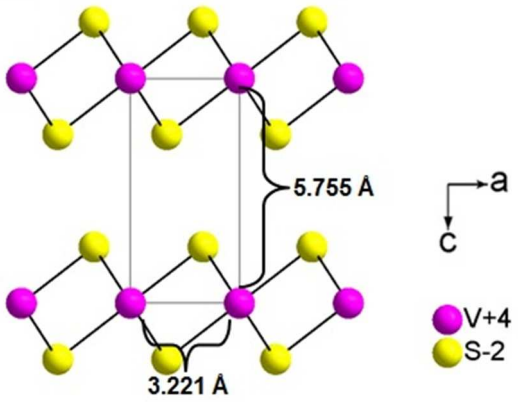

Figure 3.3: The unit cell of the VS_2 based on the best matching ICSD card. (Adopted from this study).

3.3 Raman spectroscopy

Raman spectroscopy is a non-destructive technique which has a high molecular specificity, making it an excellent technique for materials analysis. It provides information about chemical structure/phase, crystallinity and molecular interactions (i.e. structural information).

In Raman spectroscopy, there is a scattering of incident photons (from primary laser light source) by phonons (vibrational modes) upon the interaction of photons with the chemical bonds within a material, as demonstrated in figure 3.4). The interaction of incident photons of energy $\hbar\omega_L$ with the chemical bonds within a sample creates a time-dependent perturbation which increases the ground state energy (E_{GS}) to a total energy of $E_{GS} + \hbar\omega_L$ making a system (molecule) to be unstable [2,3]. Since the system has no stationary state (i.e. is in the unstable situation), the photon is emitted by the perturbed system and the system goes back to the stationary state (ground state), and if the

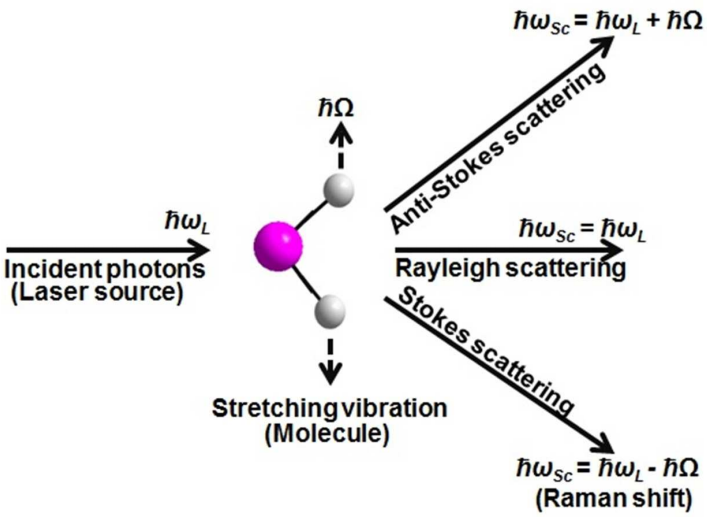

Figure 3.4: Schematic illustration of light scattering by Rayleigh, Stokes and Anti-Stokes scattering processes in a vibrating molecule due to the time-dependent perturbation introduced by incident photons.

frequency of the emitted photon (ω_{Sc}) is the same as the incident one, ω_L (i.e. elastic scattering), this is referred to as Rayleigh scattering (Figure 3.4) [2,4]. On the other hand, as the molecule returns to a ground state a photon can lose part of its energy in the interaction process and scatted from the sample with a lower energy $\hbar\omega_{Sc} = \hbar\omega_L - \hbar\Omega$, where $\hbar\Omega$ is a phonon energy. This process is referred to as Stokes process (inelastic scattering) [2,4]. Additionally, if the molecule is in the excited vibrational state, and after the photon interaction the molecule returns to its ground state, the photon leaves the sample with an increased energy $\hbar\omega_{Sc} = \hbar\omega_L + \hbar\Omega$. This process is referred to as Anti-Stokes process [2,4].

Therefore, between Stokes and Anti-Stokes processes, Stokes process is the most probable, hence Raman spectra are Stokes measurements plots of the

intensity of the scattered photon as a function of the difference between incident and scattered photon energy (i.e. Raman shift /or Wavenumber) [2]. Generally, a Raman spectroscopy has a high molecular specificity hence the spectrum reveal peaks which correspond to a specific molecular bond vibration, as shown for VS_2 in figure 3.5. The Raman spectrum of VS_2 reveals vibration bands at 140, 285 and 405 cm^{-1} which are E_{1g}, E_{2g} and A_{1g} respectively, corresponding to the in-plane (E) and out-of-plane (A) stretching modes of S−V−S [5,6].

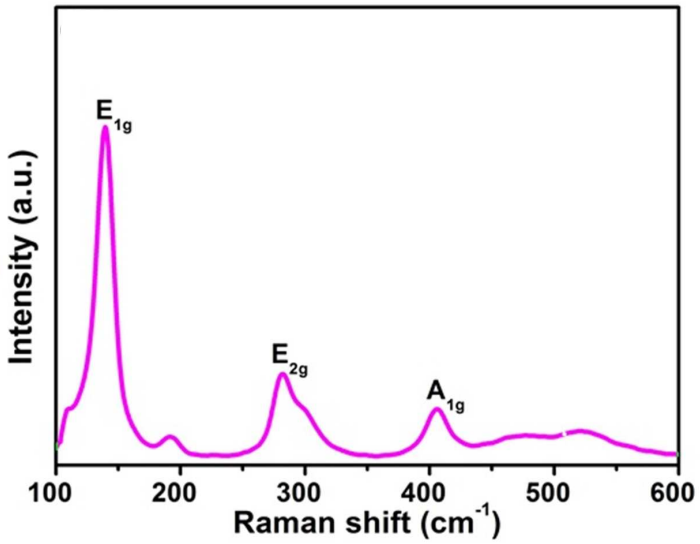

Figure 3.5: The Raman spectrum of the VS_2 nanosheets (Adopted from this study).

To briefly explain how the Rayleigh scattering are eliminated from the Raman measurements, figure 3.6 is presented which gives an overview of key instrumental components of a typical Raman system. However, in practice there are numerous Raman spectroscopic variations available depending on the instrument manufacture. For instance, the beam path will be

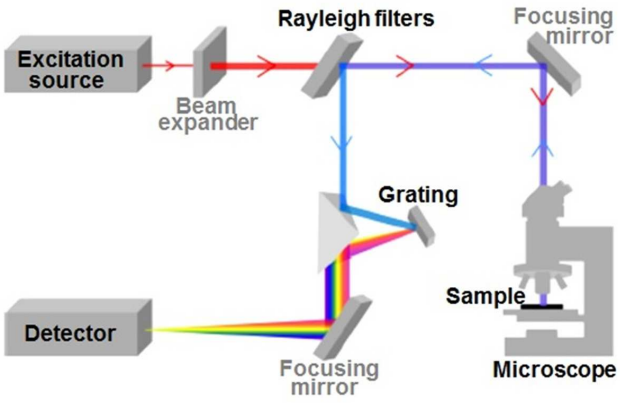

Figure 3.6: Schematic illustration of fundamental instrumental components of a typical Raman system (Adopted from Ref. [8]).

slightly different and may have additional optical components for different manufactures. It can be seen from the figure that Rayleigh scattering are optically filtered and filters are specific to the laser wavelength [7]. Filters are used in conjunction with diffraction grating which is used to disperse the Raman scattered light.

Furthermore, to detect the weak intensity of Raman scattering, the detector needs to be extremely sensitive hence charge-coupled devices (CCDs) are commonly used in Raman detector, because they exhibit high quantum efficiencies and low signal-to-noise ratios [8]. In CCDs, a charge collected from scattered photons is directly proportional to the Raman scattering intensity. There are several laser source options available within Raman systems or some of the Raman systems, and a choice of each laser source is determined mainly by the desired wavelength and the desired spot size. Based on the choice of the laser source and the material, the Raman spectrum might

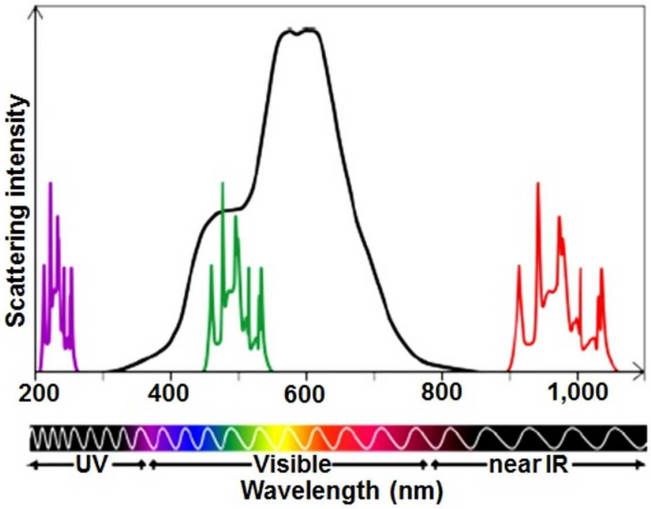

Figure 3.7: Simplified overview of the effect of laser excitation wavelength on the fluorescence background (Adopted from Ref. [8]). A 532 nm laser (green line), is largely susceptible to fluorescence background (black line), whereas high-energy UV (purple) and lower-energy IR (red) wavelengths are relatively free of fluorescence.

consist of fluorescence contribution (shown by black line in figure 3.7) which can be avoided by exciting the sample with a wavelength that falls outside fluorescence region, e.g. UV (purple) and lower-energy IR (red) wavelengths [8].

3.4 Fourier transform infrared spectroscopy

Infrared (IR) spectroscopy is a non-destructive analytical technique which is mainly used to identify organic and inorganic materials. Generally, the spectroscopy systems used to detect molecular vibrations in materials are based on the processes of infrared absorption (transmittance) and Raman scattering, and are widely used to provide information on chemical structures

and molecular interactions (structural information).

Similar to Raman spectroscopy, in IR spectroscopy there is a scattering of incident photons by vibrational modes upon the interaction of photons with the chemical bonds within a material (Figure 3.4). However, in addition to the Stokes scattering (Raman shift) emitted by the perturbed molecule which is exactly what is measured in IR spectroscopy, each peak represents the percentage of light transmitted through the sample. Hence, the intensity scale (y-axis) in IR plots is given as transmittance percentage (Figure 3.8). Figure 3.8 shows the IR plot of PANI which is compared to the Raman spectrum, and from the two spectra it can be seen that the main peaks which reveal the functionalities of PANI are within the same range of wavenumber.

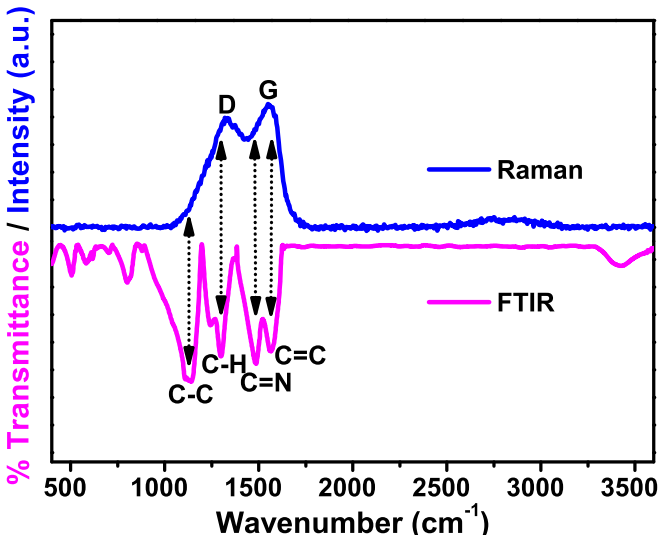

Figure 3.8: The Raman and FTIR vibration spectra of PANI (Adopted from this study).

In view of instrumentation, most commercial IR instruments measure IR radiation using Fourier transform spectrometers, hence the technique is

known as Fourier transform infrared (FTIR) spectroscopy [9]. A simplified layout of a typical FTIR spectrometer is shown in figure 3.9. The basic components of the FTIR spectrometer are a radiation source, an interferometer, mirrors and a detector. A Fourier transform spectrometer uses the configuration of mirrors and beam splitter, and one of the mirrors can be moved rapidly back and forth. A rapid mirror motions result in significant noise reduction. Fourier transform spectrometers are used primarily in the infrared region of the spectrum.

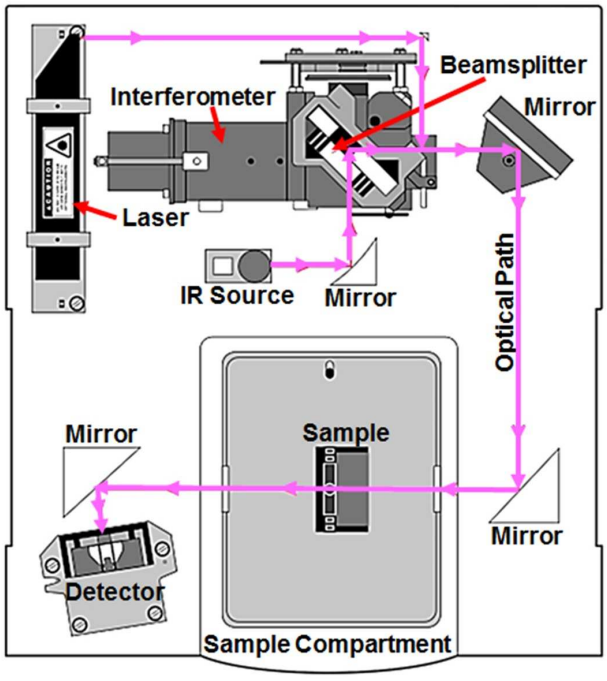

Figure 3.9: A simplified layout of a typical FTIR spectrometer (Adopted from Ref. [10]).

3.5 Scanning electron microscopy and energy dispersive X-ray spectroscopy

Scanning electron microscopy is a non-destructive technique which is mainly used for imaging the surfaces of almost any material on a micro to nanometre scale. The technique uses a beam of focused electrons under ultra-high vacuum conditions to obtain high levels of magnification and resolution for imaging. The image resolution offered by SEM depends not only on the parameters of the electron beam, but also on the interaction of the electron beam with the sample. Typically, the SEM analyses can yield information about topography, morphology, composition and crystallography of materials using other analysers intergraded in SEM system [11]. When a focused beam of high-energy primary electrons impinges the surface of a sample, among others (Figure 3.10(a)), it generates low energy secondary electrons with energies typically smaller than 50 eV [12]. Therefore, an image of the sample surface (topography/ morphology) is constructed by measuring the intensity of these secondary electrons as a function of the position of the scanning primary electron beam [11]. Field Emission SEM produces high resolution images, unique image contrast and a large depth of field. Figure 3.10(b), shows the low and high magnification (inset to the figure) SEM images of the layered structure of VS_2 which displays the nanosheets morphology of the sample.

Furthermore, X-rays which are ejected when an incident electron beam strikes a sample can be characterized by an energy dispersive X-ray spectroscopy

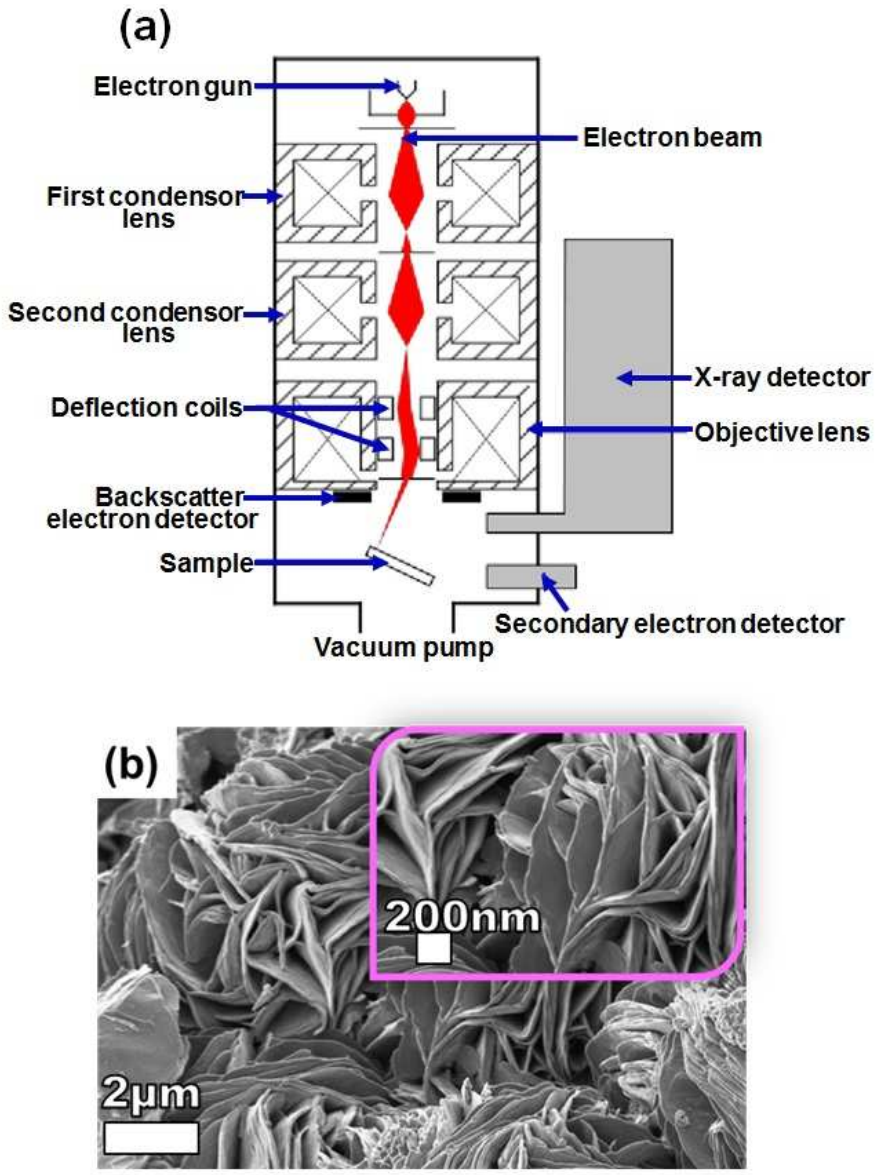

Figure 3.10: (a) A schematic diagram of a typical scanning electron microscopy (Adopted from Ref. [13]). (b) Low and high magnification (insert figure) SEM images of the layered structure of VS_2 (Adopted from this study).

(EDS) if the X-ray spectrometer (detector) is attached to the SEM system (Figure 3.10(a)). Since each element has a unique energy difference between outer and inner electron shells, the X-rays that are detected yield elemental identification hence EDS analysis gives elemental composition of the sample.

3.6 Transmission electron microscopy

Transmission electron microscopy is a non-destructive high spatial resolution characterization tool. It uses a beam of focused high-energy electrons (under ultra-high vacuum conditions) which is transmitted through a thin sample (Figure 3.11(a)) and interacts with the sample as it passes through. The transmitted electrons are used to generate an image of a sample. Different types of images can be obtained in TEM from different interactions of electron beam with a sample. For instance, an image of electron diffraction patterns is obtained from elastically scattered electrons (diffracted beam), bright field image from unscattered electrons (transmitted beam) and dark field image from elastically scattered electrons (diffracted beam) [11,14]. TEM can be used to characterize samples to obtain information about particle size, shape, crystallinity, and interparticle interaction.

Figure 3.11(b) shows typical bright field TEM image (at low magnification) of carbonized Fe/PANI sample which displays Fe dispersion on PANI. In this figure, a contrast in the image is caused by attenuation of the transmitted beam in dense (high atomic number) areas of the sample.

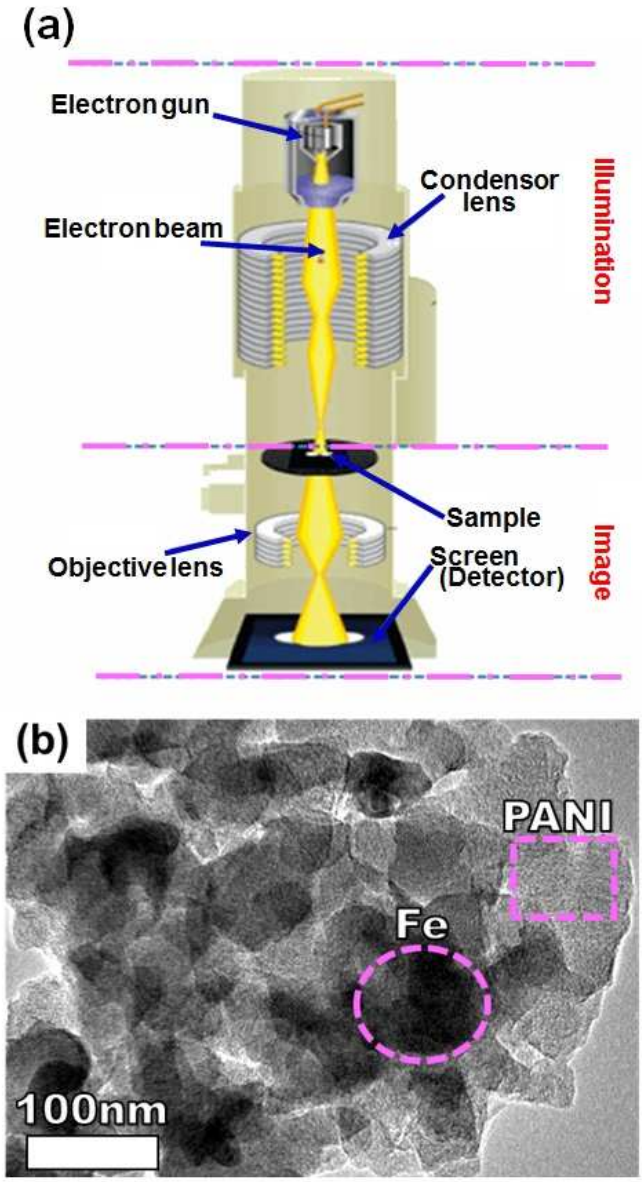

Figure 3.11: (a) Schematic diagram of a TEM (Adopted from Ref. [15]). (b) A TEM image of carbonized Fe/PANI (C-Fe/PANI) (Adopted from this study).

3.7 X-ray photoelectron spectroscopy

X-ray photoelectron spectroscopy is a surface-sensitive quantitative technique that measures the elemental composition, chemical state and electronic state

of the elements within a sample. The high surface specificity of XPS is achieved by using smaller angles of incidence or exit of the photoelectrons. Additionally, the mean free path of the detected photoelectrons is in the order of a few nm which corresponds to the topmost surface atomic layers of the sample [16]. XPS involves irradiation of the sample with a beam of X-rays (Al-Kα or Mg-Kα) while measuring the number and the kinetic energy of elastically scattered photoelectrons of the analysed sample [16]. The kinetic energy of the ejected electrons (photoelectrons) depends upon the photon energy ($h\nu$) and the binding energy of the electron in the core-shell of an atom and is usually analysed with a hemispherical energy analyser (see Figure 3.12(a)). Generally, XPS analysis is coupled with ion sputtering with noble gas ions (e.g. Ar^{+}) for surface cleaning and depth profiling and analysis are carried out under ultra-high vacuum conditions. In XPS spectrum, peaks appear from atoms emitting electrons of a particular characteristic energy. The energies and intensities of these electrons (photoelectron peaks) enable identification and quantification of the surface chemistry of a material, as shown in figure 3.12(b). Briefly, figure 3.12(b) shows the XPS core level spectrum of V 2p photoelectrons of the VS_2 sample and the fitted binding energy peaks of the V $2p_{3/2}$ core level confirm the predominance content of V^{4+} oxidation state in the sample.

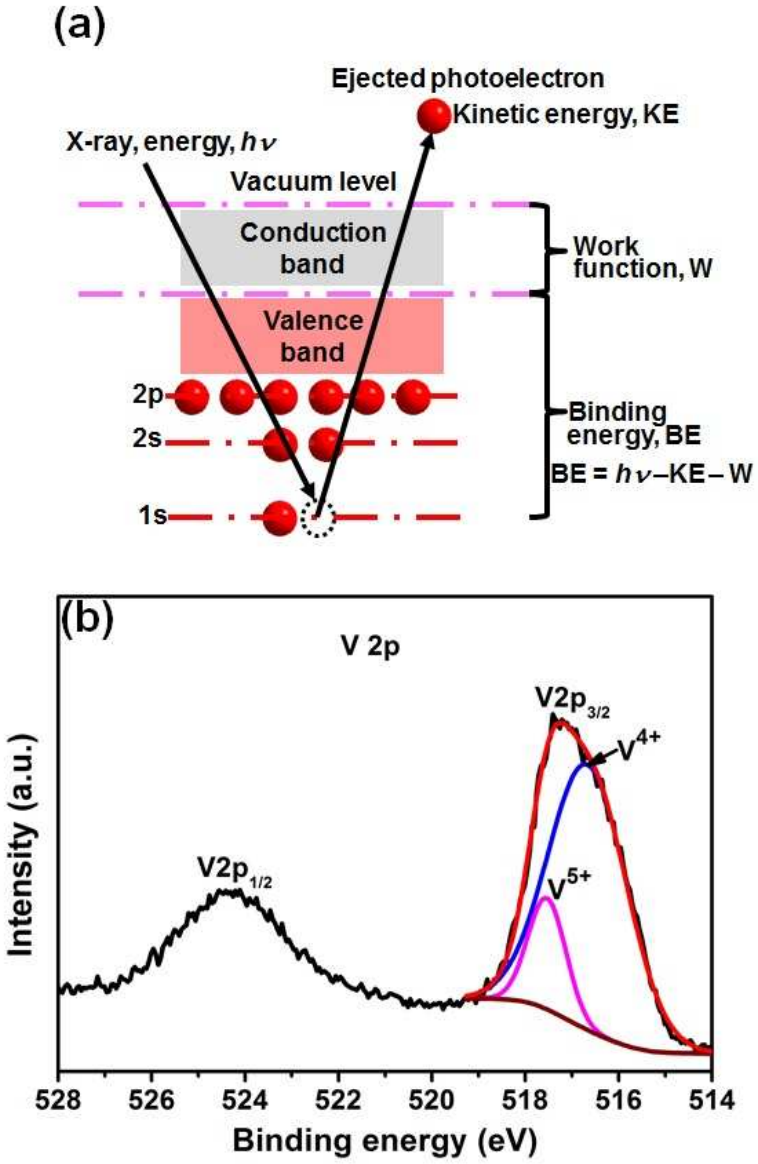

Figure 3.12: (a) Schematic view of the photoemission process in XPS: Incident photon energy, $h\nu$ is absorbed by a core level electron, if $h\nu >$ BE then the electron is ejected from the atom with kinetic energy, KE. This is then detected by an analyser and the binding energy, BE of the ejected electron is determined by, BE = $h\nu$ - KE - W, where W is the work function of the electron analyser, not the analysed material. (b) The XPS core level spectrum of vanadium, V 2p of the VS_2 nanosheets (Adopted from this study).

Bibliography

1. A.C. Ferrari, D.M. Basko, Raman spectroscopy as a versatile tool for studying the properties of graphene, Nature Nanotechnology. 8 (2013) 235-46.

2. H. Aoki, M. S. Dresselhaus, eds., Physics of Graphene, Springer, New York, 2014.

3. C. Casiraghi, A. Hartschuh, E. Lidorikis, H. Qian, H. Harutyunyan, T. Gokus, et al., Rayleigh imaging of graphene and graphene layers, Nano Letters. 7 (2007) 2711-7.

4. A.C. Ferrari, J.C. Meyer, V. Scardaci, C. Casiraghi, M. Lazzeri, F. Mauri, et al., Raman Spectrum of Graphene and Graphene Layers, Physical Review Letters. 97 (2006) 187401.

5. L.M. Malard, M.A. Pimenta, G. Dresselhaus, M.S. Dresselhaus, Raman spectroscopy in graphene, Physics Reports. 473 (2009) 51-87.

6. J.M. Caridad, F. Rossella, V. Bellani, M.S. Grandi, E. Diez, Automated detection and characterization of graphene and few-layer graphite via

Raman spectroscopy, Journal of Raman Spectroscopy. 42 (2011) 286-293.

7. J.M. Caridad, F. Rossella, V. Bellani, M. Maicas, M. Patrini, E. Diez, Effects of particle contamination and substrate interaction on the Raman response of unintentionally doped graphene, Journal of Applied Physics. 108 (2010) 084321.

8. M.J. Madito, A. Bello, J.K. Dangbegnon, C.J. Oliphant, W.A. Jordaan, T.M. Masikhwa, et al., Raman analysis of bilayer graphene film prepared on commercial Cu(0.5 at% Ni) foil, Journal of Raman Spectroscopy. J. Raman Spectrosc. 47 (2016) 553Ű559. doi:10.1002/jrs.4848.

9. J.N. Fuchs, Dirac fermions in graphene and analogues: magnetic field and topological properties. arXiv preprint arXiv:1306.0380 (2013)

10. M. Lazzeri, C. Attaccalite, L. Wirtz, F. Mauri, Impact of the electron-electron correlation on phonon dispersion: Failure of LDA and GGA DFT functionals in graphene and graphite, Physical Review B. 78 (2008) 081406.

11. M.S. Dresselhaus, A. Jorio, R. Saito, Characterizing Graphene, Graphite, and Carbon Nanotubes by Raman Spectroscopy, Annual Review of Condensed Matter Physics. 1 (2010) 89-108.

12. A.C. Ferrari, J. Robertson, Interpretation of Raman spectra of disordered and amorphous carbon, Physical Review B. 61 (2000) 14095-14107.

13. M.J. Madito, A. Bello, J.K. Dangbegnon, C.J. Oliphant, W.A. Jordaan, D.Y. Momodu, et al., A dilute Cu(Ni) alloy for synthesis of large-area Bernal stacked bilayer graphene using atmospheric pressure chemical vapour deposition, Journal of Applied Physics. 119 (2016) 015306.

14. M. Freitag, Graphene: Trilayers unravelled, Nature Physics. 7 (2011) 596-597.

15. Y. Zhang, T. Tang, C. Girit, Z. Hao, M.C. Martin, A. Zettl, et al., Direct observation of a widely tunable bandgap in bilayer graphene, Nature. 459 (2009) 820-3.

16. W. Fang, A.L. Hsu, R. Caudillo, Y. Song, A.G. Birdwell, E. Zakar, et al., Rapid identification of stacking orientation in isotopically labeled chemical-vapor grown bilayer graphene by Raman spectroscopy, Nano Letters. 13 (2013) 1541-1548.

17. S. Chen, W. Cai, R.D. Piner, J.W. Suk, Y. Wu, Y. Ren, et al., Synthesis and characterization of large-area graphene and graphite films on commercial Cu-Ni alloy foils, Nano Letters. 11 (2011) 3519-3525.

18. W. Liu, S. Kraemer, D. Sarkar, H. Li, P.M. Ajayan, K. Banerjee, Controllable and rapid synthesis of high-quality and large-area bernal stacked bilayer graphene using chemical vapor deposition, Chemistry of Materials. 26 (2014) 907-915.

19. R.F. Egerton, Physical Principles of Electron Microscopy: An Introduction to TEM, SEM, and AEM, Springer Science & Business Media, 2006.

20. A.W. Robertson, J.H. Warner, Atomic resolution imaging of graphene by transmission electron microscopy, Nanoscale. 5 (2013) 4079-93.

21. M.J. Madito, N. Manyala, A. Bello, J.K. Dangbegnon, T.M. Masikhwa, D.Y. Momodu, A wafer-scale Bernal-stacked bilayer graphene film obtained on a dilute Cu (0.61 at% Ni) foil using atmospheric pressure chemical vapour deposition, RSC Adv. 6 (2016) 28370-28378.

22. A. Dato, V. Radmilovic, Z. Lee, J. Phillips, M. Frenklach, Substrate-Free Gas-Phase Synthesis of Graphene Sheets, Nano Letters. 8 (2008) 2012-2016.

23. J.C. Meyer, A.K. Geim, M.I. Katsnelson, K.S. Novoselov, T.J. Booth, S. Roth, The structure of suspended graphene sheets, Nature. 446 (2007) 60-3.

24. Y. Wu, H. Chou, H. Ji, Q. Wu, S. Chen, W. Jiang, et al., Growth Mechanism and Controlled Synthesis of AB-Stacked Bilayer Graphene on Cu-Ni Alloy Foils, ACS Nano. (2012) 7731-7738.

25. Atomic Force Microscopy - What is it?, http://www.keysight.com/main/editorial.jspx?ckey=1774141&lc=eng&cc=ZA (accessed March 27,

2016).

26. A. Gupta, G. Chen, P. Joshi, S. Tadigadapa, P.C. Eklund, Raman scattering from high-frequency phonons in supported n-graphene layer films, Nano Letters. 6 (2006) 2667-73.

27. Z.H. Ni, H.M. Wang, J. Kasim, H.M. Fan, T. Yu, Y.H. Wu, et al., Graphene thickness determination using reflection and contrast spectroscopy, Nano Letters. 7 (2007) 2758-2763.

28. S. Ye, H. Huang, C. Yuan, F. Liu, M. Zhai, X. Shi, et al., Thickness-Dependent Strain Effect on the Deformation of the Graphene-Encapsulated Au Nanoparticles, Journal of Nanomaterials. 2014 (2014) 1-6.

29. P. Nemes-Incze, Z. Osvo Th, K. Kamaro S, L.P. Biro, Anomalies in thickness measurements of graphene and few layer graphite crystals by tapping mode atomic force microscopy, CARBON 46 (2008) 1435-1442.

30. M. Fabiane, Chemical vapour deposition of graphene: Fundamental aspects of synthesis and characterization, PhD thesis, University of Pretoria, 2014.

31. Molecular Expressions Microscopy Primer: Anatomy of the Microscope-Introduction, http://micro.magnet.fsu.edu/ primer/anatomy/introduction.html (accessed March 25, 2016).

32. X. Wang, M. Zhao, D.D. Nolte, Optical contrast and clarity of graphene on an arbitrary substrate, Applied Physics Letters. 95 (2009) 2009-2011.

33. P. Blake, E.W. Hill, A.H. Castro Neto, K.S. Novoselov, D. Jiang, R. Yang, et al., Making graphene visible, Applied Physics Letters. 91 (2007) 2007-2009.

34. H. Zhou, W.J. Yu, L. Liu, R. Cheng, Y. Chen, X. Huang, et al., Chemical vapour deposition growth of large single crystals of monolayer and bilayer graphene, Nature Communications. 4 (2013) 2096.

35. X. Tang, N. Reckinger, O. Poncelet, P. Louette, F. Ureï£¡a, H. Idrissi, et al., Damage evaluation in graphene underlying atomic layer deposition dielectrics, Scientific Reports. 5 (2015) 13523.

36. M.P. Seah, Quantification of AES and XPS, in: D. Briggs, M.P. Seah (Eds.), Practical Surface Analysis by Auger and X-Ray Photo- Electron Spectroscopy, 2nd ed., John Wiley & Sons Ltd., Chichester, 1990.

37. X-Ray Photoelectron Spectroscopy (XPS), https://www.ifw-dresden.de/de/institute/institut-fuer-komplexe -materialien/abteilungen/mikro-und-nanostrukturen/available-methods/xps/ (accessed March 27, 2016).

38. A.B. Christie, X-ray photoelectron spectroscopy, in: J.M. Walls (Ed.), Methods of Surface Analysis, Cambridge University Press, Cambridge,

1989.

39. Y. V. Butenko, S. Krishnamurthy, A.K. Chakraborty, V.L. Kuznetsov, V.R. Dhanak, M.R.C. Hunt, et al., Photoemission study of onionlike carbons produced by annealing nanodiamonds, Physical Review B. 71 (2005) 075420.

40. M. Hsiao, S. Liao, M. Yen, C. Teng, S. Lee, N. Pu, et al., Preparation and properties of a graphene reinforced nanocomposite conducting plate, Journal of Materials Chemistry. 20 (2010) 8496.

41. S. Ogawa, T. Yamada, S. Ishidzuka, A. Yoshigoe, M. Hasegawa, Y. Teraoka, et al., Graphene Growth and Carbon Diffusion Process during Vacuum Heating on Cu (111)/ Al_2O_3 Substrates, Japanese Journal of Applied Physics. 52 (2013) 110122.

42. B.G. Streetman, S. Banerjee, Solid State Electronic Devices, 5th ed., Prentice Hall, New Jersey, 2000.

43. Y. Liu, W. Li, M. Qi, X. Li, Y. Zhou, Z. Ren, Study on temperature-dependent carrier transport for bilayer graphene, Physica E: Low-Dimensional Systems and Nanostructures. 69 (2015) 115-120.

44. W. Zhu, V. Perebeinos, M. Freitag, P. Avouris, Carrier scattering, mobilities, and electrostatic potential in monolayer, bilayer, and trilayer graphene, Physical Review B. 80 (2009) 235402.

45. C. Cobaleda, E. Diez, M. Amado, S. Pezzini, F. Rossella, V. Bellani, et al., Quantum Hall effect in monolayer, bilayer and trilayer graphene, Journal of Physics: Conference Series. 456 (2013) 012006.

Chapter 4

Experimental procedure

4.1 Introduction

This chapter presents the experimental procedures and techniques used for the synthesis and characterizations of as-synthesized materials. The first part of this chapter focuses on the synthesis of C-Fe/PANI and VS_2 nanosheets, including the characterization techniques used for structural, morphological and electrochemical analysis of the as-synthesized materials. The last part of this chapter focuses on the fabrication of electrodes for three-electrode and two-electrode setup.

4.2 Materials

All the reagents used in this work are of analytical grade and were used as received without further purification. Chemicals used for VS_2 nanosheets and C-Fe/PANI synthesis were purchased from Sigma Aldrich (see table 4.1). A 3D

scaffold template of polycrystalline Ni foam with an areal density of 420 g m^2 and thickness of 1.6 mm was used as a current collector, and was purchased from Alantum (Munich, Germany).

C-Fe/PANI	**VS_2**
Aniline hydrochloride ($C_6H_5NH_2$·HCl, purity ≥99%)	Sodium orthovanadate (1 mM Na_3VO_4, purity 99.98%)
Ammonium persulphate ($(NH_4)_2S_2O_8$, purity ≥99%)	Thioacetamide (5 mM C_2H_5NS, purity ≥99%)
Iron nitrate nonahydrate ($Fe(NO_3)_3$·$9H_2O$, purity ≥99%)	–

Table 4.1: Chemicals used for the synthesis of C-Fe/PANI and VS_2 nanosheets purchased from Sigma Aldrich.

4.3 Synthesis of C-Fe/PANI

The PANI used for the synthesis of C-Fe/PANI was prepared as follows: 0.2 M aniline hydrochloride was added to a 50 ml solution of 1.0 M HCl, and in a separate beaker 0.25 M solution of ammonium persulphate was added to 1.0 M HCl. The prepared solutions were kept at room temperature for 1 h, thereafter, they were mixed and stirred for about an hour and left to polymerize. After polymerization, PANI precipitate was collected on a filter (after been washed several times with 100 ml of 0.2 M HCl, and acetone) and dried at 60 ℃ overnight. Furthermore, PANI was used as a substrate for adsorbing carbonized Fe cations. Briefly, 0.2 g of $Fe(NO_3)_3$·$9H_2O$ and 0.0125 g of PANI were dissolved in 50 mL of ethanol and sonicated in ultra-sonication bath until the ethanol was almost completely evaporated.

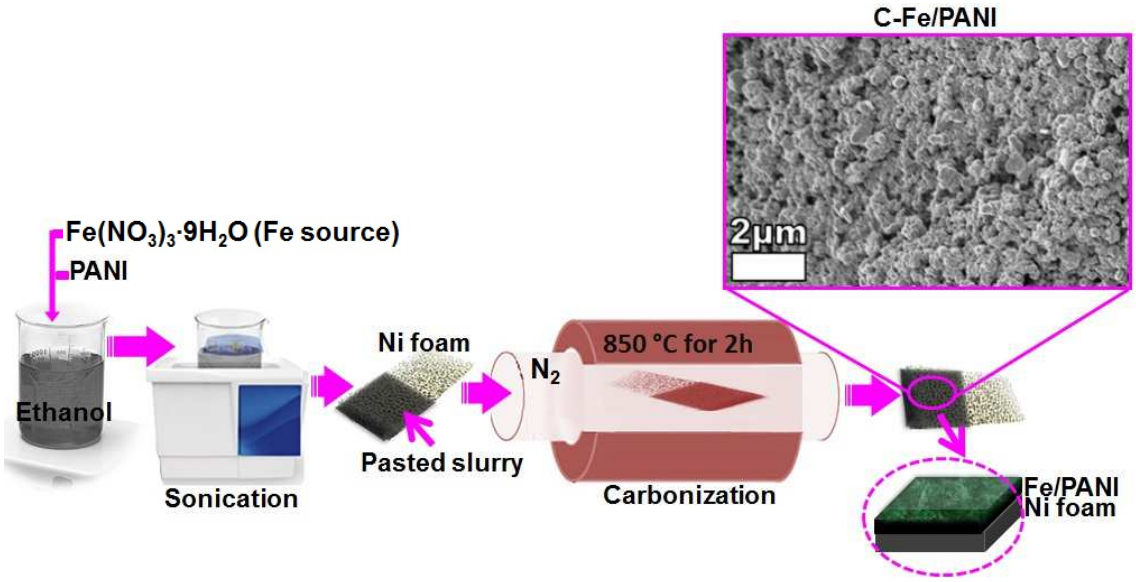

Figure 4.1: Schematic illustration of the synthesis route for C-Fe/PANI.

Thereafter, the slurry was coated on nickel foam (current collector) which was loaded in a tube furnace and heated to 850 ℃ and pyrolyzed for 2 h under the N_2 atmosphere (Figure 4.1). After pyrolysis, the as-synthesized sample which shows homogeneously dispersed nanograin particles (see micrograph in figure 4.1) was used as the negative and positive electrodes in symmetric and asymmetric supercapacitor devices.

4.4 Synthesis of VS_2 nanosheets

VS_2 nanosheets were synthesized by the hydrothermal method as shown in figure 4.2. In figure 4.2, 1.65 g of 1 mM Na_3VO_4 and 3.37 g of 5 mM C_2H_5NS were dissolved in 120 mL of deionized water and stirred for 1 h at room temperature using a magnetic stirrer. After stirring, the resultant solution was transferred into a sealed, 150 mL Teflon-lined, stainless-steel autoclave

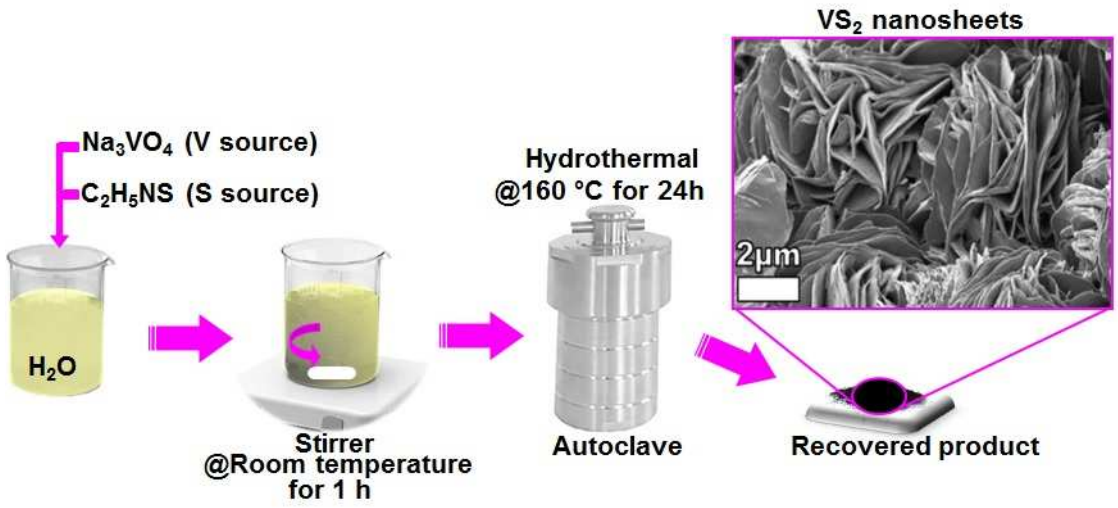

Figure 4.2: Schematic illustration of the synthesis route for VS_2 nanosheets.

and kept at a temperature of 160 ℃ for 24 h and then cooled naturally down to the room temperature. Subsequently, the obtained precipitate was filtered and washed with deionized water several times and dried at 60 ℃ overnight. Finally, the recovered product of VS_2 nanosheets was obtained as displayed by micrograph in figure 4.2.

4.5 Structural, and morphological characterization

The characterization techniques used in this work are listed in table 4.2, including the systems settings. The results obtained from these characterization techniques are presented in chapter 5 and 6.

Apparatus	Systems settings
XRD: XPERTPRO diffractometer (PANalytical BV, Netherlands)	▷ X-ray source: cobalt (Co) Kα (λ = 0.17890 nm) ▷ Generator operation: 50 kV and 30 mA ▷ Measurement settings: $2\theta = 10 - 90^{\circ}$, step size = 0.017° and time per step = 15 s
Raman spectrometer: T64000 micro-Raman spectrometer (HORIBA Scientific, Jobin Yvon Technology) WITec alpha300R confocal Raman microscope	▷ Laser wavelength: 514 nm ▷ Laser power: 3.0 mW ▷ Spectral acquisition time: 120 s ▷ Objective: 100x/0.9 ▷ Laser wavelength: 532 nm ▷ Laser power: 4.0 mW ▷ Spectral acquisition time: 10 s ▷ Objective: 100x/0.9
FTIR spectrometer: Perkin Elmer Spectrum RXI system	▷ Range: 400 to 4000 cm^{-1} ▷ Samples analyzed as KBr pellets
SEM: Zeiss Ultra Plus 55 field emission scanning electron microscope equipped with EDS	▷ Voltage: 2.0 kV
TEM: Jeol JEM-2100F Field Emission Electron Microscope	▷ Voltage: 200.0 kV
XPS: Physical Electronics VersaProbe 5000 spectrometer	▷ Beam voltage: 10 kV

Table 4.2: Characterization techniques (apparatus and systems settings).

4.6 Electrochemical characterization

All electrochemical analysis were carried out on a Biologic VMP-300 potentiostat (Knoxville TN 37,930, USA) controlled by the EC-Lab V10.37 software at room temperature. In the three-electrode system, a glassy carbon

plate was used as the counter electrode and Ag/AgCl (3 M KCl) electrode served as the reference electrode. The electrochemical performance of the electrodes was evaluated in both three and two electrode setup using the settings listed in table 4.3.

Experiments	**Settings**
Cyclic voltammetry	▷ Scan rates: 5 to 100 mV s^{-1} ▷ Voltage range: $0.0-0.5$ V and $-1.2-0.0$ V vs. Ag/AgCl (three-electrode); $0.0-1.7$ V (two-electrode)
Galvanostatic charge/discharge	▷ Current density: $0.2-10$ A g^{-1} ▷ Voltage range: $0.0-0.5$ and $-1.2-0.0$ V vs. Ag/AgCl (three-electrode); $0.0-1.7$ V (two-electrode)
Electrochemical impedance spectroscopy	▷ Frequency: 10 mHz−100 kHz (Open circuit potential)

Table 4.3: Electrochemical analysis settings for three and two electrode setup.

4.7 Preparation of the working electrodes

The working electrode of VS_2 nanosheets was prepared by coating a mixture of 80 wt% active material, 10 wt% carbon black and 10 wt% polyvinylidene fluoride (PVDF) binder dispersed in N-methylpyrrolidone (NMP) solution onto a piece of nickel foam ($1 \times 1 cm^2$), as illustrated in figure 4.3. The slurry was coated on both sides of the current collector for three-electrode and on one side for two-electrode measurements. After pasting, the electrode was dried at 60 ℃ overnight, and thereafter, the coated active material was pressed onto

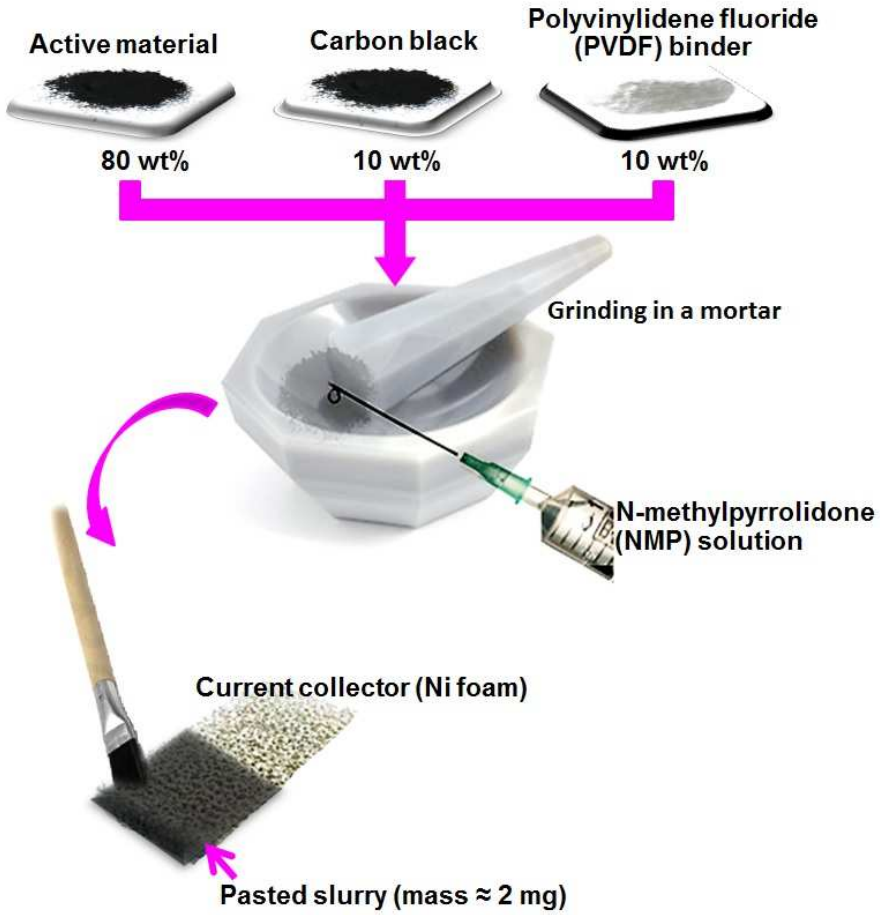

Figure 4.3: Process scheme for electrode preparation by coating a mixture of active material, carbon black and PVDF binder dispersed in NMP solution onto a piece of nickel foam.

the nickel foam under a pressure of 30 MPa.

The C-Fe/PANI working electrode was prepared as discussed in the synthesis method (see figure 4.2). Similar to preparation of VS_2 electrode, the slurry was coated on both sides of the current collector for three-electrode and on one side for two-electrode measurements.

The masses of the working electrodes (both positive and negative) ranged between 2 and 5 mg. The electrochemical measurements of VS_2 and

C-Fe/PANI electrodes were carried out in the three-electrode system in 6 M KOH, 1 M Li_2SO_4 and 1 M Na_2SO_4 electrolyte solution.

4.8 Fabrication of the supercapacitor device

The supercapacitor devices were fabricated based on VS_2 nanosheets as a cathode and C-Fe/PANI as an anode (asymmetric supercapacitor) and C-Fe/PANI electrode as both positive and negative electrode (symmetric supercapacitor) using 6 M KOH electrolyte, as illustrated in figure 4.4. Due to the difference in the specific capacity of the electrode in positive and negative potential window, a charge balance, $Q_+ = Q_-$ was done (see equation 2.4 in chapter 2). Based on this, the mass balance between the electrode in positive and negative potential window was achieved and for VS_2//C-Fe/PANI asymmetric supercapacitor the mass ratio is $m_+/m_- \approx 4$, and for C-Fe/PANI//C-Fe/PANI symmetric supercapacitor the mass ratio is $m_+/m_- \approx 1$. The electrochemical performance of the fabricated supercapacitor devices was evaluated using the settings listed in table 4.3.

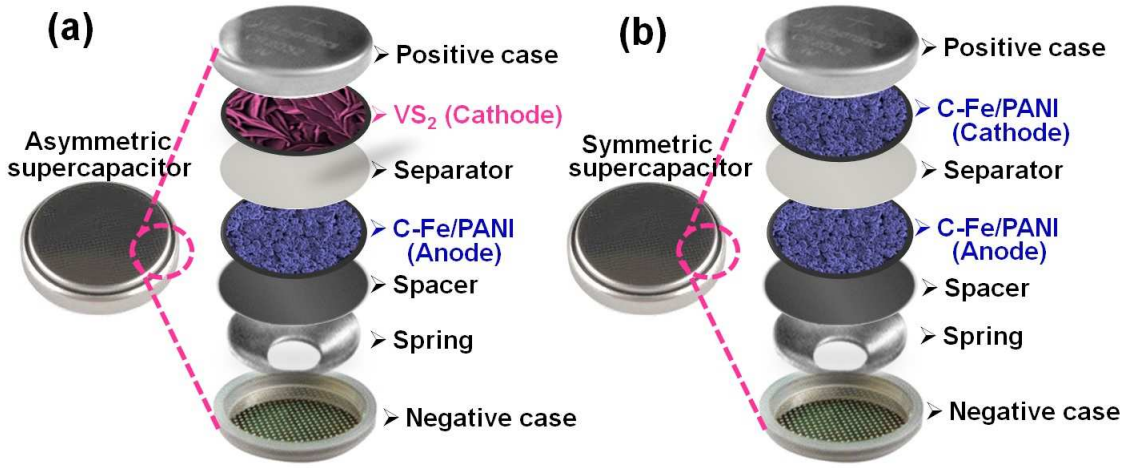

Figure 4.4: Schematic illustration of the assembled structure of supercapacitor devices based on (a) VS_2 nanosheets as a cathode and C-Fe/PANI as an anode (asymmetric supercapacitor) and (b) C-Fe/PANI electrode as both positive and negative electrode (symmetric supercapacitor) using 6 M KOH electrolyte.

PART IV

RESULTS, DISCUSSION AND CONCLUSION

Chapter 5

Symmetric supercapacitor with supercapattery behavior based on carbonized iron cations adsorbed onto polyaniline

5.1 Introduction

This chapter presents experimental findings on the structural and morphological characterization of the as-synthesized C-Fe/PANI electrode, including the electrochemical properties of the fabricated C-Fe/PANI symmetric device.

5.2 Results and discussion

The structural, morphological and compositional characterization of the as-synthesized electrode materials was carried out using different techniques such as X-ray diffraction (XRD) for crystal structure analysis, Raman

and Fourier transform infrared (FT-IR) spectroscopy for information on chemical structures and molecular interactions (vibrational modes), scanning electron microscopy (SEM) and transmission electron microscopy (TEM) for morphology, energy-dispersive X-ray spectrometer (EDS) for elemental composition of the sample and X-ray photoelectron spectroscopy (XPS) for the elemental composition and chemical state of the elements within a sample.

The electrochemical properties of the C-Fe/PANI electrode were evaluated in a three-electrode cell configuration in both positive and negative potential window using 6 M KOH electrolyte, and thereafter, a C-Fe/PANI symmetric device was successfully fabricated.

The results for structural, morphological and composition characterization are discussed in the attached publication below, including the electrochemical characterization.

5.3 Publication

Electrochimica Acta 262 (2018) 82–96

Contents lists available at ScienceDirect

Electrochimica Acta

journal homepage: www.elsevier.com/locate/electacta

Symmetric supercapacitor with supercapattery behavior based on carbonized iron cations adsorbed onto polyaniline

M.N. Rantho, M.J. Madito, N. Manyala*

Department of Physics, Institute of Applied Materials, SARChI Chair in Carbon Technology and Materials, University of Pretoria, 0028, South Africa

ARTICLE INFO

Article history:
Received 8 September 2017
Received in revised form
5 December 2017
Accepted 1 January 2018
Available online 2 January 2018

Keywords:
Supercapacitor
Supercapattery device
Iron-PANI
Negative electrode
Energy storage

ABSTRACT

The electrode material based on the carbonization of Fe cations adsorbed onto polyaniline (PANI) (C-Fe/PANI) was directly synthesized on nickel foam by pyrolysis of the iron-PANI mixture coated on nickel foam in a tube furnace under the N_2 atmosphere. The characterization of the as-synthesized electrode materials was carried out using X-ray diffraction (XRD), Raman spectroscopy, Fourier transform infrared (FT-IR) spectroscopy, scanning electron microscopy (SEM), high-resolution transmission electron microscopy (HR-TEM) equipped with a scanning transmission electron microscopy along with energy dispersive X-ray (STEM-EDX) and X-ray photoelectron spectroscopy (XPS). The electrochemical behavior of the working electrode was analyzed in both positive and negative potential window in a three-electrode cell configuration using 6 M KOH electrolyte, and thereafter, a C-Fe/PANI symmetric device was successfully fabricated. The C-Fe/PANI symmetric device was found to perform at a high applied potential difference of 1.65 V in 6 M KOH. At a current density of 0.5 A g^{-1}, this device exhibited energy and power densities of 41.3 W h kg^{-1} and 231.9 W kg^{-1} respectively. Additionally, the device exhibited a maximum power of 469.4 kW kg^{-1}. The device further showed excellent cycling stability with 100% Columbic efficiency and capacity retention of 72% at a current density of 5 A g^{-1} over 10 000 galvanostatic charge-discharge cycles.

1. Introduction

The development of high-performance energy storage devices is an important issues due to the great need for energy consumption in our modern daily lives [1–4]. Among various types of energy storage devices, supercapacitors (SCs) have attracted great attention for potential applications in electronic circuits, electric vehicles, and backup power generators [5]. This is due to the attractive properties of SCs such as portability, high efficiency, fast charge-discharge capability, long lifecycle stability, operational safety, and high power density [1]. The charge storage mechanism in SCs is divided into two classifications, namely, the electric double-layer capacitors (EDLCs) and pseudocapacitors [4,6,7]. In EDLCs, the electrochemical capacitors main energy storage is attained by double-layer capacitance, and in this charge storage process, there is no transfer of charges. Carbon-based materials with a high surface area are usually applied in SCs. In pseudocapacitors instead, the electrical energy is stored faradaically by electron charge transfer between electrode and electrolyte [4]. This is accomplished through electrosorption, reduction-oxidation reactions (redox reactions), and intercalation processes, called pseudocapacitance. The electrically conducting polymers and transition metal oxides/hydroxide/sulfides are normally used in pseudocapacitors [8–11].

Among various conducting polymers, that have been studied, polyaniline (PANI) has attracted great attention as one of the most promising pseudocapacitive material suitable for the next generation of SCs due to its high pseudocapacitance, lightweight, low cost, controllable electrical conductivity, high energy density, facile synthesis, and environmental friendliness [12–15]. However, PANI experience volume changes, i.e. the pseudocapacitive processes of PANI involve the swelling, shrinkage and cracking of the material during charging/discharging, which could result in cycling instability and poor rate performance [5,16,17]. It is shown in previous published reports that the electrochemical performance of PANI can be improved by use of PANI–carbon composites with carbon materials such as carbon nanotubes, nanofibers, graphene sheets and powdered activated carbon due to their high stability, good conductivity and high affordability [16–23]. Moreover, The need to

* Corresponding author.
E-mail address: ncholu.manyala@up.ac.za (N. Manyala).

https://doi.org/10.1016/j.electacta.2018.01.001
0013-4686/

develop high-performance supercapacitors has led to the incorporation of metals and metal oxide particles into PANI to enhance its electrical conductivity [24]. It has been shown that iron-containing nitrogen-doped graphitic carbon materials, PANI in particular, achieve high electrocatalytic performance and exhibit high stability [25,26]. These iron-containing nitrogen-doped PANI materials are synthesized by pyrolysis of a mixture of iron, carbon materials and PANI, in which the nitrogen-atoms originating from PANI coordinate Fe sites (Fe-PANI/carbon) [25,26]. Other than containing nitrogen, the preference of PANI is as result of its phenyl groups which easily produce a graphitic structure during pyrolysis, thus leading to enhanced electrical conductivity [26]. Although carbonized Fe-PANI/carbon studies have been reported in the literature for fuel cell applications [25,26], there are rare studies done on the carbonized Fe cations adsorbed onto PANI (C-Fe/PANI) as an electrode material directly synthesized on current collector for supercapacitor applications.

Herein, we report on a symmetric supercapacitor with supercapattery behavior based on C-Fe/PANI electrode material. This study focuses on structural, morphological and composition characterization of the as-synthesized electrode material, and the electrochemical properties of C-Fe/PANI symmetric device. The C-Fe/PANI symmetric device was found to perform at a high applied potential difference of 1.65 V in 6 M KOH. At a current density of 0.5 A g^{-1}, this device exhibited a maximum energy and power densities of 41.3 W h kg^{-1} and 231.9 W kg^{-1} respectively. In addition, the device showed excellent cycling stability with 100% Columbic efficiency and 72% capacity retention over 10 000 galvanostatic charge-discharge cycles at a current density of 5 A g^{-1}.

2. Experimental

2.1. Materials

All the reagents used in this work are of analytical grade and were used as received without further purification. Aniline hydrochloride ($C_6H_5NH_2$·HCl, purity ≥99%), ammonium persulphate ($(NH_4)_2S_2O_8$, purity ≥99%) and iron nitrate nonahydrate ($Fe(NO_3)_3$·$9H_2O$, purity ≥99.95%) were purchased from Sigma Aldrich. Polycrystalline Ni foam used as a current collector which is a 3D scaffold template with an areal density of 420 g m^2 and thickness of 1.6 mm was purchased from Alantum (Munich, Germany).

2.2. Synthesis of carbonized iron cations adsorbed onto polyaniline

For PANI synthesis: 0.2 M aniline hydrochloride was added to a 50 ml solution of 1.0 M HCl, and in a separate beaker 0.25 M solution of ammonium persulphate was added to 1.0 M HCl. The prepared solutions were kept at room temperature for 1 h, thereafter, they were mixed and stirred for about an hour and left to polymerize. After polymerization, PANI precipitate was collected on a filter (after been washed several times with 100 ml of 0.2 M HCl, and acetone) and dried at 60 °C overnight. Furthermore, a mixture of Fe and PANI was carbonized, in which the N-atoms originating from PANI can coordinate Fe sites (Scheme 1). Briefly, 0.2 g of $Fe(NO_3)_3$·$9H_2O$ and 0.0125 g of PANI were dissolved in 50 ml of ethanol and sonicated in the ultra-sonication bath until the ethanol was almost completely evaporated. Thereafter, the slurry was coated on nickel foam (current collector) which was loaded in a tube furnace and heated to 850 °C and pyrolyzed for 2 h under the N_2 atmosphere. After pyrolysis, the as-synthesized carbonized iron cations adsorbed onto polyaniline prepared directly on Ni foam (current collector, Scheme 1) without a binder were used as the negative and positive electrodes (symmetric supercapacitor) with masses of ~3 mg.

2.3. Structural, morphological and composition characterization

The crystallite structure analysis of the as-synthesized C-Fe/PANI material was carried out using X-ray diffraction (XRD) XPERTPRO diffractometer (PANalytical BV, Netherlands) with theta/2 theta geometry, operating with a cobalt (Co) tube at 50 kV and 30 mA. WITec alpha300R confocal Raman microscope with 532 nm excitation laser was used to characterize the as-synthesized electrode materials. Raman spectra were measured at room temperature with the laser power of 4 mW. Fourier transform infrared (FT-IR) spectroscopy performed in the range of 400–4000 cm^{-1} using Perkin Elmer Spectrum RX I FT-IR system was used to characterize the as-synthesized materials. The scanning electron microscopy (SEM) images of the samples were obtained using a Zeiss Ultra Plus 55 field emission scanning electron microscope

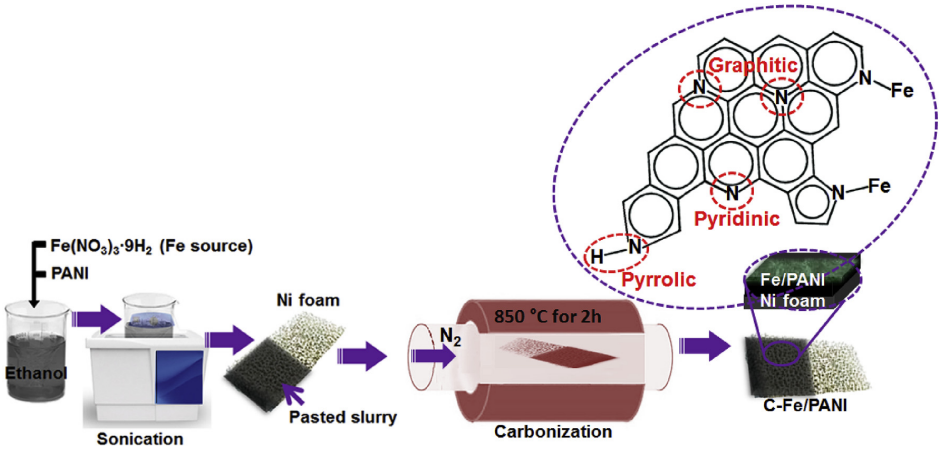

Scheme 1. Schematic illustration of the synthesis route for carbonized iron cations adsorbed onto polyaniline (C-Fe/PANI), and representation of PANI structure with the different possible N configurations (i.e. pyridinic N, pyrrolic N and graphitic N) some of which coordinate Fe sites.

(FE-SEM) operated at 2.0 kV. For transmission electron microscopy (TEM) analysis of the samples, the ethanol solution containing the sample was dispersed on a formal-coated copper grid and the analysis was carried out in a high-resolution transmission electron microscopy (HR-TEM) JEOL 2100 (from Tokyo Japan) equipped with LaB_6 filament, a Gartan U1000 camera of 2028 x 2028 pixels and operated at 200 kV. The HR-TEM is equipped with a scanning transmission electron microscopy along with energy dispersive X-ray (STEM-EDX) which were used for elemental distribution analysis and to estimate the elemental composition of the samples. X-ray photoelectron spectroscopy (XPS) measurements of the as-synthesized material were carried out using a Physical Electronics VersaProbe 5000 spectrometer.

2.4. Electrochemical characterization

All electrochemical analysis were carried out on a Biologic VMP-300 potentiostat (Knoxville TN 37,930, USA) controlled by the EC-Lab V10.37 software at room temperature. The working electrode (C-Fe/PANI) was prepared as discussed in the synthesis method (Scheme 1). Briefly, a mixture of PANI and Fe dissolved in ethanol was sonicated until the ethanol was almost completely evaporated, and thereafter, the slurry was coated on nickel foam (i.e. on both sides for three-electrode and on one side for two-electrode measurements) which was loaded in a tube furnace for pyrolysis. After pyrolysis, the as-synthesized C-Fe/PANI samples with a mass of about 3 mg (i.e. a mass of the active material) were used as the cathode and anode. The electrochemical measurements of C-Fe/PANI electrodes were carried out in the three-electrode system using 6 M KOH aqueous electrolyte solution. Cyclic voltammetry (CV) was performed at scan rates of 5–100 mV s^{-1} in the applied potential range of 0.0–0.45 V vs. Ag/AgCl and −1.2 to 0.0 V vs. Ag/AgCl for cathode and anode, respectively. The galvanostatic charge-discharge (GCD) curves for both working electrodes were tested. The electrochemical impedance spectroscopy (EIS) was measured in an open circuit potential over a frequency range of 10 mHz–100 kHz. The electrochemical analysis of the C-Fe/PANI electrode was also evaluated in a two-electrode symmetric device using 6 M KOH aqueous electrolyte solution. It is worth mentioning that the C-Fe/PANI electrode materials for both three-electrode and two-electrode electrochemical cells are the same and the current collector is Ni in both cells.

3. Results and discussion

3.1. Structural, morphological and composition characterization

Fig. 1(a) shows the XRD pattern of the as-synthesized C-Fe/PANI sample which displays very strong diffraction peaks of the Ni (current collector) which suppresses the weak diffraction peaks of the active material, i.e. carbonized Fe/PANI mixture. The strong diffraction peaks of the Ni substrate were avoided by preparing

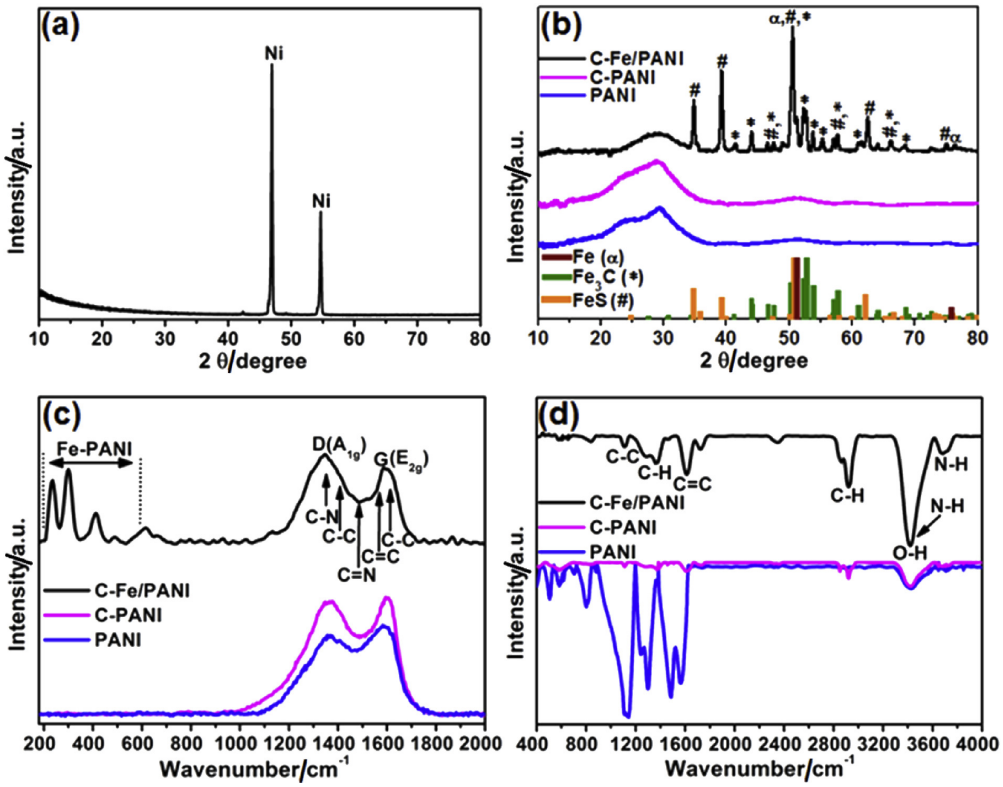

Fig. 1. The XRD pattern of the as-synthesized C-Fe/PANI: (a) with Ni foam (current collector) and (b) without Ni foam, and the matching ICSD cards for Fe, Fe_3C and FeS. The XRD pattern of the carbonized PANI (C-PANI) and pure PANI. (c) The Raman and (d) FTIR vibration spectra of the as-synthesized C-Fe/PANI, C-PANI and PANI.

C-Fe/PANI as a powder sample (i.e. without pasting on Ni foam) following the same procedure illustrated in Scheme 1, and Fig. 1(b) shows the XRD of the as-synthesized sample. The diffraction peaks of the as-synthesized C-Fe/PANI sample were indexed to an orthorhombic structure of Fe_3C with a space group of *P n m a* using the best matching Inorganic Crystal Structure Database (ICSD) card #16593 for Fe_3C, as shown in Fig. 1(b). However, some of the diffraction peaks of the C-Fe/PANI do not match with the Fe_3C standard, those were found to match the ICSD card no. 35 008 for FeS (crystal system: orthorhombic and space-group: *P n m a*) which suggests that during the pyrolysis process the degradation of ammonium persulphate from PANI synthesis generated iron sulfide. In addition to Fe_3C and FeS diffraction peaks, the diffraction peak at about 52° could also be due to metallic Fe, since during the pyrolysis process the Fe cations could be reduced to metallic iron by the reaction with pyrolytic carbon from PANI [27]. A broad diffraction peak at about 30° matches the PANI peak in comparison to pure PANI XRD, however, is it assigned to the XRD graphitic plane (002). In addition, the XRD pattern of the pure PANI and carbonized PANI (C-PANI) appear similar and show a broad diffraction peak at about 30°. The values of 2θ and *d*-spacing obtained from the XRD pattern of the as-synthesized C-Fe/PANI sample (Fig. 1(b)) and the matching data of Fe_3C, FeS and Fe from the crystal structure database are summarized in Table 1.

The chemical structure of the as-synthesized C-Fe/PANI was investigated using the Raman and FTIR vibration spectra, as shown in Fig. 1(c) and (d) respectively. Additionally, the Raman and FTIR vibration spectra of the C-Fe/PANI were compared to the vibration spectra of pure PANI and carbonized PANI (Fig. 1(c) and (d)). The Raman spectra in Fig. 1(c) show the D band (~1350 cm^{-1}) which is a breathing mode of sixfold rings (A_{1g} symmetry) and confirms the presence of the functional groups of PANI since it only appears in the presence of disorder in the carbon lattice sites. The Raman spectra also show the G band (~1602 cm^{-1}) which involves in-plane bond stretching displacements of sp^2 carbon atoms (E_{2g} symmetry) hence is common to all sp^2-hybridized carbonaceous materials [28]. In the range of 1240–1700 cm^{-1}, the vibration bands are attributable to PANI functional groups, as shown in Fig. 1(c) for C-Fe/PANI. Generally, the Raman spectrum of PANI reveals functional groups at approximately 1210 and 1346 cm^{-1} (C–N stretching), 1412 cm^{-1} (C–C stretching), 1490 cm^{-1} (C=N stretching), 1585 cm^{-1} (C=C stretching) and 1610 cm^{-1} (C–C stretching), [12,29]. Furthermore, the vibration bands in the range of 200–550 cm^{-1} originate from Fe–PANI vibration bands (e.g. Fe–C, Fe–N, Fe–S, etc.), and are similar to those reported by Pradhan et al. [30]. In view of the FTIR spectra in Fig. 1(d), the FTIR spectra clearly show that a pure PANI has high-intensity vibrational peaks in the range of 400–1800 cm^{-1} confirming a high content of functionalities in the material. However, these peaks are noticeably decreased by carbonization of the PANI (see the FTIR spectrum of C-PANI) suggesting that PANI is partially converted into a new carbon structure upon pyrolysis. Generally, the functional groups of PANI are observable at the IR bands of 1139 cm^{-1} (C–C stretching), 1296 cm^{-1} (C–H in-plane bending) and 1588 cm^{-1} (C=C stretching of the quinoid ring) [12]. In addition, the functional groups of PANI are also found at 2922 cm^{-1} (C–H stretching), 3420 and 3715 cm^{-1} (N–H stretching), however, the vibration band in the range of 3010–3680 cm^{-1} is usually assigned to O–H stretching vibrations [12,31–33]. No obvious characteristic peaks of iron–compounds vibrations at ~500 cm^{-1} are observed.

The morphology of the C-Fe/PANI sample was examined using SEM and the results are shown in Fig. 2(a) and (b). From these figures, it can be seen that the sample consist of agglomerated nanograins distributed all over the surface suggesting that Fe cations adsorbed onto PANI matrix are uniformly dispersed on the surface of the sample.

Fig. 3(a) and (b) show high-resolution TEM images of the as-synthesized PANI and C-Fe/PANI, respectively. From these figures, PANI does not show lattice fringes, as expected because is amorphous. In contrast to PANI, C-Fe/PANI shows obvious lattice fringes attributed to the Fe cations on PANI (Fig. 3(c) and (d)). In addition, Fig. 3(e) and (f) show the diffraction intensity profile of the lattice fringes area in Fig. 3(c) and (d), respectively. Fig. 3(e) displays the lattice fringe spacing of 0.298 nm corresponding to the (011) plane of FeS. The lattice fringe spacing of 0.201 nm in Fig. 3(f)

Table 1
The values of 2θ and *d*-spacing obtained from the XRD pattern of the as-synthesized C-Fe/PANI sample (Fig. 1(b)) and the matching 2θ values, including the *d*-spacing and the corresponding (*h k l*) planes obtained from the crystal structure database for Fe_3C, FeS and Fe.

Obtained data		Crystal structure database								
C-Fe/PANI		Fe_3C (#16593)			FeS (#35008)			Fe (#64795)		
2θ (°)	*d*-spacing (nm)	2θ (°)	*d*-spacing (nm)	*h k l*	2θ (°)	*d*-spacing (nm)	*h k l*	2θ (°)	*d*-spacing (nm)	*h k l*
29.72	0.349									
34.81	0.299				34.676	0.300	0 1 1			
39.16	0.267				39.175	0.267	1 1 1			
41.38	0.253	41.155	0.255	2 0 0						
43.99	0.239	43.992	0.239	1 2 1						
46.48	0.227	46.599	0.226	0 0 2						
47.49	0.222	47.569	0.222	2 0 1	47.302	0.223	2 1 0			
50.56	0.209	50.241	0.211	2 1 1	50.674	0.209	2 1 1			
51.16	0.207	51.293	0.207	1 0 2						
52.32	0.203	52.24	0.203	2 2 0				51.995	0.204	0 1 1
53.73	0.198	53.829	0.198	1 1 2						
55.29	0.193	56.871	0.188	0 2 2						
57.08	0.187				56.415	0.189	1 0 3			
57.65	0.186	57.715	0.185	2 2 1						
61.11	0.176	61.003	0.176	1 2 2						
62.38	0.173				62.153	0.173	0 1 3			
64.16	0.168	64.043	0.169	0 4 0						
66.21	0.164				66.553	0.163	3 0 2			
68.46	0.159	68.539	0.159	3 0 1						
72.63	0.151	72.575	0.151	2 2 2	73.173	0.150	0 0 4			
75.02	0.147				75.795	0.146	4 0 0			
76.37	0.145							76.617	0.144	0 0 2

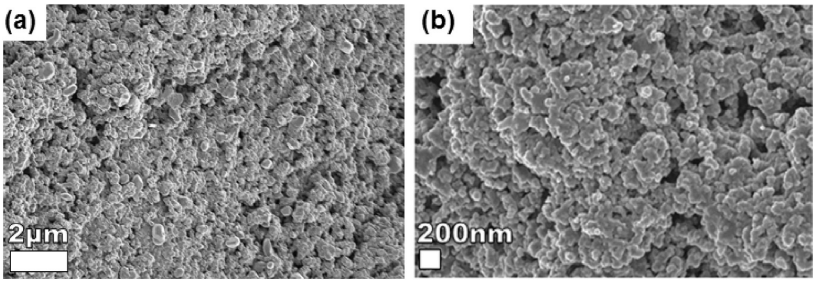

Fig. 2. (a) Low and (b) high magnification SEM images of the as-synthesized C-Fe/PANI.

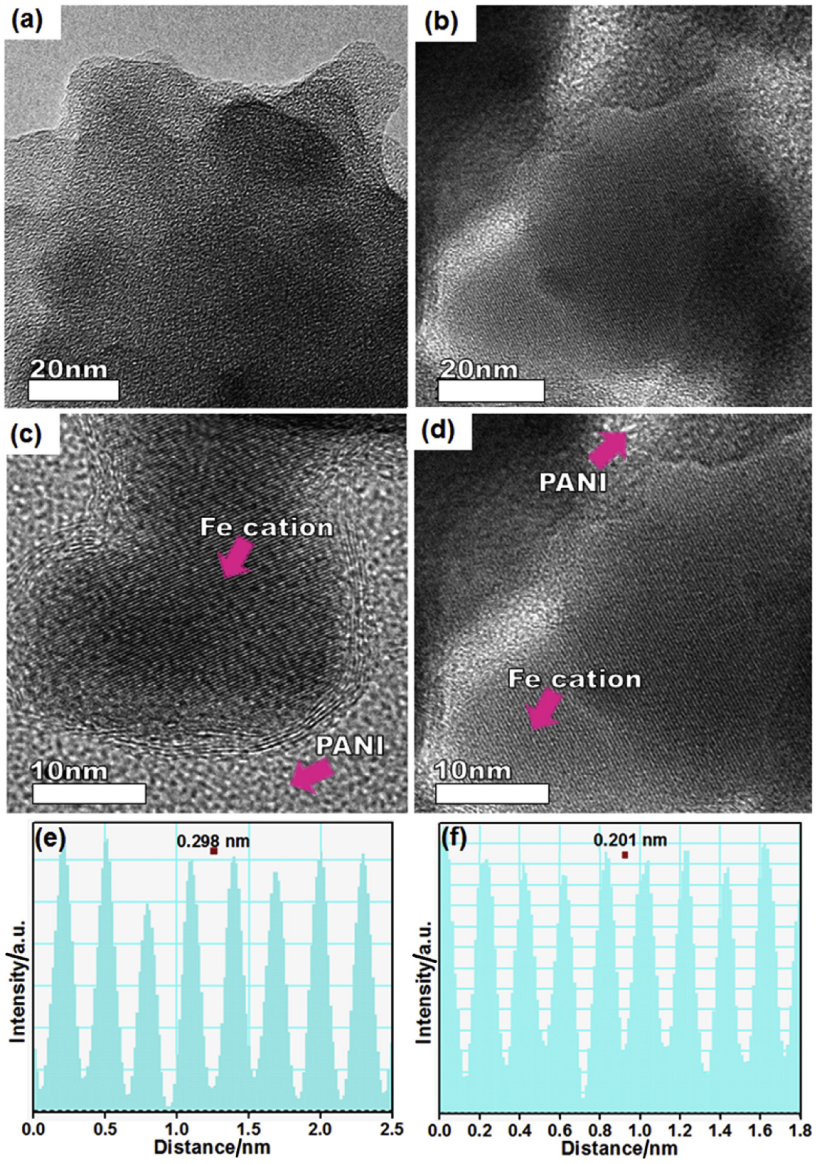

Fig. 3. (a) and (b) High-resolution TEM images of the as-synthesized PANI and C-Fe/PANI, respectively. (c) and (d) High-resolution TEM images of the as-synthesized C-Fe/PANI displaying lattice fringes attributed to the Fe cations on PANI. (e) and (f) The diffraction intensity profile of the lattice fringes area in (c) and (d), respectively.

corresponds to the (220) and (011) planes of Fe_3C and Fe, respectively (see Table 1).

To further evaluate the dispersion of Fe cations on the PANI structure, the elemental mapping was obtained for as-synthesized PANI and C-Fe/PANI using a scanning transmission electron microscopy along with energy dispersive X-ray and the maps are displayed in Figs. 4 and 5, respectively. Fig. 4(a) shows a scanning transmission electron microscopy image and Fig. 4(b)–(e) show the corresponding energy dispersive X-ray maps of C, N, O and S obtained from the as-synthesized PANI sample. Similarly, Fig. 5(a) shows a scanning transmission electron microscopy image and Fig. 5(b)–(f) show the corresponding energy dispersive X-ray maps of C, N, O, S and Fe obtained from the as-synthesized C-Fe/PANI sample. In Fig. 4, the detected elements, i.e. C, N and O are the main elements of the composition of PANI. In this sample, the detection of S only shows trace amount (0.01 wt%). In contrast to PANI, C-Fe/PANI sample shows a significant amount of S (6.4 wt%, see Table 2) attributed to the degradation of ammonium persulphate during the pyrolysis process. In addition, a significant amount of Fe aggregates is also observed confirming that Fe cations adsorbed onto PANI matrix are dispersed on the surface of the agglomerated nanograins distributed all over the surface of the C-Fe/PANI sample. The EDX elemental compositions for as-synthesized PANI and C-Fe/PANI samples are listed in Table 2.

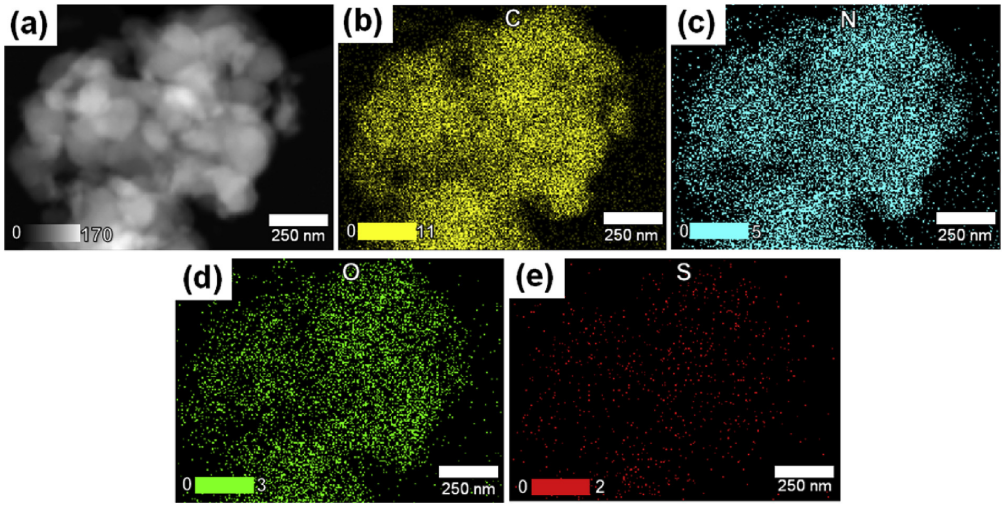

Fig. 4. (a) Scanning transmission electron microscopy image and (b)–(e) the corresponding energy dispersive X-ray maps of C, N, O and S obtained from the as-synthesized PANI sample.

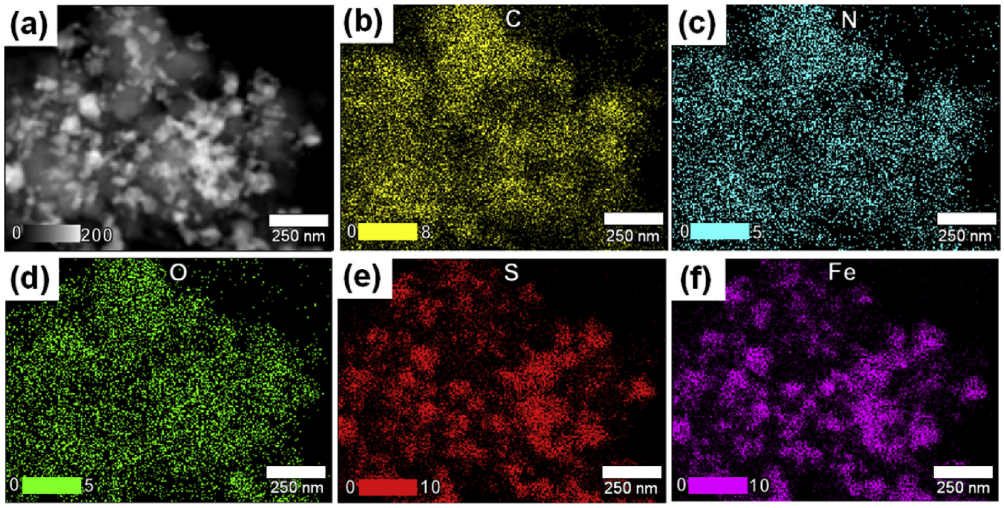

Fig. 5. (a) Scanning transmission electron microscopy image and (b)–(f) the corresponding energy dispersive X-ray maps of C, N, O, S and Fe obtained from the as-synthesized C-Fe/PANI sample.

Table 2
Summary of the EDX elemental compositions of as-synthesized C-Fe/PANI and PANI.

Sample	Element (Wt%)				
	C	N	O	S	Fe
C-Fe/PANI	51.1	8.2	4.1	6.4	30.2
PANI	81.03	10.16	8.80	0.01	–

The configuration of atoms (e.g. Fe, N, C and O) in the as-synthesized C-Fe/PANI sample was further analyzed by XPS. Fig. 6(a) shows the core level spectrum of Fe 2p of the as-synthesized C-Fe/PANI sample which reveals the binding energy peak at around 707 eV corresponding to Fe $2p_{3/2}$ core level photoelectrons. The fitted Fe $2p_{3/2}$ peak reveals Fe^{3+} (708.1 eV) and Fe^{2+} (706.5 eV) oxidation states present in the sample which could be mainly due to iron-carbide, iron-sulfide and iron-nitride configurations. On the other hand, the fitted peak at 706.5 eV (Fe^0) also indicates the presence of metallic Fe in the sample [34]. In Fig. 6(b), the core level spectrum of N 1s reveals different nitrogen configurations, i.e. pyridinic N at 398.6 eV, pyrrolic N at 400.2 eV (bound to a hydrogen atom) and graphitic N at 401.5 eV (includes ammonium species) present in the sample which are typically found in N-containing/doped carbon materials (e.g. PANI). A pyridinic N peak (398.6 eV) and N–Fe bound configuration peak (399.3 eV) occur at almost the same binding energy [35], hence pyridinic N peak may also consist of contribution from N–Fe. Fig. 6(c) shows the core level spectrum of C 1s which reveals different carbon components, namely, C=C at 284.5 eV (sp^2 carbon), C–C at 285.3 eV (sp^3 carbon), C–OH/C–N at 286.5 eV, C–O–C at 287.6 eV and C=O at 288.9 eV [36,37]. The high-intensity peak at 284.5 eV (C=C) confirms the predominance content of graphitic carbon in the sample. Additionally, the core level spectrum of O 1s (Fig. 6(d)) shows oxygen components at binding energies of 532.7 and 530.9 eV attributed to C–OH/C–O–C and C=O respectively [38].

3.2. Electrochemical characterization

To study the electrochemical performance of the material, the C-Fe/PANI electrodes were firstly evaluated in three-electrode configuration in both positive and negative potential window using three different electrolytes at a scan rate of 50 mV s^{-1}, as shown in Fig. 7(a). From the figure, it can be seen that 6 M KOH is the best electrolyte for both positive and negative potential window compared to 1 M Na_2SO_4 and 1 M Li_2SO_4 electrolytes, as it gives a high current response. The low current response in 1 M Na_2SO_4 and 1 M Li_2SO_4 electrolytes may be due to the ionic conductivity of Na^+ and Li^+ which are much lower than that of K^+. Consequently, the ionic conductivity of 1 M Na_2SO_4 and 1 M Li_2SO_4 electrolytes is much lower than that of 6 M KOH electrolyte, which is attributed to the high mobility of OH^- anions in water solutions. In fact, the OH^- anion has the highest ionic conductivity among anions [39]. A high concentration of 6 M KOH electrolyte also

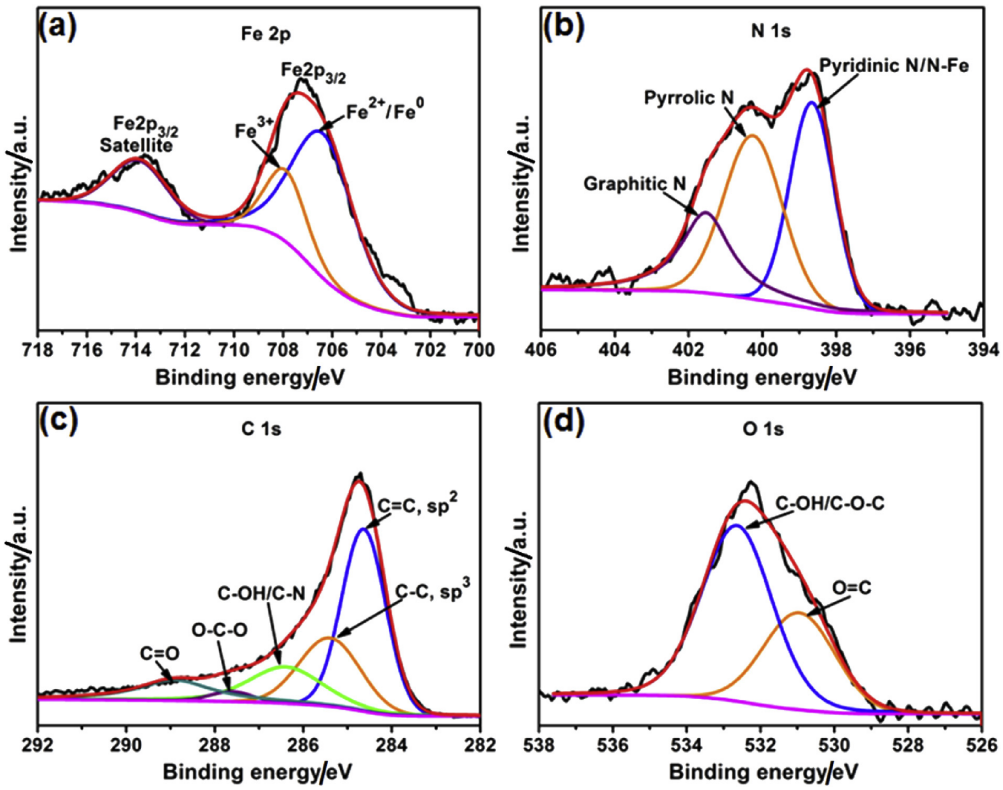

Fig. 6. (a) The XPS core level spectrum of (b) Fe 2p, (c) N 1s, (d) C 1s and (e) O 1s of the as-synthesized C-Fe/PANI sample.

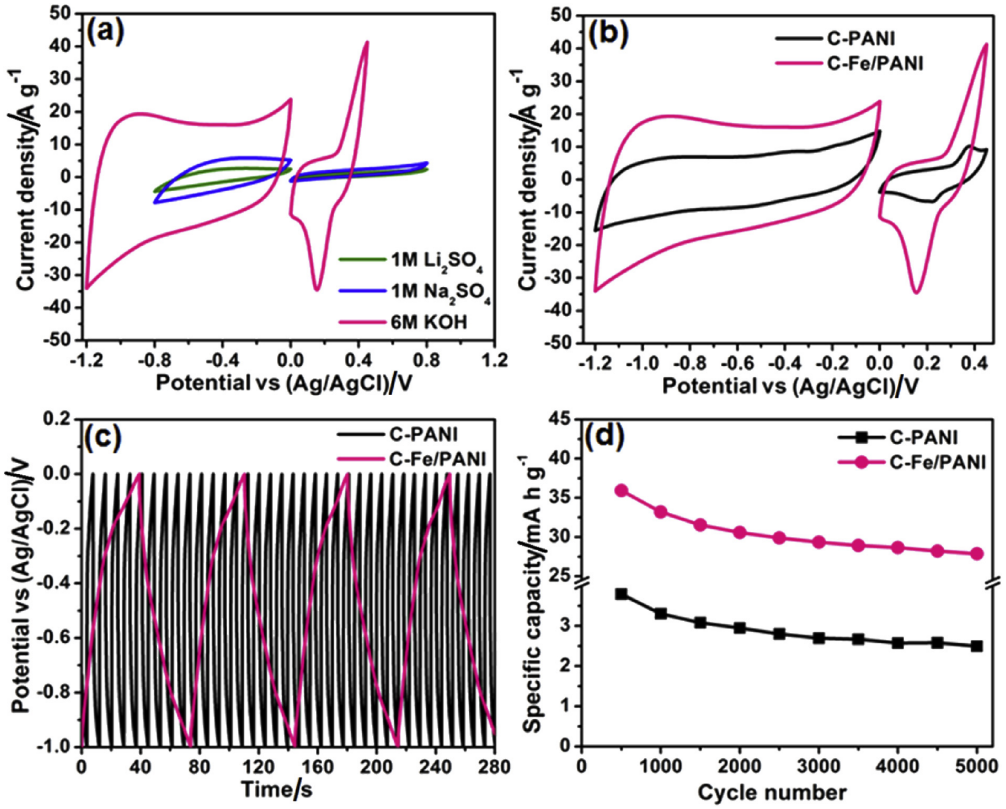

Fig. 7. (a) CV curves of C-Fe/PANI in different electrolytes at a scan rate of 50 mV s^{-1} in both positive and negative potential window. (b) CV curves of both C-PANI and C-Fe/PANI at a scan rate of 50 mV s^{-1} in 6 M KOH electrolyte. (c) GCD curves of both C-PANI and C-Fe/PANI at 1 A g^{-1}. (d) The specific capacity of both C-PANI and C-Fe/PANI and as a function of a cycle number at a current density of 5 A g^{-1}.

increases the number of ions hence the ionic conductivity of the electrolyte also increases. It is noticeable that in the negative potential window, carbonaceous part of the electrode (i.e. PANI) dominates displaying EDLC behavior, however, in the positive potential window, the faradic behavior dominates. Such behavior in the positive electrode is mainly influenced by the presence of functional groups in electrochemical activities and the additional contribution of pseudocapacitance of iron-composite layer. Fig. 7(b) shows the CV curves of both carbonized PANI and carbonized Fe/PANI mixture in both positive and negative potential window at a scan rate of 50 mV s^{-1} in 6 M KOH electrolyte. From Fig. 7(b) it is clear that C-Fe/PANI exhibits high current response compared to C-PANI. This clearly reveals that Fe cations enhance the electrical conductivity of C-Fe/PANI.

To further evaluate the cycling performance of the C-Fe/PANI in comparison to C-PANI, the electrodes were subjected to 5000 charge-discharge cycles at a current density of 5 A g^{-1} of which the few cycles for both electrodes are shown in Fig. 7(c). From the figure, it can be seen that C-PANI charge and discharge fast than C-Fe/PANI electrode which suggest that C-Fe/PANI electrode has a better charge storing capacity. From the acquired GCD curves the specific capacity (Q_S) for both C-PANI and C-Fe/PANI electrode was calculated, and shown as a function of number of circles in Fig. 4(d), using the following equation [4,40–43]:

$$Q_S = \left(\frac{I}{m}\right)\frac{t}{3.6} \quad (1)$$

where I is the applied current (A), m is the total mass of the active material (g), and t is the time taken for a complete discharge cycle (s).

From Fig. 7(d), it can be seen that C-Fe/PANI has high specific capacity compared to C-PANI electrode and also exhibits excellent cycling stability with 78% capacity retention over 5000 GCD cycles compared to C-PANI with capacity retention of 66%. This is in agreement with studies that have shown that iron-containing PANI, achieve high electrocatalytic performance and exhibit high cycling stability [25,26]. In addition, the recent reports have shown that iron sulfides in conducting polymers improve cycling stability [44].

To further evaluate the C-Fe/PANI electrode in the three electrode configuration using 6 M KOH electrolyte, the CV curves of C-Fe/PANI electrode at different scan rates in the range of 5–100 mV s^{-1} in a negative potential window range of −1.2 to 0.0 V are shown in Fig. 8(a). In the figure, the CV curves show relatively rectangular shapes, which is a typical EDLC behavior. Also, in a negative potential window range of −1.2 to 0.0 V, the GCD curves of

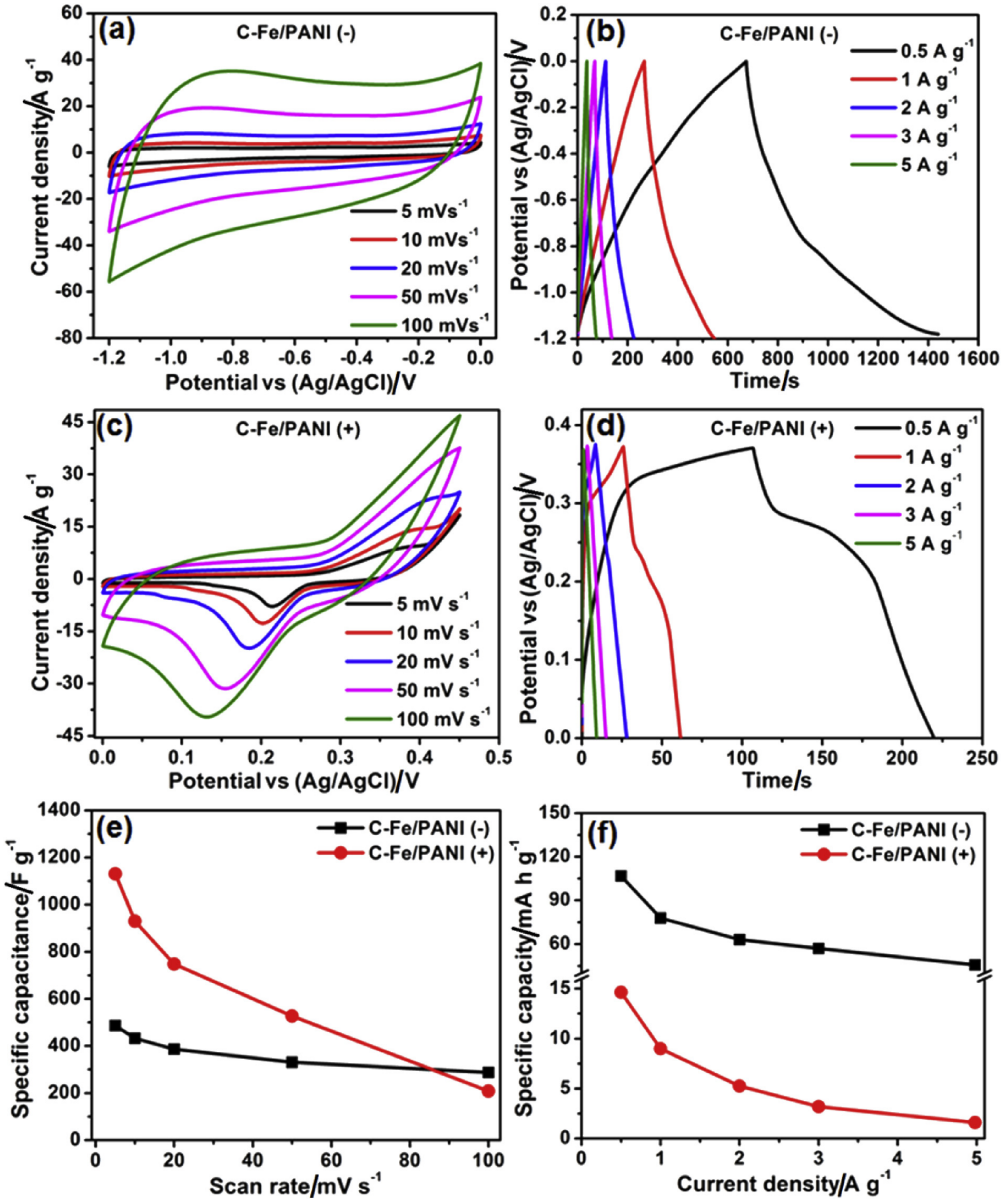

Fig. 8. (a) CV curves of C-Fe/PANI negative electrode at different scan rates in a potential window range of −1.2 to 0.0 V. (b) GCD curves of the C-Fe/PANI negative electrode at different current densities. (c) CV curves of C-Fe/PANI positive electrode at different scan rates in a potential window range of 0.0–0.45 V. (d) CD curves of the C-Fe/PANI positive electrode at different current densities. (e) Specific capacitance as a function of scan rate for C-Fe/PANI positive and negative electrode, respectively. (f) The specific capacity of both C-Fe/PANI positive and negative electrodes as a function of current density.

C-Fe/PANI electrode at various current densities in the range of 0.5–5 A g^{-1} are shown in Fig. 8(b). These GCD curves show almost linear behavior, thus, illustrating mostly EDLC behavior in agreement with the CV curves of the C-Fe/PANI electrode. Furthermore, the C-Fe/PANI electrode was evaluated in a positive potential window range of 0.0–0.45 V, and Fig. 8(c) shows the CV curves of the electrode at different scan rates ranging from 5 to 100 mV s^{-1}. These CV curves reveal the presence of a well-defined pair of redox peaks (cathodic at ~0.2 V and anodic at ~0.4 V) and the corresponding peaks shoulders (cathodic peak shoulder at ~0.3 V and anodic peak shoulder at ~0.2 V) which are due to the electrochemical redox reactions arising from the presence of functional groups which have high redox reactivity characteristics in the positive potential window. Additionally, the cathodic peak can also

be attributed to the reversible conversion between Fe(II/III) redox couple and on the other hand, the anodic peak can be attributed to the oxidations: $Fe_3C \rightarrow Fe^{3+}$ and $Fe \rightarrow Fe^{2+}$. FeS is reported to behave much less reversibly [45]. Consequently, the high current response observed in the positive potential window is attributed to synergistic electrochemical effect/reaction caused by PANI and Fe. The GCD curves of C-Fe/PANI electrode are shown in Fig. 8(d) at current densities ranging from 0.5 to 5.0 A g^{-1}. These curves show potential steps, i.e. a fast potential drop (~0.4–0.25 V) and slow potential drop (~0.25–0.15 V) which confirms the faradic behavior of the C-Fe/PANI electrode in the positive potential window in agreement with the CV curves. Moreover, the specific capacitance (C_S) of C-Fe/PANI was calculated as a function of scan rate from the CV curves integrals for both positive and negative potential windows as shown in Fig. 8(e), using the following equation:

$$C_S = \frac{\int I(V)dV}{m\nu\Delta V} \quad (2)$$

where m is the total mass of the active material (g), ν is the scan rate (V s^{-1}), $\Delta V = V_f - V_i$, and V_f and V_i are the integration potential limits of the CV curve (V), and I (V) is the CV current (A).

From Fig. 8(e) it can be seen that at a scan rate of 5 mV s^{-1}, C-Fe/PANI electrode exhibits a high specific capacitance of 1130.8 F g^{-1} in the positive potential window compared to negative potential window in which it exhibits a specific capacitance of 486.5 F g^{-1}. Additionally, the specific capacity of the electrode in both positive and negative potential window was calculated as a function of current density from the GCD curves using Equation (1), as shown in Fig. 8(f). From Fig. 8(f) it is clear that C-Fe/PANI exhibits higher specific capacity of 106.7 mA h g^{-1} in the negative potential window compared to 14.6 mA h g^{-1} exhibited in the positive potential window at a current density of 0.5 A g^{-1}. It is clear that the specific capacity of the working electrode continuously decreases with increasing current density in both potential windows. Generally, this may be due to the increasing electronic field within the cell setup, increased by increase in current density which alters both faradic and EDLC processes. In addition, the observed decrease in the specific capacity can also be attributed to the ion exchange mechanism where at low current density, a high specific capacity is obtained because the K^+ in the negative and OH^- in the positive potential window has enough time to be intercalated/extracted into/out of the electrode during charging/discharging [46]. However, at high current density, a low specific capacity is obtained because less charge is transferred between electrolyte and the electrode.

In order to fully explore electrochemical performance of C-Fe/PANI electrode as both positive and negative electrode, a symmetric supercapacitor device (scheme in Fig. 9(a)) with a supercapattery behavior was fabricated using 6 M KOH electrolyte. In addition, due to the difference in the specific capacity of the electrode in positive and negative potential window, a charge balance, $Q_+ = Q_-$ was done, where Q_+ and Q_- are charge stored in the electrode in both positive and negative potential window respectively. The charge balance is necessary in order to acquire the optimal performance of the device. Based on the charge definition, $Q = C_S m\Delta V$, the mass balance between the electrode in positive and negative potential window was achieved ($m_+/m_- \approx 1$) using the following expression [40]:

$$\frac{m_+}{m_-} = \frac{C_{S(-)} \times V_-}{C_{S(+)} \times V_+} \quad (3)$$

where $C_{S(+)}$ (= 1130.8 F g^{-1} at a scan rate of 5 mV s^{-1}) and $C_{S(-)}$ (= 486.5 F g^{-1} at a scan rate of 5 mV s^{-1}) are the specific capacitance of the active material of the electrodes in positive and negative potential window respectively, m_+ and m_- are the masses of the active material of the electrodes in positive and negative potential window, and V_+ (= 0.45 V) and V_- (= 1.2 V) are the positive and negative potential windows of the working electrodes respectively.

After the mass balance ratio ($m_+/m_- \approx 1$) was obtained, the as-synthesized positive and negative electrode with similar masses (m_+ = 2.6 mg and m_- = 2.4 mg) were used for device fabrication. Fig. 9(b) shows the CV curves of C-Fe/PANI electrode in the positive and negative potential window evaluated in three-electrode measurements at a scan rate of 50 mV s^{-1}. Since the C-Fe/PANI electrode has a potential window range of −1.2 to 0.0 V and 0.0–0.45 V in the negative and positive potential window respectively, the CV curves of the C-Fe/PANI symmetric cell was able to reach potential window in the range of 0.0–1.65 V, as shown in Figs. 9(c) and 6(d). Fig. 9(c) shows the CV curves of the device in the potential window of 0.0–1.2 and 0.0–1.65 V both at a scan rate of 50 mV s^{-1}. The figure clearly illustrates the EDLC and faradic behavior of the device. It can be seen that the EDLC contribution has equivalent positive and negative currents, on the other hand, the faradic contribution shows much higher positive current compared to EDLC contribution suggesting that the contribution of the positive electrode to the total current of the device dominates hence the device has mostly faradic behavior. Fig. 9(d) shows the CV curves of the device at different scan rates in the range of 5–100 mV s^{-1}. It can be seen from the CV curves that a device has a combined contribution of EDLC and faradic behavior and such combined behavior was named “supercapattery” (supercapacitors-batteries: from combined characteristics of pseudocapacitor behavior for negative electrode and battery-like behavior for positive electrode) [47,48]. In addition, Fig. 9(e) show the GCD curves at different current densities in the range of 0.5–5 A g^{-1} which shows the potential steps confirming the faradic behavior of the device in agreement with CV curves (Fig. 9(d)).

In addition, the energy density, E_d (W h kg^{-1}) and power density, P_d (W kg^{-1}) of the fabricated C-Fe/PANI symmetric supercapacitor device were calculated from the GCD curves at different current densities in the range of 0.5–5 A g^{-1} (Fig. 9(e)) using the following expressions:

$$E_d = \left(\frac{I}{m}\right)\frac{\int V(t)dt}{3.6} \quad (4)$$

$$P_d = \frac{3.6E_d}{\Delta t} \quad (5)$$

where I is the applied current (A), m is the total mass of the active material (g), $\int V(t)dt$ is the integral under the discharge curve from GCD curve of the device, and Δt is the discharge time (s).

At a current density of 0.5 A g^{-1}, the device exhibited energy and power densities of 41.3 W h kg^{-1} and 231.9 W kg^{-1} respectively. Fig. 10(a) shows the Ragone plot of the device which describes the relationship between energy density and power density, including the energy and power density regions for lithium ion batteries (faradic behavior) and electrochemical capacitors (EDLC behavior). The Ragone plot clearly shows that the power densities for C-Fe/PANI symmetric supercapacitor device are within the upper end of the electrochemical capacitors' region confirming the supercapacitor characteristics the device and the energy densities for the device extend to the upper end of lithium Ion batteries' region confirming a battery-like behavior of the device at low current densities. Therefore, based on the power and energy density

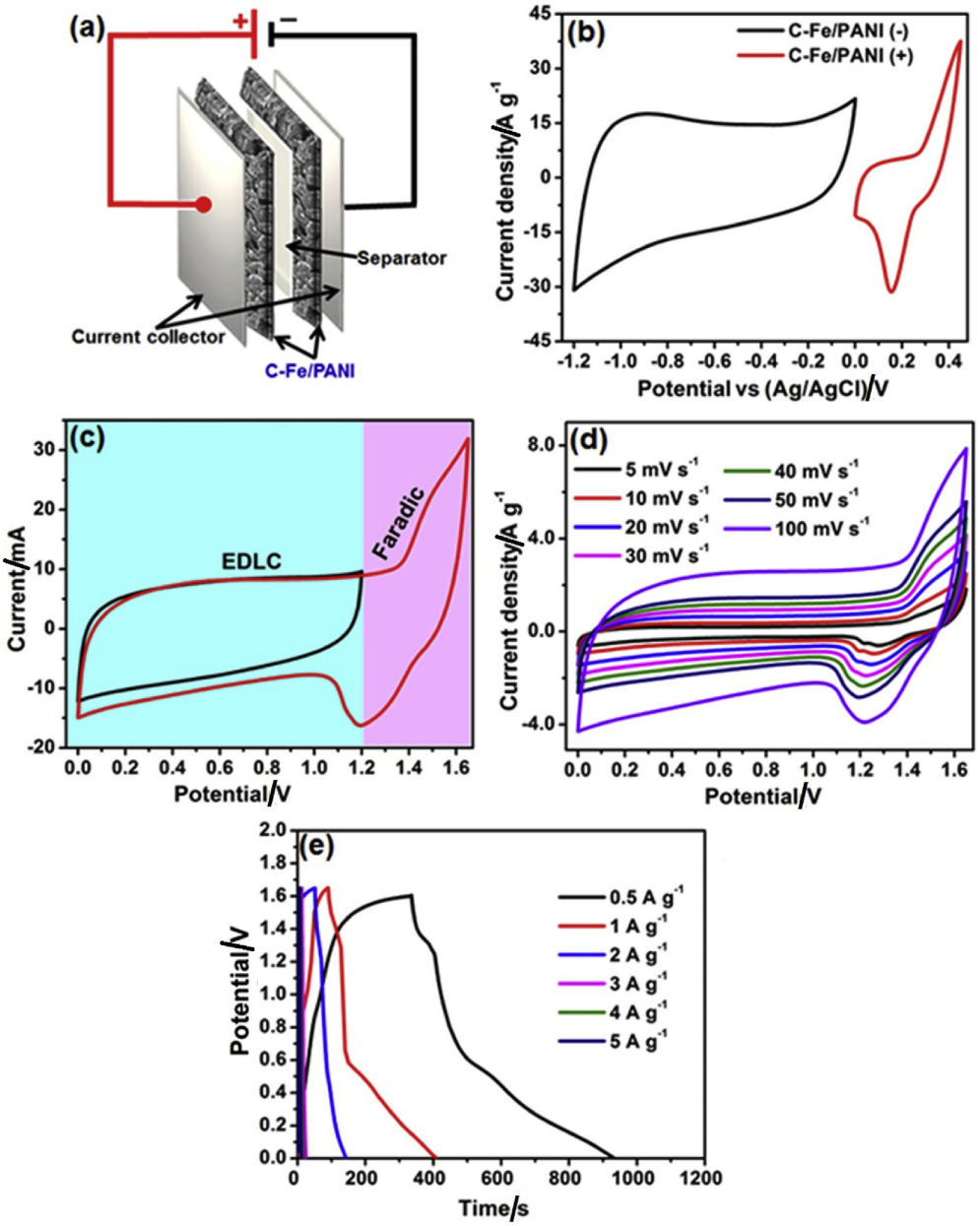

Fig. 9. (a) Schematic illustration of the fabricated C-Fe/PANI symmetric supercapacitor using 6 M KOH aqueous electrolyte. (b) CV curves of C-Fe/PANI electrode in the positive and negative potential window evaluated in three-electrode measurements at a scan rate of 50 mV s^{-1} (c) CV curves of the device in the potential window of 0.0–1.2 and 0.0–1.65 V both at a scan rate of 50 mV s^{-1} (illustrates the EDLC and faradic behavior of the device). (d) CV curves of the device at different scan rates in the range of 5–100 mV s^{-1} (e) GCD curves of the device at different current densities in the range of 0.5–5 A g^{-1}.

(combined supercapacitor-battery characteristics), it is suggested that the C-Fe/PANI symmetric device could be classified as "supercapattery" type of electrochemical power sources. Furthermore, as shown in the Ragone plot, the power and energy densities obtained in this work are superior to those reported on PANI based symmetric devices [5,18,49]. Furthermore, the maximum power, P_{max} of the device obtained is 469.4 kW kg^{-1}. The following standard approach was used to calculate the maximum power at the

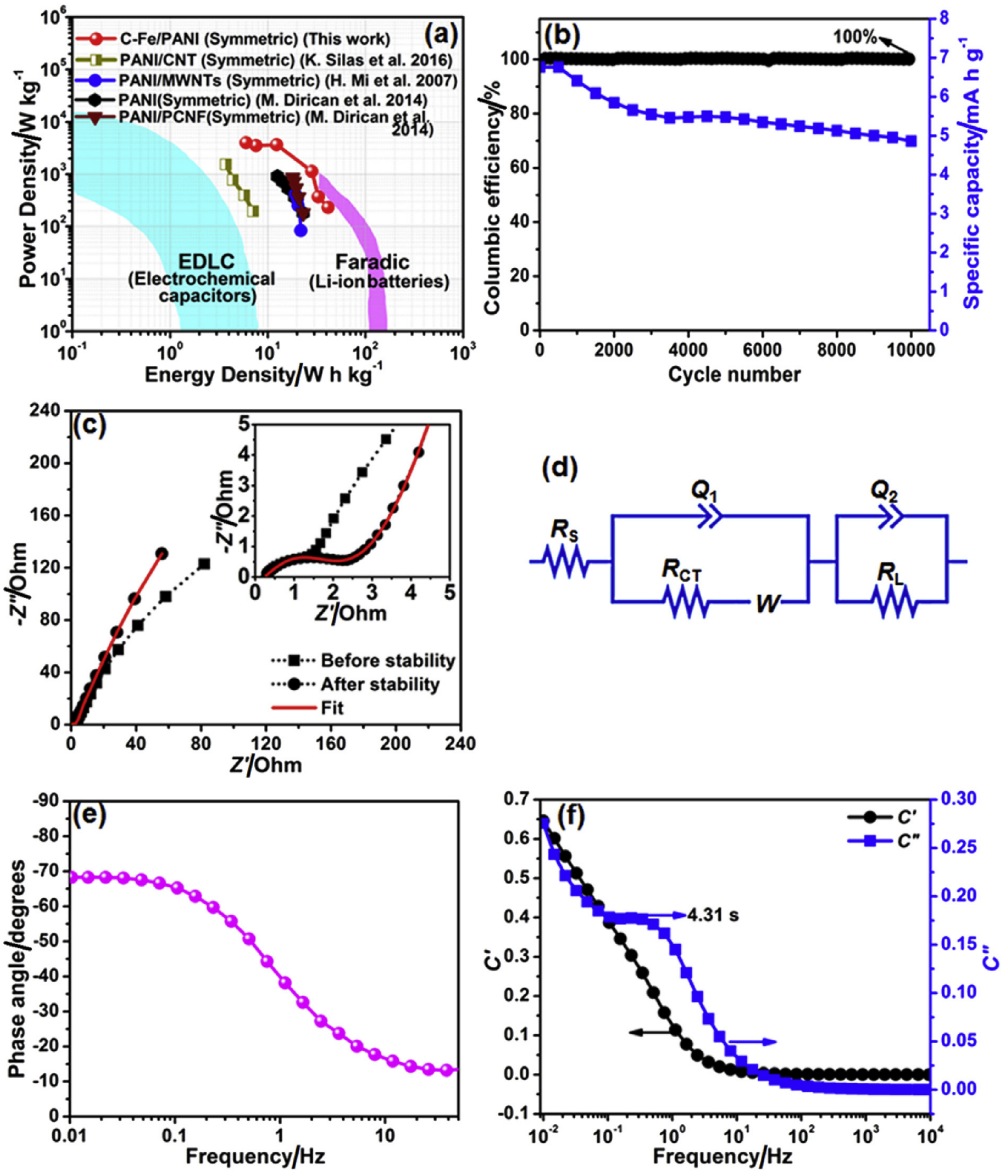

Fig. 10. (a) Ragone plot of the C-Fe/PANI symmetric device showing the relationship between energy and power densities, including the energy and power density regions for lithium ion batteries (faradic behavior) and electrochemical capacitors (EDLC behavior). (b) The columbic efficiency and the specific capacity retention as a function of a cycle number for the device at a current density of 5 A g^{-1}. (c) The Nyquist plots before and after cycling stability of the device (the inset shows the enlarged high-frequency region of the plots). (d) The equivalent circuit diagram used to fit the Nyquist plot after stability in (c) (i.e. a red solid-line). (e) The phase angle versus frequency. (f) Real and imaginary plot of capacitance as a function of frequency. (For interpretation of the references to colour in this figure legend, the reader is referred to the Web version of this article.)

matched impedance condition [1]:

$$P_{max} = \frac{V^2}{4mR_S} \quad (6)$$

where V is the maximum potential window of the device (= 1.65 V), m is the total mass of the active materials (= 5.0×10^{-6} kg), and R_S is the solution resistance (= 0.29 Ω) as determined from the Nyquist plots.

Fig. 10(b) shows the plots of columbic efficiency and specific capacity as a function of cycle number for the device performed at a current density of 5.0 A g^{-1}, which reveals an excellent cycling stability of the device with a columbic efficiency of 100% and 72% capacity retention of the initial capacity up to 10 000 cycling. The

electrochemical behavior of the device was further evaluated using the EIS, and the EIS of the C-Fe/PANI symmetric device before and after cycling stability was carried out (Fig. 10(c)). In Fig. 10(c), the Nyquist plots (imaginary component, Z'' versus the real component, Z' of the impedance) show semi-circle in the high-frequency region and in the low-frequency region the plots show a linear component (slightly tilted vertical line with superior angles than 45°) indicating a deviation from ideal capacitive behavior, and also the existence of a low diffusion resistance of ions within the electrode materials. The Nyquist plot after cycling stability shows a slight increase in the diameter of the semi-circle in the high-frequency region (see the inset to the figure) compared to the Nyquist plot before cycling stability, indicating some loss of conductivity and deterioration of the active material due to possible degradation reactions during cycling. This could be attributed to the adhesion loss of some electro-active material on the current collector during a cycle test. The electrodes before and after cycling stability display a similar and shorter diffusion length descriptive of the easiness of the movement of ions towards the electrode/electrolyte interface and the transfer of the charge to the electrodes. Moreover, the plot after stability was fitted (see a red solid-line in Fig. 10(c)) using the equivalent circuit diagram shown in Fig. 10(d). In the high-frequency region, the equivalent circuit diagram presents the equivalent series (solution) resistance, R_S in series with the charge transfer resistance, R_{CT}, and Warburg impedance characteristic element, W, which can be expressed as $W = A/(j\omega)^{1/2}$, where A is the Warburg coefficient, ω is the angular frequency parallel to the real capacitance (Q_1) [50]. The R_S and R_{CT} values represent the ohmic resistance of the electrodes and the charge-transfer kinetics (fast ion transport), respectively. In the low-frequency region, an ideal supercapacitor exhibits a vertical line parallel to the imaginary axis with a mass capacitance, Q_2, however, in practice supercapacitors show deviation from this ideal behavior which is attributed to a leakage resistance, R_L arising from the faradaic charge transfer process [51,52]. In the equivalent circuit, R_L is parallel to the Q_2. The R_S and R_{CT} values before stability ($R_S = 0.29\ \Omega$ and $R_{CT} = 1.51\ \Omega$) and after stability ($R_S = 0.29\ \Omega$ and $R_{CT} = 2.01\ \Omega$) are small and similar signifying good chemical stability of the electrodes.

Fig. 10(e) shows the impedance phase angle dependence on a frequency (Bode plot) for the C-Fe/PANI symmetric device and presents the phase angle value of about −68° in the low-frequency region, not far from an ideal value of −90° which suggests a full capacitive behavior of the device. In the low-frequency region, the frequency dependence of the real and imaginary part of the capacitances ($C'(\omega)$ and $C''(\omega)$) was evaluated (Fig. 10(f)) using a complex capacitance model presented by the following equations [53,54]:

The impedance, $Z(\omega)$ given by

$$Z(\omega) = \frac{1}{j\omega \times C(\omega)} \tag{7}$$

Therefore, $C'(\omega)$ and $C''(\omega)$ can be calculated as follows:

$$C'(\omega) = \frac{Z''(\omega)}{\omega |Z(\omega)|^2} \tag{8}$$

$$C''(\omega) = \frac{Z'(\omega)}{\omega |Z(\omega)|^2} \tag{9}$$

where Z' and Z'' are the real part and the imaginary part of the impedance, respectively, defined as

$$|Z(\omega)|^2 = Z'(\omega)^2 + Z''(\omega)^2 \tag{10}$$

and $\omega = 2\pi f$. $C'(\omega)$ is the real accessible capacitance of the cell that can be delivered and this corresponds to the deliverable capacitance of 0.65 F (Fig. 10(f)). $C''(\omega)$ corresponds to energy loss by the irreversible process of the electrodes [54]. In Fig. 10(f), $C''(\omega)$ shows a peak at 0.2 Hz giving a relaxation time of 4.31 s which is obtained by taking reciprocal of maximum frequency. This value reveals that the device can be fully charged within a short time.

4. Conclusion

In this work, the C-Fe/PANI electrode material was directly synthesized on a current collector by pyrolysis of the iron-PANI mixture coated on nickel foam in a tube furnace under the N_2 atmosphere. The XRD analysis of the as-synthesized C-Fe/PANI electrode material confirmed the diffraction peaks of Fe, Fe_3C, FeS and a broad diffraction peak of graphitized PANI. The Raman and FTIR vibration spectra of C-Fe/PANI revealed features of the graphitized carbon material, PANI functional groups, and Fe—PANI vibration bands. The SEM images of the C-Fe/PANI sample showed agglomerated nanograins. Additionally, HR-TEM images and STEM-EDX analysis confirmed the dispersion of Fe cations on the PANI structure. Furthermore, the XPS analysis confirmed the presence of Fe^{3+} and Fe^{2+} oxidation states in the sample which could be mainly due to iron-carbide, iron-sulfide and iron-nitride configurations. The electrochemical behavior of each working electrode was analyzed in a three-electrode cell configuration using 6 M KOH electrolyte, and thereafter, a symmetric device was successfully fabricated using C-Fe/PANI as a positive and negative electrode. The C-Fe/PANI symmetric device was found to perform at a high applied potential difference of 1.65 V in 6 M KOH. At a current density of 0.5 A g^{-1}, this device exhibited energy and power densities of 41.3 W h kg^{-1} and 231.9 W kg^{-1} respectively. Additionally, the device exhibited a maximum power of 469.4 kW kg^{-1}. Based on the power and energy density, it is suggested that the C-Fe/PANI symmetric device could be classified as "supercapattery" type of electrochemical power sources. The device further showed excellent cycling stability with 100% Columbic efficiency an capacity retention of 72% at a current density of 5 A g^{-1} over 10 000 galvanostatic charge-discharge cycles.

Acknowledgements

This work is based on research supported by the South African Research Chairs Initiative (SARChI) of the Department of Science and Technology and the National Research Foundation of South Africa (Grant No. 61056). Any opinion, finding and conclusion or recommendation expressed in this material is that of the author(s) and the NRF does not accept any liability in this regard. Mologadi N. Rantho acknowledges the financial support from University of Pretoria and NRF through SARChI in Carbon Technology and Materials. J.B. McClimon of the R.W. Carpick laboratory at the University of Pennsylvania is acknowledged for performing XPS measurements.

References

[1] S. Mondal, U. Rana, S. Malik, Reduced graphene oxide/Fe_3O_4/polyaniline nanostructures as electrode materials for an all-solid-state hybrid supercapacitor, J. Phys. Chem. C. 121 (2017) 7573–7583, https://doi.org/10.1021/acs.jpcc.6b10978.
[2] H. Nishide, K. Oyaizu, Toward flexible batteries, Science 319 (5864) (2008) 737–738, https://doi.org/10.1126/science.1151831.
[3] Z. Yang, J. Zhang, M.C. Kintner-Meyer, X. Lu, D. Choi, J.P. Lemmon, J. Liu, Electrochemical energy storage for green grid, Chem. Rev. 111 (5) (2011)

3577–3613, https://doi.org/10.1021/cr100290v (2011).

[4] P. Simon, Y. Gogotsi, Materials for electrochemical capacitors, Nat. Mater. 7 (2008) 845–854, https://doi.org/10.1038/nmat2297.

[5] S.K. Simotwo, C. Delre, V. Kalra, Supercapacitor electrodes based on high-purity electrospun polyaniline and polyaniline-carbon nanotube nanofibers, ACS Appl. Mater. Interfaces 8 (2016) 21261–21269, https://doi.org/10.1021/acsami.6b03463.

[6] G. Zhang, M. Kong, Y. Yao, L. Long, M. Yan, One-pot synthesis of γ-MnS/reduced graphene oxide with enhanced performance for aqueous asymmetric supercapacitors, Nanotechnology 28 (2017), 065402, https://doi.org/10.1088/1361-6528/aa52a5.

[7] G. Feng, S. Li, V. Presser, P.T. Cummings, Molecular insights into carbon supercapacitors based on room-temperature ionic liquids, J. Phys. Chem. Lett. 4 (2013) 3367–3376, https://doi.org/10.1021/jz4014163.

[8] X. Wang, J. Deng, X. Duan, D. Liu, J. Guo, P. Liu, Crosslinked polyaniline nanorods with improved electrochemical performance as electrode material for supercapacitors, J. Mater. Chem. 2 (2014) 12323, https://doi.org/10.1039/C4TA02231A.

[9] V. Kumar, P.S. Lee, Redox active polyaniline-h-MoO_3 hollow nanorods for improved pseudocapacitive performance, J. Phys. Chem. C 119 (2015) 9041–9049, https://doi.org/10.1021/acs.jpcc.5b00153.

[10] X. Zheng, J. Luo, W. Lv, D.W. Wang, Q.H. Yang, Two-dimensional porous carbon: synthesis and ion-transport properties, Adv. Mater. 27 (2015) 5388–5395, https://doi.org/10.1002/adma.201501452.

[11] M.H. Bai, T.Y. Liu, F. Luan, Y. Li, X.X. Liu, Electrodeposition of vanadium oxide-polyaniline composite nanowire electrodes for high energy density supercapacitors, J. Mater. Chem. 2 (2014) 10882–10888, https://doi.org/10.1039/c3ta15391f.

[12] M. Sawangphruk, M. Suksomboon, K. Kongsupornsak, J. Khuntilo, P. Srimuk, Y. Sanguansak, P. Klunbud, P. Suktha, P. Chiochan, High-performance supercapacitors based on silver nanoparticle–polyaniline–graphene nanocomposites coated on flexible carbon fiber paper, J. Mater. Chem. 1 (2013) 9630, https://doi.org/10.1039/c3ta12194a.

[13] K.S. Ryu, K.M. Kim, N.G. Park, Y.J. Park, S.H. Chang, Symmetric redox supercapacitor with conducting polyaniline electrodes, J. Power Sources 103 (2002) 305–309, https://doi.org/10.1016/S0378-7753(01)00862-X.

[14] S. Zhou, H. Zhang, Q. Zhao, X. Wang, J. Li, F. Wang, Graphene-wrapped polyaniline nanofibers as electrode materials for organic supercapacitors, Carbon 52 (2013) 440–450, https://doi.org/10.1016/j.carbon.2012.09.055.

[15] M. Sawangphruk, T. Kaewsongpol, Direct electrodeposition and superior pseudocapacitive property of ultrahigh porous silver-incorporated polyaniline films, Mater. Lett. 87 (2012) 142–145, https://doi.org/10.1016/j.matlet.2012.07.103.

[16] G.A. Snook, P. Kao, A.S. Best, Conducting-polymer-based supercapacitor devices and electrodes, J. Power Sources 196 (2010) 1–12, https://doi.org/10.1016/j.jpowsour.2010.06.084.

[17] S. Bose, T. Kuila, A.K. Mishra, R. Rajasekar, N.H. Kim, J.H. Lee, Carbon-based nanostructured materials and their composites as supercapacitor electrodes, J. Mater. Chem. Mater. Chem. 22 (2012) 767–784, https://doi.org/10.1039/c1jm14468e.

[18] H. Mi, X. Zhang, S. An, X. Ye, S. Yang, Microwave-assisted synthesis and electrochemical capacitance of polyaniline/multi-wall carbon nanotubes composite, Electrochem. Commun. 9 (2007) 2859–2862, https://doi.org/10.1016/j.elecom.2007.10.013.

[19] M. Wu, G.A. Snook, V. Gupta, M. Shaffer, D.J. Fray, G.Z. Chen, Electrochemical fabrication and capacitance of composite films of carbon nanotubes and polyaniline, J. Mater. Chem. 15 (2005) 2297, https://doi.org/10.1039/b418835g.

[20] M.J. Bleda-Martinez, C. Peng, S. Zhang, G.Z. Chen, E. Morallon, D. Cazorla-Amoros, Electrochemical methods to enhance the capacitance in activated carbon/polyaniline composites, J. Electrochem. Soc. 155 (2008) A672, https://doi.org/10.1149/1.2956969.

[21] D. Salinas-Torres, J.M. Sieben, D. Lozano-Castelló, D. Cazorla-Amorós, E. Morallón, Asymmetric hybrid capacitors based on activated carbon and activated carbon fibre-PANI electrodes, Electrochim. Acta 89 (2013) 326–333, https://doi.org/10.1016/j.electacta.2012.11.039.

[22] K.S. Ryu, Y.G. Lee, K.M. Kim, Y.J. Park, Y.S. Hong, X. Wu, M.G. Kang, N.G. Park, R.Y. Song, J.M. Ko, Electrochemical capacitor with chemically polymerized conducting polymer based on activated carbon as hybrid electrodes, Synth. Met. 153 (2005) 89–92, https://doi.org/10.1016/j.synthmet.2005.07.167.

[23] F. Chen, P. Liu, Q. Zhao, Well-defined graphene/polyaniline flake composites for high performance supercapacitors, Electrochim. Acta 76 (2012) 62–68, https://doi.org/10.1016/j.electacta.2012.04.154.

[24] S.S. Umare, B.H. Shambharkar, R.S. Ningthoujam, Synthesis and characterization of polyaniline–Fe_3O_4 nanocomposite: electrical conductivity, magnetic, electrochemical studies, Synth. Met. 160 (2010) 1815–1821, https://doi.org/10.1016/j.synthmet.2010.06.015.

[25] H. Peng, Z. Mo, S. Liao, H. Liang, L. Yang, F. Luo, H. Song, Y. Zhong, B. Zhang, High performance Fe- and N- doped carbon catalyst with graphene structure for oxygen reduction, Sci. Rep. 3 (2013) 1765, https://doi.org/10.1038/srep01765.

[26] N. Daems, X. Sheng, Y. Alvarez-Gallego, I.F.J. Vankelecom, P.P. Pescarmona, Iron-containing N-doped carbon electrocatalysts for the cogeneration of hydroxylamine and electricity in a H_2–NO fuel cell, Green Chem. 18 (2016) 1547–1559, https://doi.org/10.1039/C5GC02197A.

[27] M. Zhao, H. Song, Synthesis of carbon-encapsulated iron carbide/iron nanoparticles from phenolic-formaldehyde resin and ferric nitrate, Mater. Chem. Phys. 124 (2010) 861–864, https://doi.org/10.1016/j.matchemphys.2010.08.011.

[28] C. Röder, T. Weißbach, C. Himcinschi, J. Kortus, S. Dudczig, C.G. Aneziris, Raman spectroscopic characterization of novel carbon-bonded filter compositions for steel melt filtration, J. Raman Spectrosc. 45 (2014) 128–132, https://doi.org/10.1002/jrs.4426.

[29] J. Zhang, C. Liu, G. Shi, Raman spectroscopic study on the structural changes of polyaniline during heating and cooling processes, J. Appl. Polym. Sci. 96 (2005) 732–739, https://doi.org/10.1002/app.21520.

[30] S.K. Pradhan, B.B. Nayak, B.K. Mohapatra, B.K. Mishra, Micro Raman spectroscopy and electron probe microanalysis of graphite spherulites and flakes in cast iron, Metall. Mater. Trans. 38 (2007) 2363–2370, https://doi.org/10.1007/s11661-007-9288-1.

[31] Y. Ren, N. Yan, J. Feng, J. Ma, Q. Wen, N. Li, Q. Dong, Adsorption mechanism of copper and lead ions onto graphene nanosheet/δ-MnO_2, Mater. Chem. Phys. 136 (2012) 538–544, https://doi.org/10.1016/j.matchemphys.2012.07.023.

[32] Y. Zhao, H. Ma, S. Huang, X. Zhang, M. Xia, Y. Tang, Z.F. Ma, Monolayer nickel cobalt hydroxyl carbonate for high performance all-solid-state asymmetric supercapacitors, ACS Appl. Mater. Interfac. 8 (2016) 22997–23005, https://doi.org/10.1021/acsami.6b05496.

[33] R. Li, Z. Hu, X. Shao, P. Cheng, S. Li, W. Yu, W. Lin, D. Yuan, Large scale synthesis of NiCo layered double hydroxides for superior asymmetric electrochemical capacitor. Sci. Rep. 6 (2016), 18737 https://doi.org/10.1038/srep18737.

[34] G.H. Le, A.Q. Ha, Q.K. Nguyen, K.T. Nguyen, P.T. Dang, H.T.K. Tran, L.D. Vu, T.V. Nguyen, G.D. Lee, T.A. Vu, Removal of Cd^{2+} and Cu^{2+} ions from aqueous solution by using Fe–Fe_3O_4/graphene oxide as a novel and efficient adsorbent, Mater. Res. Express 3 (2016), 105603, https://doi.org/10.1088/2053-1591/3/10/105603.

[35] G. Wu, C.M. Johnston, N.H. Mack, K. Artyushkova, M. Ferrandon, M. Nelson, J.S. Lezama-Pacheco, S.D. Conradson, K.L. More, D.J. Myers, P. Zelenay, Synthesis–structure–performance correlation for polyaniline–Me–C non-precious metal cathode catalysts for oxygen reduction in fuel cells, J. Mater. Chem. 21 (2011) 11392, https://doi.org/10.1039/c0jm03613g.

[36] X. Feng, Z. Yan, N. Chen, Y. Zhang, X. Liu, Y. Ma, X. Yang, W. Hou, Synthesis of a graphene/polyaniline/MCM-41 nanocomposite and its application as a supercapacitor, New J. Chem. 37 (2013) 2203, https://doi.org/10.1039/c3nj00108c.

[37] S.K. Lai, C.M. Luk, L. Tang, K.S. Teng, S.P. Lau, Photoresponse of polyaniline-functionalized graphene quantum dots, Nanoscale 7 (2015) 5338–5343, https://doi.org/10.1039/C4NR07565J.

[38] Y. Luo, D. Kong, Y. Jia, J. Luo, Y. Lu, D. Zhang, K. Qiu, C.M. Li, T. Yu, Self-assembled graphene@PANI nanoworm composites with enhanced supercapacitor performance, RSC Adv 3 (2013) 5851, https://doi.org/10.1039/c3ra00151b.

[39] Y. He, J. Pan, L. Wu, Y. Zhu, X. Ge, J. Ran, Z. Yang, T. Xu, A novel methodology to synthesize highly conductive anion exchange membranes, Nat. Publ. Gr (2015), https://doi.org/10.1038/srep13417.

[40] K.O. Oyedotun, M.J. Madito, A. Bello, D.Y. Momodu, A.A. Mirghni, N. Manyala, Investigation of graphene oxide nanogel and carbon nanorods as electrode for electrochemical supercapacitor, Electrochim. Acta 245 (2017) 268–278, https://doi.org/10.1016/j.electacta.2017.05.150.

[41] B. Akinwolemiwa, C. Peng, G.Z. Chen, Redox electrolytes in supercapacitors, J. Electrochem. Soc. 162 (2015) A5054–A5059, https://doi.org/10.1149/2.0111505jes.

[42] G. Godillot, L. Guerlou-Demourgues, P.L. Taberna, P. Simon, C. Delmas, Original conductive Nano-Co_3O_4 investigated as electrode material for hybrid supercapacitors, Electrochem. Solid State Lett. 14 (2011) A139, https://doi.org/10.1149/1.3609259.

[43] A. Laheäär, P. Przygocki, Q. Abbas, F. Béguin, Appropriate methods for evaluating the efficiency and capacitive behavior of different types of supercapacitors, Electrochem. Commun. 60 (2015) 21–25, https://doi.org/10.1016/j.elecom.2015.07.022.

[44] X. Rui, H. Tan, Q. Yan, Nanostructured metal sulfides for energy storage, Nanoscale 6 (2014) 9889, https://doi.org/10.1039/C4NR03057E.

[45] B. Conway, J.C. Ku, F. Ho, The electrochemical surface reactivity of iron sulfide, FeS_2, J. Colloid Interface Sci. 75 (1980) 357–372, https://doi.org/10.1016/0021-9797(80)90461-0.

[46] C. Yuan, X. Zhang, L. Su, B. Gao, L. Shen, Facile synthesis and self-assembly of hierarchical porous NiO nano/micro spherical superstructures for high performance supercapacitors, J. Mater. Chem. 19 (2009) 5772–5777, https://doi.org/10.1039/B902221J.

[47] D.P. Dubal, O. Ayyad, V. Ruiz, P. Gómez-Romero, Hybrid energy storage: the merging of battery and supercapacitor chemistries, Chem. Soc. Rev. 44 (2015) 1777–1790, https://doi.org/10.1039/C4CS00266K.

[48] L. Yu, G.Z. Chen, Redox electrode materials for supercapatteries, J. Power Sources 326 (2016) 604–612, https://doi.org/10.1016/j.jpowsour.2016.04.095.

[49] M. Dirican, M. Yanilmaz, X. Zhang, S. Mondal, K. Barai, N. Munichandraiah, et al., Free-standing polyaniline–porous carbon nanofiber electrodes for symmetric and asymmetric supercapacitors, RSC Adv. 4 (2014) 59427–59435, https://doi.org/10.1039/C4RA09103E.

[50] Y. Zhou, H. Xu, N. Lachman, M. Ghaffari, S. Wu, Y. Liu, A. Ugur, K.K. Gleason, B.L. Wardle, Q.M. Zhang, Advanced asymmetric supercapacitor based on

conducting polymer and aligned carbon nanotubes with controlled nanomorphology, Nano Energy 9 (2014) 176–185 doi.org/10.1016/j.nanoen.2014.07.007.

[51] W. Sun, X. Chen, Preparation and characterization of polypyrrole films for three-dimensional micro supercapacitor, J. Power Sources 193 (2009) 924–929, https://doi.org/10.1016/j.jpowsour.2009.04.063.

[52] H. Li, J. Wang, Q. Chu, Z. Wang, F. Zhang, S. Wang, Theoretical and experimental specific capacitance of polyaniline in sulfuric acid, J. Power Sources 190 (2009) 578–586, https://doi.org/10.1016/j.jpowsour.2009.01.052.

[53] T.M. Masikhwa, F. Barzegar, J.K. Dangbegnon, A. Bello, M.J. Madito, D. Momodu, et al., Asymmetric supercapacitor based on VS_2 nanosheets and activated carbon materials, RSC Adv. (2016), https://doi.org/10.1039/C5RA27155J.

[54] P.L. Taberna, P. Simon, J.-F.F. Fauvarque, Electrochemical characteristics and impedance spectroscopy studies of carbon-carbon supercapacitors, J. Electrochem. Soc. 150 (2003) A292–A300, https://doi.org/10.1149/1.1543948.

Chapter 6

Asymmetric supercapacitor based on VS_2 nanosheets as a cathode and C-Fe/PANI as an anode

6.1 Introduction

This chapter presents the experimental findings on the structural and morphological characterization of the as-synthesized electrode materials (i.e. VS_2 nanosheets and C-Fe/PANI) and the electrochemical properties of the electrodes and fabricated VS_2//C-Fe/PANI asymmetric device.

6.2 Results and discussion

The structural, morphological and compositional characterization of the as-synthesized electrode materials was carried out using different techniques such as X-ray diffraction (XRD), Raman spectroscopy, Fourier transform

infrared (FT-IR) spectroscopy and scanning electron microscopy (SEM). The electrochemical properties of the working electrodes (VS_2 nanosheets and C-Fe/PANI) were evaluated in a three-electrode cell configuration using 6 M KOH electrolyte, and thereafter, asymmetric device based on VS_2 nanosheets as a cathode and C-Fe/PANI as an anode was successfully fabricated.

Similar to the previous chapter, the results for structural, morphological and composition characterization are discussed in the attached publication below, including the electrochemical characterization.

6.3 Publication

Electrochimica Acta 260 (2018) 11–23

Contents lists available at ScienceDirect

Electrochimica Acta

journal homepage: www.elsevier.com/locate/electacta

Asymmetric supercapacitor based on vanadium disulfide nanosheets as a cathode and carbonized iron cations adsorbed onto polyaniline as an anode

M.N. Rantho, M.J. Madito, F.O. Ochai-Ejeh, N. Manyala*

Department of Physics, Institute of Applied Materials, SARChI Chair in Carbon Technology and Materials, University of Pretoria 0028, South Africa

ARTICLE INFO

Article history:
Received 12 August 2017
Received in revised form
2 November 2017
Accepted 12 November 2017
Available online 13 November 2017

Keywords:
Supercapacitor
Asymmetric device
VS_2 nanosheets
Iron-PANI
Energy storage

ABSTRACT

VS_2 nanosheets electrode material was successfully synthesized by the hydrothermal method, and the electrode material (C-Fe/PANI) based on the carbonization of Fe cations adsorbed onto polyaniline (PANI) was directly synthesized on a nickel foam (current collector) by pyrolysis of the iron-PANI mixture coated on nickel foam in a tube furnace under the N_2 atmosphere. The structural and morphological characterization of the as-synthesized electrode materials was carried out using X-ray diffraction (XRD), Raman spectroscopy, Fourier transform infrared (FT-IR) spectroscopy and scanning electron microscopy (SEM). The electrochemical behavior of each working electrode was analyzed in a three-electrode cell configuration using 6 M KOH electrolyte, and thereafter, a hybrid (asymmetric) device was successfully fabricated using VS_2 nanosheets as the positive electrode and C-Fe/PANI as a negative electrode. The fabricated VS_2//C-Fe/PANI asymmetric device was found to perform at a high applied potential difference of 1.7 V in 6 M KOH. At a current density of 2 A g^{-1}, this device exhibited high energy and power densities of 27.8 Wh kg^{-1} and 2991.5 W kg^{-1} respectively. In addition, a VS_2//C-Fe/PANI device showed excellent cycling stability with 95% capacity retention over 10,000 galvanostatic charge-discharge cycles at a current density of 5 A g^{-1}.

1. Introduction

Supercapacitors (SCs) which are also referred to as electrochemical capacitors (ECs) have attracted great interest for the important application in the area of electrochemical energy storage because of increasing demand for digital communication, electric vehicles and other electric devices at high pulse power level [1–7]. Since, SCs are high power-delivery storage devices which are able to discharge in a shorter time by exploiting their fast surface or near surface reactions and delivering high power compared to conventional batteries [2,8–10]. Though, SCs are high power-delivery storage devices (have high power density) they have low energy density especially compared to rechargeable batteries (Li-ion batteries) [2,11]. Accordingly, research focus in SCs is on improving their energy density (i.e. ~5–8 Wh kg^{-1}) without compromising their high power density (i.e. ~5–30 kW kg^{-1}), unlike in rechargeable batteries which already have high energy density in the range of 120–200 Wh kg^{-1}, the focus will be on improving the power density which is in the range of 0.4–3 kW kg^{-1} [2,8,9,12]. Recently, asymmetric (hybrid) systems have been explored to increase the operating electrode potential to improve the energy density of the SCs. Generally, the behavior of the SCs is mainly influenced by the charge storage mechanism which is divided into two classifications, namely, the electric double layer capacitors (EDLCs) and pseudocapacitors [1,2,13]. In EDLCs, the predominant energy storage is achieved by double-layer capacitance, and in this charge storage process, there is no transfer of charges. On the other hand, in pseudocapacitors, the electrical energy is stored faradaically by electron charge transfer between electrode and electrolyte [2]. This is accomplished through electrosorption, reduction-oxidation reactions (redox reactions), and intercalation processes, called pseudocapacitance.

The electrochemical capacitors have three main categories of electrode materials which are carbon materials such as carbon nanotubes, transition metal oxides (e.g. MnO_2 and RuO_2), and electrochemically conducting polymers, for instance, polyaniline (PANI) and polypyrrole [14–17]. Among various pseudocapacitive materials that have been studied, PANI has attracted great attention

* Corresponding author.
E-mail address: ncholu.manyala@up.ac.za (N. Manyala).

https://doi.org/10.1016/j.electacta.2017.11.074
0013-4686/

as one of the most promising pseudocapacitive polymer material suitable for the next generation of supercapacitors. This is due to its attractive properties such as high pseudocapacitance, light weight, low cost, controllable electrical conductivity, high energy density, facile synthesis, and environmental friendliness [18–21]. PANI is often used as electrode material for supercapacitors and it has three oxidation states (leucoemeraldine, emeraldine salt, and pernigraniline) which contribute to its high specific capacitance [22]. Among its three oxidation states, the emeraldine salt has lower electronic conductivity than that of typical metals [23]. The need to develop high-performance SCs has led to the incorporation of metals and metal oxide particles into PANI to enhance its electronic conductivity [24]. It has been shown that iron-containing nitrogen-doped graphitic carbon materials, carbonized PANI in particular, achieve high electrocatalytic performance and exhibit high cycling stability [15,16]. Generally, carbonaceous materials with Fe cations have shown enhanced electrochemical performance as the negative electrode materials for SCs, including iron oxides and hydroxides [25–27]. Therefore, the synthesis of carbonized Fe-PANI hybrid material is promising for achieving high-performance SCs. In this study, Fe cations are found to be interesting since they can easily adsorb onto PANI by the complexation and electrostatic interactions due to the active binding sites present in functional groups on PANI [18,28–30].

Until now, transition metal oxides/sulfides and layered transition-metal dichalcogenides (TMDs) such as MoS_2, VS_2, WS_2, FeS_2, CoS_2, and NiS_2 have been successfully established as new paradigm in the chemistry of nanomaterials especially for nanotubes and fullerene-like nanostructures as well as the graphene analogs and have been extensively investigated as the positive electrode materials for SCs due to their high faradic capacitance [31–35]. On the other hand, VS_2 has not received much attention in two electrode supercapacitor devices. However, it has been investigated for applications in SCs due to its promising electrochemical performance. Recently, Feng et al. [36], reported all-in-solution route to synthesize VS_2 phase for the first time, taking advantage of an intermediate intercalated compound precursor of $VS_2 \cdot NH_3$. This report clearly demonstrated that VS_2 nanosheets are highly conductive and have a high specific capacitance, showing promising signs for 2D material to be utilized in energy storage devices. Masikhwa et al. [37], reported the design of an asymmetric supercapacitor based on 3D interconnected activated carbon as the negative electrode and mesoporous VS_2 nanosheets as the positive electrode material. The report suggests that pairing hybrid materials could be an excellent method to produce SCs with high energy and power densities.

Although studies about VS_2 electrode for supercapacitor applications have been reported in the literature, there are rare studies done on the binder-free electrode material based on carbonized Fe cations adsorbed onto PANI (C-Fe/PANI) and until now there are no reports on VS_2//C-Fe/PANI asymmetric cell device. Herein, we report on asymmetric supercapacitor based on VS_2 nanosheets as a cathode and C-Fe/PANI as an anode. This study focuses on structural, and morphological characterization of the as-synthesized electrode materials and the electrochemical properties of VS_2//C-Fe/PANI asymmetric device. The VS_2//C-Fe/PANI asymmetric device was found to perform at a high applied potential difference of 1.7 V in 6 M KOH. At a high current density of 2 A g^{-1}, this device exhibited energy and power densities of 27.8 Wh kg^{-1} and 2991.5 W kg^{-1} respectively. In addition, a VS_2//C-Fe/PANI device showed excellent cycling stability with 95% capacity retention for 10 000 galvanostatic charge-discharge cycles at a current density of 5 A g^{-1}.

2. Experimental

2.1. Materials

All the reagents used in this work are of analytical grade and were used as received without further purification. For VS_2 nanosheets synthesis: Sodium orthovanadate (1 mM Na_3VO_4, purity 99.98%) and thioacetamide (5 mM C_2H_5NS, purity ≥99%), were purchased from Sigma Aldrich. For C-Fe/PANI synthesis: Aniline hydrochloride ($C_6H_5NH_2 \cdot HCl$, purity ≥99%), ammonium persulphate ($(NH_4)_2S_2O_8$, purity ≥99%) and iron nitrate nonahydrate ($Fe(NO_3)_3 \cdot 9H_2O$, purity ≥99.95%) were also purchased from Sigma Aldrich. Polycrystalline nickel foam (Ni-F) used as a current collector which is a 3D scaffold template with an areal density of 420 g m^2 and thickness of 1.6 mm was purchased from Alantum (Munich, Germany).

2.2. Synthesis of VS_2 nanosheets using hydrothermal method

VS_2 nanosheets were synthesized by the hydrothermal method as shown in Scheme 1(a). In the synthesis, 1.65 g of 1 mM Na_3VO_4 and 3.37 g of 5 mM C_2H_5NS were dissolved in 120 mL of deionized water and stirred for 1 h at room temperature using a magnetic stirrer. After stirring, the resultant solution was transferred into a sealed, 150 mL Teflon-lined, stainless-steel autoclave and kept at a temperature of 160 °C for 24 h and then cooled naturally down to the room temperature. Subsequently, the obtained precipitate was filtered and washed with deionized water several times and dried at 60 °C overnight. Finally, the recovered product of VS_2 nanosheets was obtained as displayed by micrograph in Scheme 1(a).

2.3. Synthesis of C-Fe/PANI

For PANI synthesis: 0.2 M aniline hydrochloride was added to a 50 mL solution of 1.0 M HCl, and in a separate beaker 0.25 M solution of ammonium persulphate was added to 1.0 M HCl. The prepared solutions were kept for 1 h at room temperature, thereafter, they were mixed and stirred for about an hour and left to polymerize. After polymerization, PANI precipitate was collected on a filter (after been washed several times with 100 mL of 0.2 M HCl, and acetone) and dried at 60 °C overnight. Furthermore, PANI was used as a substrate for adsorbing Fe cations. Briefly, 0.2 g of $Fe(NO_3)_3 \cdot 9H_2O$ and 0.0125 g of PANI were dissolved in 50 mL of ethanol and sonicated in ultra-sonication bath until the ethanol was almost completely evaporated. Thereafter, the slurry was coated on nickel foam (current collector) which was loaded in a tube furnace and heated to 850 °C and pyrolyzed for 2 h under the N_2 atmosphere. After pyrolysis, the as-synthesized sample which shows homogeneously dispersed nanograin particles (Scheme 1(b)) was used as the negative electrode (i.e. without a binder).

2.4. Structural, and morphological characterization

The crystallite structure analysis of the as-synthesized VS_2 and C-Fe/PANI materials was carried out using X-ray diffraction (XRD) XPERTPRO diffractometer (PANalytical BV, Netherlands) with theta/2 theta geometry, operating with a cobalt (Co) tube at 50 kV and 30 mA. A T64000 micro-Raman spectrometer (HORIBA Scientific, Jobin Yvon Technology) with a 514 nm laser wavelength and spectral acquisition time of 120 s was used to characterize the as-synthesized electrode materials. The Raman system laser power was set as low as 3 mW in order to minimize heating effects. Fourier transform infrared (FT-IR) spectroscopy performed in the range of

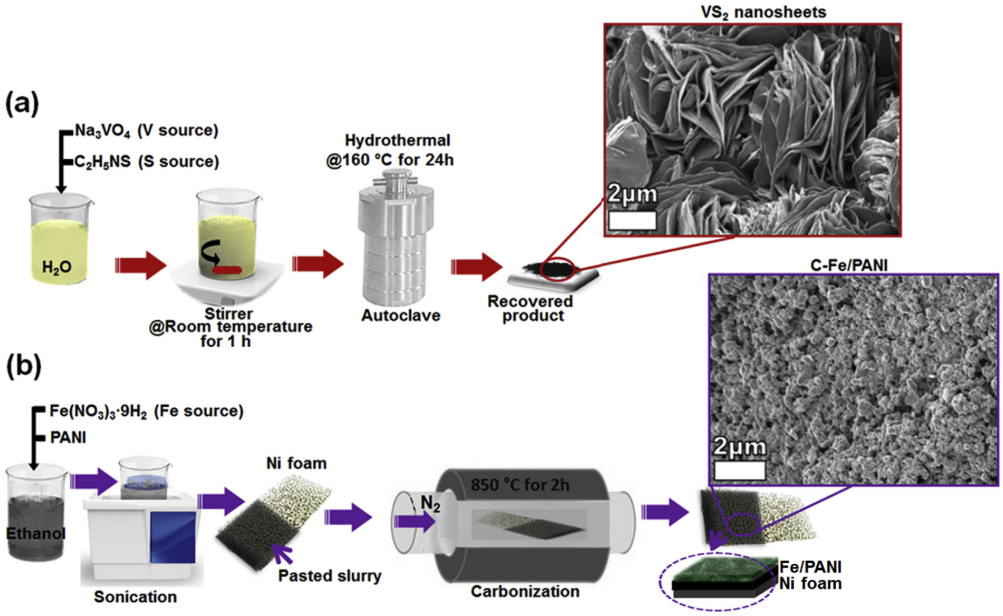

Scheme 1. Schematic illustration of the synthesis route for (a) VS_2 nanosheets and (b) carbonized iron cations adsorbed onto polyaniline (C-Fe/PANI).

400–4000 cm^{-1} using Perkin Elmer Spectrum RX I FT-IR system was used to characterize VS_2 and C-Fe/PANI materials. The scanning electron microscopy (SEM) images were obtained using a Zeiss Ultra Plus 55 field emission scanning electron microscope (FE-SEM) operated at 2.0 kV to obtain the morphology of the VS_2 and C-Fe/PANI materials.

2.5. Electrochemical characterization

All electrochemical analysis were carried out on a Biologic VMP-300 potentiostat (Knoxville TN 37,930, USA) controlled by the EC-Lab V10.37 software at room temperature. In the three-electrode system, a glassy carbon plate was used as the counter electrode and Ag/AgCl (3 M KCl) electrode served as the reference electrode. The working electrode (VS_2 nanosheets) was prepared by coating a mixture of 80 wt% active material, 10 wt% carbon black and 10 wt% polyvinylidene fluoride (PVDF) binder dispersed in N-methyl-pyrrolidone (NMP) solution onto a piece of nickel foam (1×1 cm^2). After coating, the as-synthesized electrode was dried at 60 °C overnight, and thereafter, the coated active material was pressed onto the nickel foam under a pressure of 30 MPa. However, the other working electrode (C-Fe/PANI) was prepared without a binder as discussed in the synthesis method (Scheme 1(b)). Briefly, a mixture of Fe and PANI dissolved in ethanol was sonicated until the ethanol was almost completely evaporated, and thereafter, the slurry was coated on nickel foam (i.e. on both sides of the foam for three electrode and on one side for two electrode measurements) which was loaded in a tube furnace and heated to 850 °C and pyrolyzed for 2 h under the N_2 atmosphere. After pyrolysis, the as-synthesized sample was used as the negative electrode. The electrochemical measurements of VS_2 and C-Fe/PANI electrodes were carried out in the three-electrode system in 6 M KOH aqueous electrolyte solution. Cyclic voltammetry (CV) was performed at scan rates of 5–100 mV s^{-1} in the applied potential range of 0.0–0.5 V vs. Ag/AgCl and 0.0 to −1.2 V vs. Ag/AgCl for the positive and negative electrode, respectively. The galvanostatic charge/discharge (GCD) curves for both working electrodes were tested. The electrochemical impedance spectroscopy (EIS) was measured in an open circuit potential over a frequency range of 10 mHz–100 kHz. The electrochemical analysis of the active material was also evaluated in a two-electrode asymmetric device. In the two-electrode asymmetric device (VS_2//C-Fe/PANI), VS_2 and C-Fe/PANI electrode served as a positive and negative electrode, respectively.

3. Results and discussion

3.1. Structural and morphological characterization

Fig. 1(a) shows the XRD pattern of the as-synthesized VS_2 sample which shows the characteristic diffraction peaks of VS_2 with clear main two diffraction peaks corresponding to (001) and (011). The XRD pattern agrees with the one reported in the literature of VS_2 nanosheets synthesized using the hydrothermal method [36]. In Fig. 1(a), the diffraction peaks were indexed using the matching Inorganic Crystal Structure Database (ICSD) card no. 86519 with chemical formula VS_2, space-group $P\,-3\,m\,1$ and cell parameters $a = 3.221$ Å and $c = 5.755$ Å. From Fig. 1(b) it can be seen that vanadium disulfide is a hexagonal layered transition metal dichalcogenide with each layer composing of one vanadium sheet sandwiched between the two sulfur sheets. The sandwiches are separated by van der Waals gap [38]. The unit cell and the molecule of the VS_2 shown Fig. 1(b) are based on Crystallographic Information File (CIF) of ICSD card no. 86519.

Figure S1 (supporting information) shows the XRD of the as-synthesized C-Fe/PANI sample which displays very strong diffraction peaks of the Ni (current collector) which suppresses the weak diffraction peaks of the active material. To avoid the Ni diffraction,

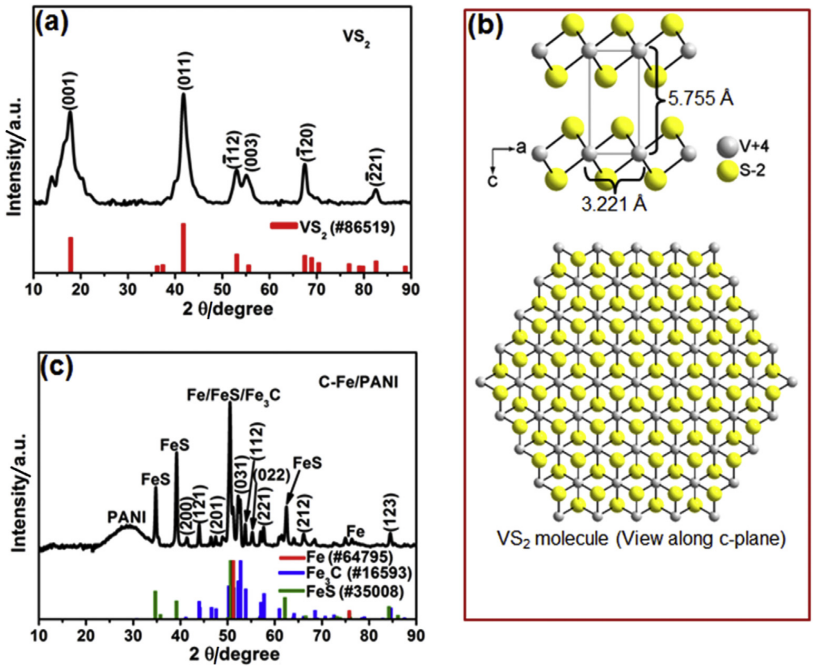

Fig. 1. (a) The XRD pattern of the as-synthesized VS_2 nanosheets and the matching ICSD card. (b) The unit cell and the molecule of the VS_2 based on CIF of the matching ICSD card. (c) The XRD pattern of the as-synthesized C-Fe/PANI without current collector and the matching ICSD cards for Fe, Fe_3C and FeS.

the C-Fe/PANI was prepared without Ni foam and Fig. 1(c) shows the XRD of the sample. The diffraction peaks for C-Fe/PANI sample were indexed using the matching ICSD card no. 16593 with chemical formula Fe_3C, crystal system: orthorhombic and space-group: *P n m a*. In addition, the other diffraction peaks that did not match the ICSD card no. 16593 for Fe_3C were found to match the ICSD card no. 35008 for FeS (crystal system: orthorhombic and space-group: *P n m a*.) which suggests that during the pyrolysis process the degradation of ammonium persulphate from PANI synthesis generated iron sulfide. Furthermore, A diffraction peak at about 52° could also be due to metallic Fe in addition to Fe_3C and FeS, because during the pyrolysis process, Fe cations could be reduced to metallic iron by the reaction with pyrolytic carbon from PANI [39]. A broad diffraction peak at about 30° (PANI) is assigned to the XRD graphitic plane (002), indicating a graphitization of carbon material. In fact, the phenyl groups of PANI easily produce a graphitic structure during pyrolysis, thus leading to enhanced electrical conductivity [40].

The chemical structure of the as-synthesized VS_2 was investigated using the Raman and FTIR vibration spectra as shown in Fig. 2(a). The Raman spectrum of VS_2 reveals vanadium disulfide characteristic vibration bands at approximately 140, 285 and 405 cm^{-1} which are E_{1g}, E_{2g} and A_{1g} respectively, corresponding to the in-plane (E) and out-of-plane (A) modes of S–V–S (Fig. 2(b)). Similar characteristic vibration bands were previously observed for 2H-TaS_2 by Sugai et al. [41]. In fact, the Raman signal of VS_2 is similar to that of other group V metal sulfides [41,42]. FTIR vibration spectrum of VS_2 (Fig. 2(a)) shows the characteristic V–S stretching vibration band of VS_2 below 600 cm^{-1} and in the range of ~800–4000 cm^{-1} the observed vibration bands may originate from the oxidation of VS_2 and absorbed gas molecules on the surface of VS_2 nanosheets during exposure to the atmosphere.

Similarly, the chemical structure of the as-synthesized C-Fe/PANI was also investigated using the Raman and FTIR vibration spectra (Fig. 2(c)). The Raman spectrum of C-Fe/PANI reveals features of the graphitized carbon material, namely the D band (~1350 cm^{-1}) which is a breathing mode of sixfold rings (A_{1g} symmetry) and becomes active in the presence of disorder in the carbon lattice sites, and G band (~1602 cm^{-1}) which involves in-plane bond stretching displacements of sp^2 carbon atoms (E_{2g} symmetry) (Fig. 2(d)) [43]. The observed vibration bands in the range of 1240–1700 cm^{-1} are attributed to PANI functional groups. Generally, the Raman spectrum of PANI reveals functional groups at approximately 1610 cm^{-1} (C–C stretching), 1585 cm^{-1} (C=C stretching), 1490 cm^{-1} (C=N stretching), 1412 cm^{-1} (C–C stretching), 1346 cm^{-1} (C–N stretching), 1210 cm^{-1} (C–N stretching) [18,30]. Furthermore, the vibration bands at about 781 and 895 cm^{-1} are associated with the deformation of amine, imine, and benzenoid/quinoid rings [18], and the bands at about 215, 280, 395, and 505 cm^{-1} originate from Fe–PANI (e.g. Fe–C, Fe–N, Fe–S, etc.) vibration bands which are similar to those reported by Pradhan et al. [44]. In view of the FTIR spectra of C-Fe/PANI, the functional groups of PANI are observable at the IR bands of 1583 cm^{-1} (C=C stretching of the quinoid ring), 1296 cm^{-1} (C–H in-plane bending) and 1139 cm^{-1} (C–C stretching) [18]. In addition, the functional groups of PANI are also found at ~3715 and 3420 cm^{-1} (N–H stretching), and 2922 cm^{-1} (C–H stretching), however, the broad vibration band in the range of 3010–3680 cm^{-1} is usually assigned to O–H stretching vibrations [18,45–47]. No characteristic peaks of Fe–S or Fe–O vibrations at ~500-600 cm^{-1} are observed.

The morphology of as-synthesized layered structure of VS_2 was examined using SEM and the results are shown in Fig. 3(a) and (b)

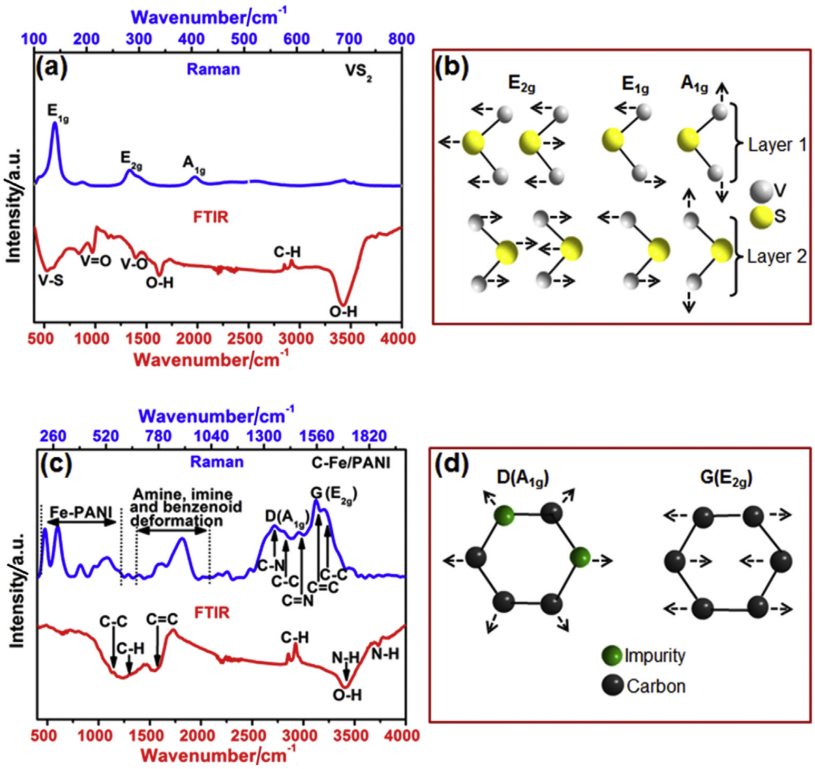

Fig. 2. (a) The Raman and FTIR vibration spectrum of the as-synthesized VS_2 nanosheets, and (b) the schematic view of the corresponding Raman vibrational modes. (c) The Raman and FTIR vibration spectrum of the as-synthesized C-Fe/PANI, and (d) the schematic view of the breathing mode of sixfold rings (A_{1g} symmetry) and the in-plane bond stretching displacements of sp^2 carbon atoms (E_{2g} symmetry).

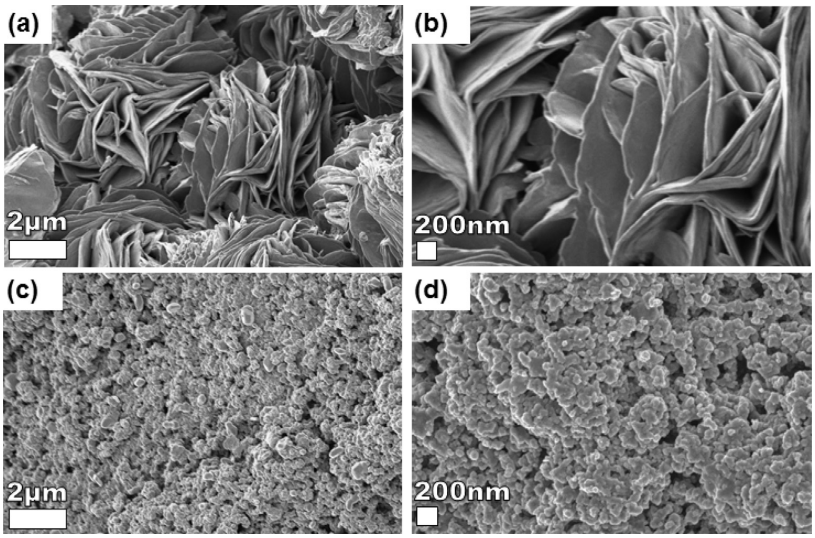

Fig. 3. (a) Low and (b) high magnification SEM images of the as-synthesized layered structure of VS_2. (c) Low and (d) high magnification SEM images of as-synthesized C-Fe/PANI.

at low and high magnification respectively. It can be seen from these figures that the sample is composed of a large number of nanosheets. The morphology of the C-Fe/PANI sample was also examined using SEM and the results are shown in Fig. 3(c) and (d). At low magnification, in Fig. 3(c), it can be seen that the crystallites are agglomerated and well distributed all over the sample surface suggesting that Fe cations adsorbed onto polyaniline are uniformly dispersed on the surface of the C-Fe/PANI sample.

3.2. Electrochemical characterization

Before fabricating a two-electrode asymmetric device based on VS_2 nanosheets as a cathode and C-Fe/PANI as an anode, the electrochemical performances of the VS_2 and C-Fe/PANI electrodes were evaluated in three-electrode cell configuration. Firstly, the cyclic voltammetry (CV) of the cathode (VS_2 nanosheets) was evaluated in three-electrode cell configuration using 1 M KOH, 6 M KOH and 1 M Na_2SO_4 electrolytes, as shown in Fig. 4(a) (also see Fig. S2 (supporting information)). From the figure it can be seen that VS_2 electrode performs better (has a highest current response) in KOH than in Na_2SO_4, this is due to the difference in the hydrated radius of K^+ ions (0.331 nm) and Na^+ ions (0.358 nm). The lower hydrated radius of K^+ ions favors enhanced ionic mobility and interaction with the electrode material. Furthermore, it is worth mentioning that the reported conductivity of K^+ ions is higher than that of Na^+ ions at room temperature [48]. K^+ ions acquire small charge density, i.e. weak solvation interactions with the water molecule that favors easier polarization during the de-solvation processes. This causes an easy passage of K^+ ions into the electrode during the redox reactions. In addition, the OH^- anion has the highest ionic conductivity among anions [48]. The high concentration of 6 M KOH also increases the number of ions and therefore the ionic conductivity of the electrolyte. The VS_2 in KOH electrolyte also shows faradic behavior which leads to much higher specific capacitance compared to using Na_2SO_4. In Fig. 4(b) the CV curves of VS_2 and Ni-F are shown, to illustrate that Ni-F has no obvious influence in the observed redox peaks (a reduction and oxidation peaks at 0.15 V and 0.31 V respectively) of VS_2 which clearly shows that these peaks are from VS_2

The CV curves of VS_2 electrode are shown in Fig. 5(a) at different scan rates of 5, 10, 20, 50, and 100 mV s^{-1}. The curves of VS_2 electrode reveal the presence of two redox peaks which are due to the electrochemical redox reactions arising from the presence of oxygen functionalities which have high redox reactivity characteristics in the positive potential window [49]. The observed redox peaks in the CV curves of VS_2 electrode indicates the faradic behavior of the electrode. Furthermore, the GCD curves of VS_2 electrode are shown in Fig. 5(b) at current densities of 0.5, 1, 2, 3, and 5 A g^{-1}. The discharge curves show potential steps, i.e. a fast potential drop (0.41–0.25 V) and slow potential drop (0.25–0.18 V) which confirms the faradic behavior of the VS_2 electrode as suggested by CV curves. Fig. 5(c) shows the CV curves of C-Fe/PANI at different scan rates ranging from 5 to 100 mV s^{-1}. The CV curves of C-Fe/PANI show relatively rectangular shapes, which is a typical EDLC sample behavior. In addition, the GCD curves of C-Fe/PANI at various current densities ranging from 0.5 to 5.0 A g^{-1} are shown in Fig. 5(d). These curves show pseudocapacity behavior, thus, illustrating mostly EDLC behavior in agreement with the CV curves of the C-Fe/PANI electrode. Furthermore, for both VS_2 and C-Fe/PANI electrode the specific capacitance, C_S of the electrode was calculated from the CV curves integrals, as shown in Fig. 5(e), using the following equation [2,50,51]:

$$C_S = \frac{\int I(V)dV}{m\nu\Delta V} \quad (1)$$

where m is the total mass of the active material (g), ν is the scan rate (V s^{-1}), $\Delta V = V_f - V_i$, and V_f and V_i are the integration potential limits of the CV curve (V), and I (V) is the CV current (A).

In addition, the specific capacity (Q_S) for both VS_2 and C-Fe/PANI electrode showing the EDLC and faradic behavior respectively, was calculated from the GCD curves, as shown in Fig. 5(f), using the following equation [2,50–53]:

$$Q_S = \left(\frac{I}{m}\right)\frac{t}{3.6} \quad (2)$$

where I is the applied current (A), m is the total mass of the active material (g), and t is the time taken for a complete discharge cycle (s).

In Fig. 5(e), it can be seen that at a scan rate of 5 mV s^{-1}, VS_2 electrode exhibit a high specific capacitance of 516.5 F g^{-1} than C-Fe/PANI electrode which exhibit a specific capacitance of 486.5 F g^{-1}. Additionally, from Fig. 5(f) it can also be seen that C-Fe/PANI exhibits higher specific capacity than VS_2. The specific capacities of C-Fe/PANI and VS_2 at current density of 0.5 A g^{-1} are 106.7 and 81.0 mA h g^{-1}, respectively. It is clear that the specific capacitance and capacity continuously decrease with increasing scan rate and current density for both working electrodes. Generally this may be due to the increasing electronic field within the cell setup, increased by increase in scan rate or current density which alters both Faradic and EDLC processes. In addition, the observed

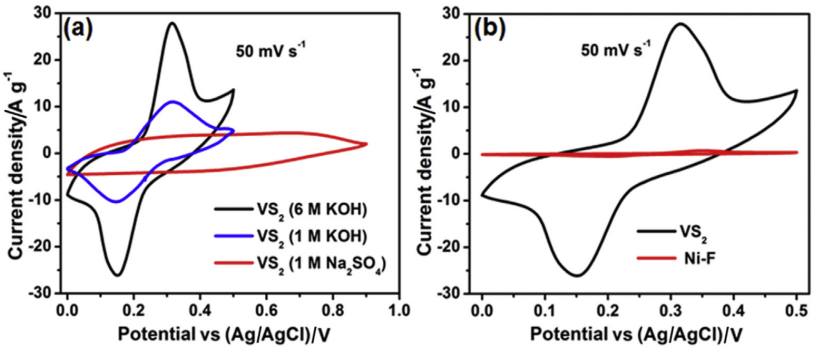

Fig. 4. (a) CV curves of VS_2 in different electrolytes at a scan rate of 50 mV s^{-1} (b) CV curves of VS_2 and Ni foam (Ni-F) at a scan rate of 50 mV s^{-1}.

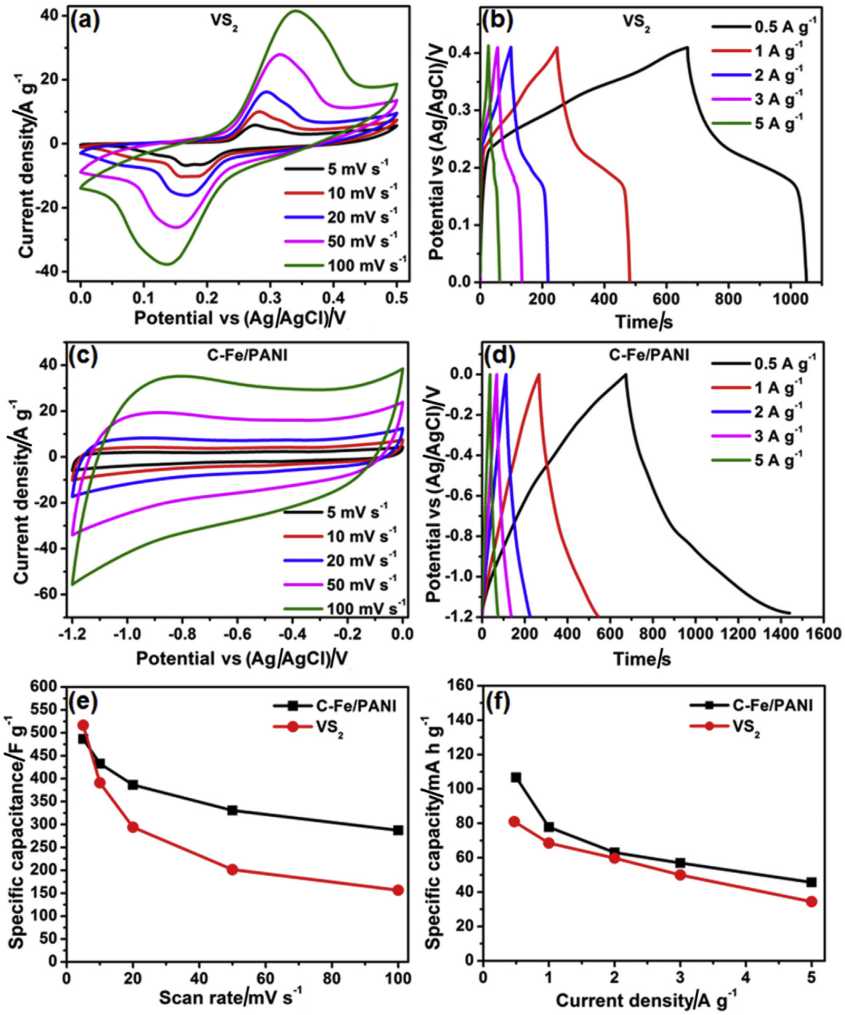

Fig. 5. (a) CV curves of VS_2 electrode at different scan rates in a potential window range of 0.0–0.5 V. (b) CD curves of the VS_2 electrode at different current densities. (c) CV curves of C-Fe/PANI electrode at different scan rates in a potential window range of −1.2 to 0.0 V. (d) CD curves of the C-Fe/PANI electrode at different current densities. (e) Specific capacitance as a function of scan rate for both VS_2 and C-Fe/PANI electrode. (f) The specific capacity of both C-Fe/PANI and VS_2 electrodes as a function of current density.

decrease in the specific capacity can also be attributed to the ion exchange mechanism where at low current density, a high specific capacity is obtained because the OH^- has enough time to be intercalated/extracted into/out of the electrode during charging/discharging [54]. However, at high current density, a low specific capacity is obtained because less charge is transferred between electrolyte and the electrode. The charge storing capacity of C-Fe/PANI was further compared to carbonized PANI (C-PANI) where the C-PANI electrode was prepared in the similar way as C-Fe/PANI electrode without incorporating Fe. From Fig. S3 (supporting information), it can be seen that C-PANI charge and discharge faster than C-Fe/PANI electrode which suggest that C-Fe/PANI electrode has a better charge storing capacity signifying that Fe in C-Fe/PANI enhance electrochemical performance of the electrode.

In addition, the EIS was carried out to evaluate the factors that influence the capacitive performance of the working electrodes such as the electronic resistance of the electrode, an ionic resistance of the electrolyte, the charge-transfer resistance of redox reactions and the diffusive resistance of the electrode in the electrolyte. The EIS was carried out in an open circuit potential and the frequency range of 10–100 mHz. To evaluate the cycling performance of the electrodes, the electrodes were subjected to 1000 cycles at a current density of 5 A g^{-1}, as shown in Fig. 6(a). It can be seen that the electrodes show good cycle stability with 100% columbic efficiency up to 1000 charge-discharge cycles, signifying good electrochemical stability of the electrodes. Fig. 6(b) shows the Nyquist plot (imaginary component, Z'' versus the real component, Z' of the impedance) for VS_2 before and after stability test. As it can be seen from the plot, VS_2 electrode shows electrolyte/solution resistance, R_S value of 0.60 Ω and 0.63 Ω (see inset figure) before and after

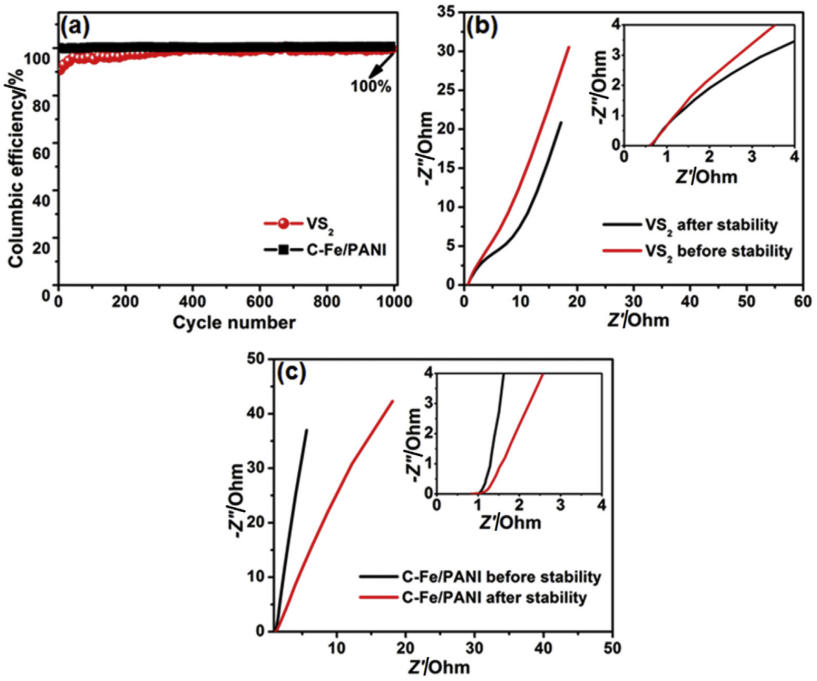

Fig. 6. (a) The cycling performance of the VS_2 and C-Fe/PANI electrodes at a current density of 5 A g^{-1}. The Nyquist plots for the (b) VS_2 and (c) C-Fe/PANI electrodes, before and after cycling. The insets show the enlarged high-frequency region of the plots.

stability respectively. The observed R_S values before and after cycling stability test are almost equal, hence confirming the good chemical stability of the electrode. For C-Fe/PANI electrode, the Nyquist plot is also shown in Fig. 6(c), and the R_S values are 0.94 Ω and 0.86 Ω before and after stability respectively which are almost equal confirming the good chemical stability of the electrode. Briefly, the VS_2 and C-Fe/PANI electrodes show good cycling stability at a high current density of 5 A g^{-1} with 100% columbic efficiency up to 1000 charge-discharge cycles suggesting that continuous cycling does not cause any structural change on the two electrode materials.

In order to fully explore the electrochemical performance of the VS_2 and C-Fe/PANI electrodes, a two-electrode asymmetric device based on VS_2 as cathode and C-Fe/PANI as anode was fabricated and investigated by a two-electrode system using 6 M KOH electrolyte (Fig. 7(a)). Due to the difference in the specific capacity of the two electrodes (Fig. 5(f)), a charge balance, $Q_+ = Q_-$ was done, where Q_+ and Q_- are charge stored in both positive and negative electrodes respectively, expressed as $Q = C_S m \Delta V$. The charge balance is necessary in order to acquire the optimal performance of the device. Based on charge balancing, the mass balance between the positive and negative electrode can be expressed using the following equation [40]:

$$\frac{m_+}{m_-} = \frac{C_{S(-)} \times V_-}{C_{S(+)} \times V_+} \tag{3}$$

where $C_{S(+)}$ and $C_{S(-)}$ are the specific capacitance of the active materials in positive and negative electrodes respectively, m_+ and m_- are the masses of the active materials in positive and negative electrodes and V_+ and V_- are the potential window of the positive and negative electrodes respectively.

Fig. 7(b) shows the CV curves of both VS_2 and C-Fe/PANI electrodes at a scan rate of 50 mV s^{-1} evaluated in three-electrode. Since the C-Fe/PANI electrode has a potential window range of 0.0 to −1.2 V and VS_2 of 0.0–0.5 V, the CV curves of VS_2//C-Fe/PANI asymmetric cell was able to reach potential window range of 0.0–1.7 V, as shown in Fig. 7(c) and (d). Fig. 7(c) shows the CV curves of the device in the potential window of 0.0–1.2 and 0.0–1.7 V both at a scan rate of 50 mV s^{-1}. The figure clearly illustrates the EDLC and faradic behavior of the device. It can be seen that the EDLC contribution has equivalent positive and negative currents (i.e. anodic and cathodic reactions), however, the faradic contribution shows much higher positive current (anodic reactions) compared to EDLC contribution suggesting that the contribution of the positive electrode (VS_2) to the overall current of the device dominates. Consequently, the device has predominantly a battery-like behavior. The CV curves of the device at different scan rates in the range of 5–100 mV s^{-1} are shown in Fig. 7(d). It can be seen that the CV curves at different scan rates display a combined contribution of EDLC and faradic behaviors which is a typical behavior of hybrid asymmetric supercapacitor. In addition, the GCD curves at different current densities in the range of 2–5 A g^{-1} (Fig. 7(e)) show potential steps which confirm the faradic behavior of the device as suggested by CV curves (Fig. 7(d)). Since the device shows mostly faradic behaviour, the specific capacity of the device was calculated from the GCD curves using Equation (2) and found to be 19, 10, 7, and 5 mA h g^{-1} at current densities of 2.0, 3.0, 4.0 and 5.0 A g^{-1} respectively (Fig. 7(f)). The observed drop in specific capacity with increasing current density could be due to the limited movement of ions by diffusion accessing only the outer surface of the material for charge storage at higher current density [55]. The observed drop in specific capacity values for fabricated device compared to three-electrode measurements, may be due to the

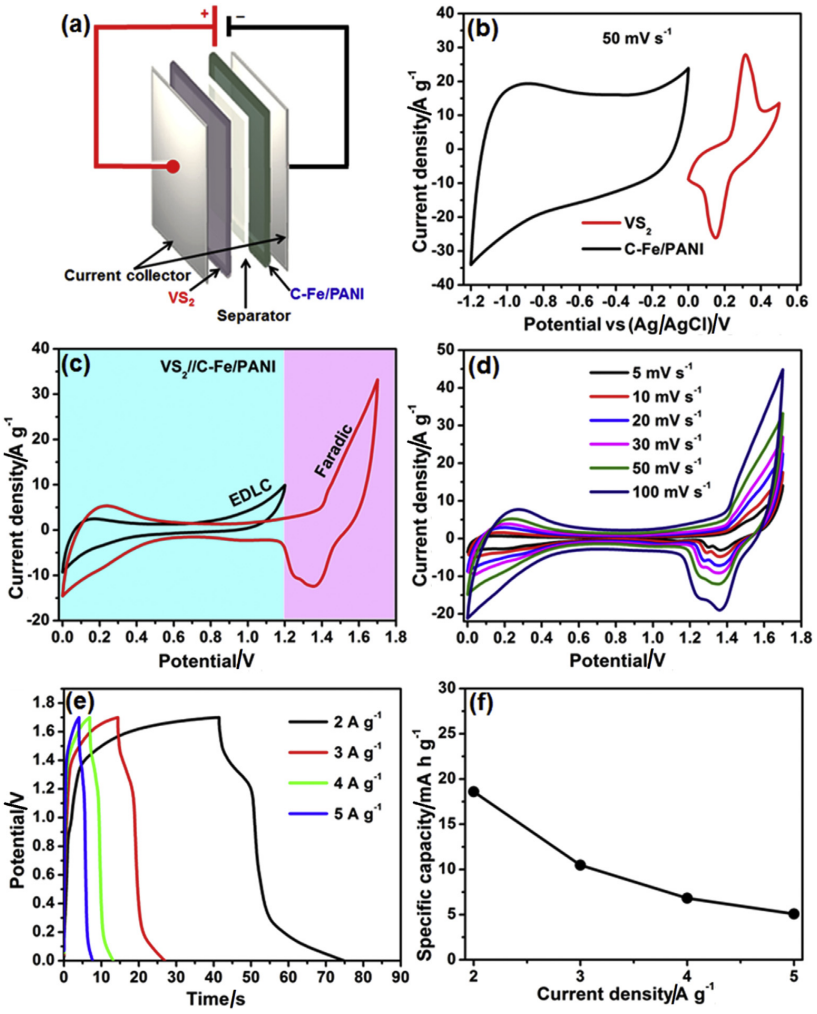

Fig. 7. (a) Schematic illustration of the fabricated asymmetric supercapacitor based on VS_2 as a cathode and C-Fe/PANI as an anode in 6 M KOH aqueous electrolyte. (b) CV curves of both VS_2 and C-Fe/PANI electrodes at a scan rate of 50 mV s^{-1} evaluated in three-electrode. For the asymmetric VS_2//C-Fe/PANI device: (c) CV at scan rates of 50 mV s^{-1} in the potential window of 0.0–1.2 and 1.7 V, (d) CV curves at different scan rates in the range of 5–100 mV s^{-1}, and (e) CD curves at different current densities in the range of 0.5–10 A g^{-1}, (f) the specific capacity as the as a function of current density.

increasing electronic field within the cell setup (operated in a high potential window), increased by an increase in current density which alters the synergy of Faradic and EDLC processes. Similar behavior for the VS_2-based device can be observed in Ref. [37], for instance, from the GCD curves of the VS_2//AC device the specific capacity at current densities of 1.0, 2.0 and 5.0 A g^{-1} are 40, 22 and 15 mA h g^{-1}, respectively.

Moreover, the energy density, E_d (W h kg^{-1}) and the power density, P_d (W kg^{-1}) were calculated from the GCD curves, as shown in Fig. 8(a), using the following equations:

$$E_d = \left(\frac{I}{m}\right)\frac{\int V(t)dt}{3.6} \quad (4)$$

$$P_d = \frac{3.6\ E_d}{\Delta t} \quad (5)$$

where I is the applied current (A), m is the total mass of the active material (g), $\int V(t)dt$ is the integral under the discharge curve from CD of the device, and Δt is the discharge time (s).

The VS_2//C-Fe/PANI asymmetric device exhibited highest energy and power densities of 27.8 W h kg^{-1} and 2991.5 W kg^{-1} respectively at a current density of 2 A g^{-1}. Fig. 8(a) shows the Ragone plot of the device which describes the relationship between energy density and power density, including the energy and power density regions for lithium ion batteries (faradic behavior) and electrochemical capacitors (EDLC behavior). Ragone plot clearly shows that the energy densities for VS_2//C-Fe/PANI asymmetric device are close to the upper end of lithium Ion batteries' region confirming a

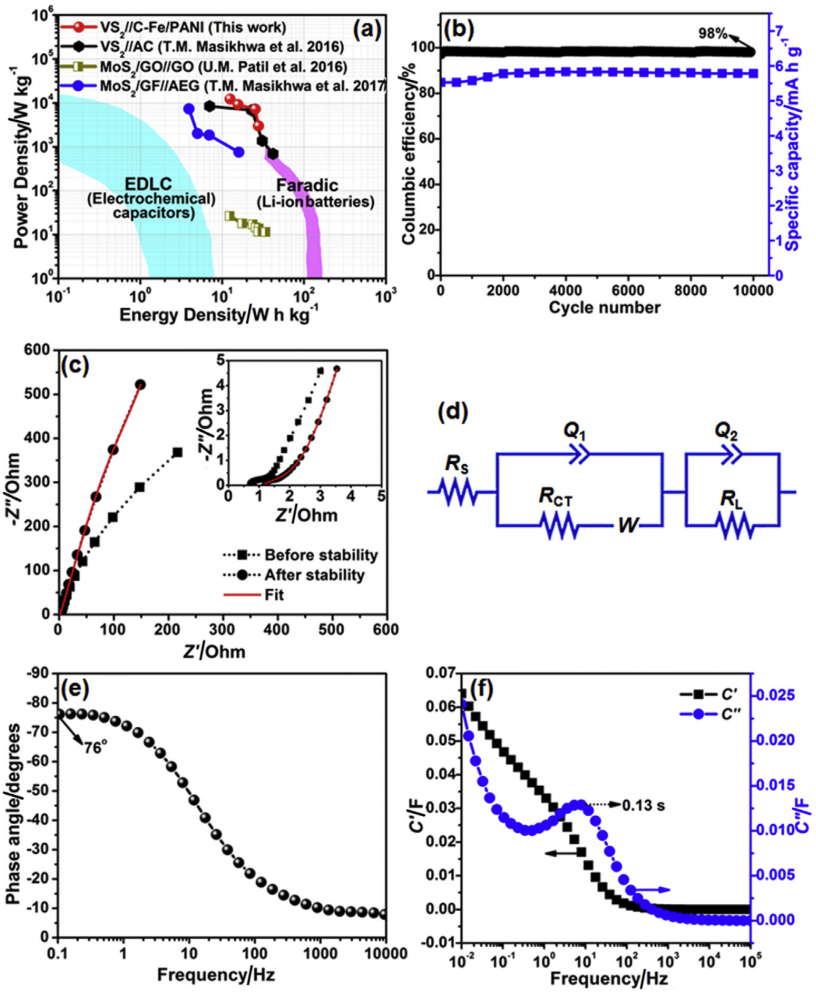

Fig. 8. (a) Ragone plot of the VS_2//C-Fe/PANI asymmetric device showing the relationship between energy and power densities, including the energy and power density regions for lithium ion batteries (Faradic behavior) and electrochemical capacitors (EDLC behavior). (b) The columbic efficiency and the capacity retention and as a function of a cycle number for the device at a current density of 5 A g^{-1}. (c) The Nyquist plots before and after cycling stability of the device (the insets show the enlarged high-frequency region of the plots). (d) The equivalent circuit diagram used to fit the Nyquist plot after stability in (c) (i.e. a red solid-line). (e) The phase angle versus frequency. (f) The real and imaginary plot of capacitance as a function of frequency. (For interpretation of the references to colour in this figure legend, the reader is referred to the web version of this article.)

battery-like behavior of the device. As shown in the Ragone plot, the values obtained in this work are comparable with those found in the previously published report on VS_2//AC asymmetric device [37] and superior to those reported on other metal disulfide based asymmetric devices [56,57].

Fig. 8(b) shows the stability test of the device which reveals an excellent cycling stability with a columbic efficiency of 98% and retains 95% of its initial capacity up to 10 000 cycling at a current density of 5 A g^{-1}. To further evaluate the electrochemical behavior of the device (i.e., the conductivity and charge transport properties at the electrode/electrolyte interface), the EIS of the VS_2//C-Fe/PANI asymmetric device before and after cycling stability was carried out (Fig. 8(c)). In Fig. 8(c), the Nyquist plots (imaginary component, Z'' versus the real component, Z' of the impedance) show negligible semi-circle in the high-frequency region and in the low-frequency region the plots show a linear component almost parallel to the imaginary axis (y-axis) suggesting nearly ideal behavior of the asymmetric supercapacitor. The Nyquist plots before and after cycling stability are comparable (also see the inset figure) confirming the good chemical stability of the device. The plot after stability was fitted (see a red solid-line in Fig. 8(c)) using the equivalent circuit diagram shown in Fig. 8(d). In the high-frequency region, the equivalent circuit diagram presents the equivalent series (solution) resistance, R_S in series with the charge transfer resistance, R_{CT}, and Warburg impedance characteristic element, W, which can be expressed as $W = A/(j\omega)^{0.5}$, where A is the Warburg coefficient, ω is the angular frequency parallel to the real capacitance (Q_1) [58]. The R_S and R_{CT} values represent the ohmic resistance of the electrodes and the charge-transfer kinetics (fast ion transport) respectively. In the low-frequency region, an ideal

supercapacitor exhibits a vertical line parallel to the imaginary axis with a mass capacitance, Q_2, however, in practice supercapacitors show deviation from this ideal behavior which is attributed to a leakage resistance, R_L arising from the faradaic charge transfer process [59,60]. In the equivalent circuit, R_L is parallel to the Q_2. The R_S and R_{CT} values before stability ($R_S = 0.73\ \Omega$ and $R_{CT} = 0.61\ \Omega$) and after stability ($R_S = 1.10\ \Omega$ and $R_{CT} = 0.56\ \Omega$) are small and similar signifying fast ion diffusion and low charge transfer resistance, hence suggesting nearly an ideal capacitive performance of the device and good chemical stability of the electrodes.

Fig. 8(e) shows the impedance phase angle dependence on a frequency Bode plot for the VS_2//C-Fe/PANI asymmetric device and presents the phase angle value of about $-76°$ in the low-frequency region, which is close to the ideal value of $-90°$ suggesting a full capacitive behavior of the device. In the low-frequency region, the frequency dependence of the real and imaginary part of the capacitances ($C'(\omega)$ and $C''(\omega)$) was evaluated (Fig. 8(f)) using a complex capacitance model presented by the following equations [61]:

The impedance, $Z(\omega)$ given by

$$Z(\omega) = \frac{1}{j\omega \times C(\omega)} \tag{6}$$

can be written in the complex form as

$$Z(\omega) = Z'(\omega) + jZ''(\omega) \tag{7}$$

Therefore, Equations (6) and (7) gives:

$$\begin{aligned} C(\omega) &= \frac{1}{\omega \times (jZ'(\omega) - Z''(\omega))} \\ &= \frac{-(Z''(\omega) + jZ'(\omega))}{\omega|Z(\omega)|^2} \end{aligned} \tag{8}$$

Thus, $C(\omega)$ in the complex form can be written as:

$$C(\omega) = C'(\omega) - jC''(\omega) \tag{9}$$

which gives

$$C'(\omega) = \frac{Z''(\omega)}{\omega|Z(\omega)|^2} \tag{10}$$

$$C''(\omega) = \frac{Z'(\omega)}{\omega|Z(\omega)|^2} \tag{11}$$

where Z' and Z'' are the real part and the imaginary part of the impedance, respectively, defined as

$$|Z(\omega)|^2 = Z'(\omega)^2 + Z''(\omega)^2 \tag{12}$$

and $\omega = 2\pi f$. $C'(\omega)$ is the real accessible capacitance of the cell that can be delivered and this corresponds to the deliverable capacitance of 0.065 F (Fig. 8(f)). $C''(\omega)$ corresponds to energy loss by the irreversible process of the electrodes [61]. In Fig. 8(f), $C''(\omega)$ shows a peak at 8.0 Hz giving a relaxation time of 0.13 s which is obtained by taking reciprocal of maximum frequency. This value reveals that the VS_2//C-Fe/PANI asymmetric device can be fully charged within a very short time.

4. Conclusion

In this work, VS_2 nanosheets electrode material was successfully synthesized by the hydrothermal method, and the C-Fe/PANI electrode material was directly synthesized on a current collector by pyrolysis of the iron-PANI mixture coated on nickel foam in a tube furnace under the N_2 atmosphere. The structural and morphological characterization of the as-synthesized VS_2 electrode showed characteristic XRD peaks of VS_2. Furthermore, the Raman and FTIR vibration spectra also showed the characteristic vibration bands of VS_2. The SEM images of the VS_2 sample showed that is composed of a large number of nanosheets. Similarly, the structural and morphological characterization of C-Fe/PANI electrode confirmed diffraction peaks of Fe, Fe_3C, FeS and a broad diffraction peak of graphitized PANI. The Raman and FTIR vibration spectra of C-Fe/PANI revealed features of the graphitized carbon material, PANI functional groups, and Fe—PANI vibration bands. The SEM images of the C-Fe/PANI sample showed agglomerated nanograins. The electrochemical behavior of each working electrode was analyzed in a three-electrode cell configuration using 6 M KOH electrolyte, and thereafter, an asymmetric device was successfully fabricated using VS_2 nanosheets as the positive electrode and C-Fe/PANI as a negative electrode. The fabricated VS_2//C-Fe/PANI asymmetric device was found to perform at a high applied potential difference of 1.7 V in 6 M KOH. At a current density of 2 A g^{-1}, the device exhibited a maximum energy and power densities of 27.8 Wh kg^{-1} and 2991.5 W kg^{-1} respectively. In addition, a VS_2//C-Fe/PANI device showed excellent cycling stability with 95% capacity retention over 10 000 galvanostatic charge-discharge cycles at a current density of 5 A g^{-1}.

Acknowledgements

This work is based on research supported by the South African Research Chairs Initiative (SARChI) of the Department of Science and Technology and the National Research Foundation (NRF) of South Africa (Grant No. 61056). Any opinion, finding and conclusion or recommendation expressed in this material is that of the author(s) and the NRF does not accept any liability in this regard. Mologadi N. Rantho acknowledges the financial support from University of Pretoria and NRF through SARChI in Carbon Technology and Materials.

Appendix A. Supplementary data

Supplementary data related to this article can be found at https://doi.org/10.1016/j.electacta.2017.11.074.

References

[1] G. Feng, S. Li, V. Presser, P.T. Cummings, Molecular insights into carbon supercapacitors based on room-temperature ionic liquids, J. Phys. Chem. Lett. 4 (2013) 3367–3376, https://doi.org/10.1021/jz4014163.
[2] P. Simon, Y. Gogotsi, Materials for electrochemical capacitors, Nat. Mater 7 (2008) 845–854, https://doi.org/10.1038/nmat2297.
[3] K. Zhang, L.L. Zhang, X.S. Zhao, J. Wu, Graphene/polyaniline nanofiber composites as supercapacitor electrodes, Chem. Mater. 22 (2010) 1392–1401, https://doi.org/10.1021/cm902876u.
[4] D.A.C. Brownson, D.K. Kampouris, C.E. Banks, An overview of graphene in energy production and storage applications, J. Power Sources 196 (2011) 4873–4885, https://doi.org/10.1016/j.jpowsour.2011.02.022.
[5] Y. Xie, Z. Song, S. Yao, H. Wang, W. Zhang, Y. Yao, B. Ye, C. Song, J. Chen, Y. Wang, High capacitance properties of electrodeposited PANI-Ag nanocable arrays, Mater. Lett. 86 (2012) 77–79, https://doi.org/10.1016/j.matlet.2012.07.026.
[6] W. Sun, X. Chen, Fabrication and tests of a novel three dimensional micro supercapacitor, Microelectron. Eng. 86 (2008) 1307–1310, https://doi.org/10.1016/j.mee.2008.12.010.
[7] D.P. Dubal, S.V. Patil, W.B. Kim, C.D. Lokhande, Supercapacitors based on electrochemically deposited polypyrrole nanobricks, Mater. Lett. 65 (2011) 2628–2631, https://doi.org/10.1016/j.matlet.2011.05.114.
[8] B.E. Conway, Electrochemical Supercapacitors Scientific Fundamentals and Technological Applications 1999.pdf, Kluwer Academic/Plenum, New York, 1999.

[9] J.R.J. Miller, A.F.A. Burke, Electrochemical capacitors: challenges and opportunities for real-world applications, Electrochem. Soc. Interface 17 (2008) 53.

[10] A. Burke, R&D considerations for the performance and application of electrochemical capacitors, Electrochim. Acta 53 (2007) 1083–1091, https://doi.org/10.1016/j.electacta.2007.01.011.

[11] G. Feng, S. Li, V. Presser, P.T. Cummings, Molecular insights into carbon supercapacitors based on room-temperature ionic liquids, J. Phys. Chem. Lett. 4 (2013) 3367–3376, https://doi.org/10.1021/jz4014163.

[12] X. Rui, H. Tan, Q. Yan, Nanostructured metal sulfides for energy storage, Nanoscale 6 (2014) 9889, https://doi.org/10.1039/C4NR03057E.

[13] G. Zhang, M. Kong, Y. Yao, L. Long, M. Yan, One-pot synthesis of γ -MnS/reduced graphene oxide with enhanced performance for aqueous asymmetric supercapacitors, Nanotechnology 28 (2017), 065402, https://doi.org/10.1088/1361-6528/aa52a5.

[14] D.S. Patil, J.S. Shaikh, S.A. Pawar, R.S. Devan, Y.R. Ma, A.V. Moholkar, J.H. Kim, R.S. Kalubarme, C.J. Park, P.S. Patil, Investigations on silver/polyaniline electrodes for electrochemical supercapacitors, Phys. Chem. Chem. Phys. 14 (2012) 11886–11895, https://doi.org/10.1039/c2cp41757j.

[15] S.K. Mondal, K. Barai, N. Munichandraiah, High capacitance properties of polyaniline by electrochemical deposition on a porous carbon substrate, Electrochim. Acta 52 (2007) 3258–3264, https://doi.org/10.1016/j.electacta.2006.09.067.

[16] H. Mi, X. Zhang, X. Ye, S. Yang, Preparation and enhanced capacitance of core–shell polypyrrole/polyaniline composite electrode for supercapacitors, J. Power Sources 176 (2008) 403–409, https://doi.org/10.1016/j.jpowsour.2007.10.070.

[17] C. Portet, P.L. Taberna, P. Simon, E. Flahaut, C. Laberty-Robert, High power density electrodes for Carbon supercapacitor applications, Electrochim. Acta 50 (2005) 4174–4181, https://doi.org/10.1016/j.electacta.2005.01.038.

[18] M. Sawangphruk, M. Suksomboon, K. Kongsupornsak, J. Khuntilo, P. Srimuk, Y. Sanguansak, P. Klunbud, P. Suktha, P. Chiochan, High-performance supercapacitors based on silver nanoparticle–polyaniline–graphene nanocomposites coated on flexible carbon fiber paper, J. Mater. Chem. A 1 (2013) 9630, https://doi.org/10.1039/c3ta12194a.

[19] K.S. Ryu, K.M. Kim, N.G. Park, Y.J. Park, S.H. Chang, Symmetric redox supercapacitor with conducting polyaniline electrodes, J. Power Sources 103 (2002) 305–309, https://doi.org/10.1016/S0378-7753(01)00862-X.

[20] S. Zhou, H. Zhang, Q. Zhao, X. Wang, J. Li, F. Wang, Graphene-wrapped polyaniline nanofibers as electrode materials for organic supercapacitors, Carbon 52 (2013) 440–450, https://doi.org/10.1016/j.carbon.2012.09.055.

[21] M. Sawangphruk, T. Kaewsongpol, Direct electrodeposition and superior pseudocapacitive property of ultrahigh porous silver-incorporated polyaniline films, Mater. Lett. 87 (2012) 142–145, https://doi.org/10.1016/j.matlet.2012.07.103.

[22] A. Clemente, S. Panero, E. Spila, B. Scrosati, Solid-state, polymer-based, redox capacitors, Solid State Ion. 85 (1996) 273–277, https://doi.org/10.1016/0167-2738(96)00070-7.

[23] A. Sarkar, P. Ghosh, A.K. Meikap, S.K. Chattopadhyay, S.K. ChatterjeeM Ghosh, S.K. Chatterjee, M. Ghosh, Alternate and direct current conductivity of conducting polyaniline dispersed with poly vinyl alcohol and blended with methyl cellulose, J. Appl. Phys. 97 (2005), 113713, https://doi.org/10.1063/1.1923168.

[24] S.S. Umare, B.H. Shambharkar, R.S. Ningthoujam, Synthesis and characterization of polyaniline–Fe_3O_4 nanocomposite: electrical conductivity, magnetic, electrochemical studies, Synth. Met. 160 (2010) 1815–1821, https://doi.org/10.1016/j.synthmet.2010.06.015.

[25] H. Wang, Y. Liang, M. Gong, Y. Li, W. Chang, T. Mefford, J. Zhou, J. Wang, T. Regier, F. Wei, H. Dai, An ultrafast nickel–iron battery from strongly coupled inorganic nanoparticle/nanocarbon hybrid materials, Nat. Commun. 3 (2012) 917, https://doi.org/10.1038/ncomms1921.

[26] Q. Qu, S. Yang, X. Feng, 2D sandwich-like sheets of iron oxide grown on graphene as high energy anode material for supercapacitors, Adv. Mater 23 (2011) 5574–5580, https://doi.org/10.1002/adma.201103042.

[27] Z. Liu, S.W. Tay, X. Li, Rechargeable battery using a novel iron oxide nanorods anode and a nickel hydroxide cathode in an aqueous electrolyte, Chem. Commun. 47 (2011), 12473, https://doi.org/10.1039/c1cc15022g.

[28] B. Yanwu Zhu, S. Murali, W. Cai, X. Li, J. Won Suk, J.R. Potts, R.S. Ruoff, Graphene and graphene oxide: synthesis, properties, and applications, Adv. Mater. 22 (2010) 3906–3924, https://doi.org/10.1002/adma.201001068.

[29] J. Wang, B. Deng, H. Chen, X. Wang, J. Zheng, Removal of aqueous Hg(II) by polyaniline: sorption characteristics and mechanisms, Environ. Sci. Technol. 43 (2009) 5223–5228, https://doi.org/10.1021/es803710k.

[30] J. Zhang, C. Liu, G. Shi, Raman spectroscopic study on the structural changes of polyaniline during heating and cooling processes, J. Appl. Polym. Sci. 96 (2005) 732–739, https://doi.org/10.1002/app.21520.

[31] Y. Tang, T. Chen, S. Yu, Y. Qiao, S. Mu, J. Hu, F. Gao, Synthesis of graphene oxide anchored porous manganese sulfide nanocrystals via the nanoscale Kirkendall effect for supercapacitors, J. Mater. Chem. A 3 (2015) 12913–12919, https://doi.org/10.1039/C5TA02480C.

[32] P.C. Chen, G. Shen, Y. Shi, H. Chen, C. Zhou, Preparation and characterization of flexible asymmetric supercapacitors based on transition-metal-oxide nanowire/single-walled carbon nanotube hybrid thin-film electrodes, ACS Nano 4 (2010) 4403–4411, https://doi.org/10.1021/nn100856y.

[33] Y. Tang, T. Chen, S. Yu, Y. Qiao, S. Mu, S. Zhang, Y. Zhao, L. Hou, W. Huang, F. Gao, A highly electronic conductive cobalt nickel sulphide dendrite/quasi-spherical nanocomposite for a supercapacitor electrode with ultrahigh areal specific capacitance, J. Power Sources 295 (2015) 314–322, https://doi.org/10.1016/j.jpowsour.2015.07.035.

[34] Y. Tang, T. Chen, S. Yu, Morphology controlled synthesis of monodispersed manganese sulfide nanocrystals and their primary application in supercapacitors with high performances, Chem. Commun. 51 (2015) 9018–9021, https://doi.org/10.1039/C5CC01700A.

[35] T. Chen, Y. Tang, Y. Qiao, Z. Liu, W. Guo, J. Song, S. Mu, S. Yu, Y. Zhao, F. Gao, All-solid-state high performance asymmetric supercapacitors based on novel MnS nanocrystal and activated carbon materials, Sci. Rep. 6 (2016), 23289, https://doi.org/10.1038/srep23289.

[36] J. Feng, X. Sun, C. Wu, L. Peng, C. Lin, S. Hu, J. Yang, Y. Xie, Metallic few-layered VS_2 ultrathin nanosheets: high two-dimensional conductivity for in-plane supercapacitors, J. Am. Chem. Soc. 133 (2011) 17832–17838, https://doi.org/10.1021/ja207176c.

[37] T.M. Masikhwa, F. Barzegar, J.K. Dangbegnon, A. Bello, M.J. Madito, D. Momodu, N. Manyala, Asymmetric supercapacitor based on VS_2 nanosheets and activated carbon materials, RSC Adv. 6 (2016), 38990, https://doi.org/10.1039/C5RA27155J.

[38] G.A. Wiegers, Physical properties of first-row transition metal dichalcogenides and their intercalates, Phys. B+C 99 (1980) 151–165, https://doi.org/10.1016/0378-4363(80)90225-9.

[39] M. Zhao, H. Song, Synthesis of carbon-encapsulated iron carbide/iron nanoparticles from phenolic-formaldehyde resin and ferric nitrate, Mater. Chem. Phys. 124 (2010) 861–864, https://doi.org/10.1016/j.matchemphys.2010.08.011.

[40] N. Daems, X. Sheng, Y. Alvarez-Gallego, I.F.J. Vankelecom, P.P. Pescarmona, Iron-containing N-doped carbon electrocatalysts for the cogeneration of hydroxylamine and electricity in a H_2 –NO fuel cell, Green Chem. 18 (2016) 1547–1559, https://doi.org/10.1039/C5GC02197A.

[41] S. Sugai, K. Murase, S. Uchida, S. Tanaka, Studies of lattice dynamics in 2H-TaS_2 by Raman scattering, Solid State Commun. 40 (1981) 399–401, https://doi.org/10.1016/0038-1098(81)90847-4.

[42] W.G. McMullan, J.C. Irwin, Raman scattering from 2H and 3r–NbS_2, Solid State Commun. 45 (1983) 557–560, https://doi.org/10.1016/0038-1098(83)90426-X.

[43] C. Röder, T. Weißbach, C. Himcinschi, J. Kortus, S. Dudczig, C.G. Aneziris, Raman spectroscopic characterization of novel carbon-bonded filter compositions for steel melt filtration, J. Raman Spectrosc. 45 (2014) 128–132, https://doi.org/10.1002/jrs.4426.

[44] S.K. Pradhan, B.B. Nayak, B.K. Mohapatra, B.K. Mishra, Micro raman spectroscopy and electron probe microanalysis of graphite spherulites and flakes in cast iron, Metall. Mater. Trans. A 38 (2007) 2363–2370, https://doi.org/10.1007/s11661-007-9288-1.

[45] Y. Ren, N. Yan, J. Feng, J. Ma, Q. Wen, N. Li, Q. Dong, Adsorption mechanism of copper and lead ions onto graphene nanosheet/δ-MnO_2, Mater. Chem. Phys. 136 (2012) 538–544, https://doi.org/10.1016/j.matchemphys.2012.07.023.

[46] Y. Zhao, H. Ma, S. Huang, X. Zhang, M. Xia, Y. Tang, Z.F. Ma, Monolayer nickel cobalt hydroxyl carbonate for high performance all-solid-state asymmetric supercapacitors, ACS Appl. Mater. Interfaces 8 (2016) 22997–23005, https://doi.org/10.1021/acsami.6b05496.

[47] R. Li, Z. Hu, X. Shao, P. Cheng, S. Li, W. Yu, W. Lin, D. Yuan, Large scale synthesis of NiCo layered double hydroxides for superior asymmetric electrochemical capacitor, Sci. Rep. 6 (2016), 18737, https://doi.org/10.1038/srep18737.

[48] Y. He, J. Pan, L. Wu, Y. Zhu, X. Ge, J. Ran, Z. Yang, T. Xu, A novel methodology to synthesize highly conductive anion exchange membranes, Sci. Rep. 5 (2015), https://doi.org/10.1038/srep13417.

[49] K.O. Oyedotun, M.J. Madito, A. Bello, D.Y. Momodu, A.A. Mirghni, N. Manyala, Electrochimica Acta Investigation of graphene oxide nanogel and carbon nanorods as electrode for electrochemical supercapacitor, Electrochim. Acta 245 (2017) 268–278, https://doi.org/10.1016/j.electacta.2017.05.150.

[50] B. Akinwolemiwa, C. Peng, G.Z. Chen, Redox electrolytes in supercapacitors, J. Electrochem. Soc. 162 (2015) A5054–A5059, https://doi.org/10.1149/2.0111505jes.

[51] A. Laheäär, P. Przygocki, Q. Abbas, F. Béguin, Appropriate methods for evaluating the efficiency and capacitive behavior of different types of supercapacitors, Electrochem. Commun. 60 (2015) 21–25, https://doi.org/10.1016/j.elecom.2015.07.022.

[52] K.O. Oyedotun, M.J. Madito, A. Bello, D.Y. Momodu, A.A. Mirghni, N. Manyala, Investigation of graphene oxide nanogel and carbon nanorods as electrode for electrochemical supercapacitor, Electrochim. Acta (2017), https://doi.org/10.1016/j.electacta.2017.05.150.

[53] G. Godillot, L. Guerlou-Demourgues, P.L. Taberna, P. Simon, C. Delmas, Original conductive Nano-Co_3O_4 investigated as electrode material for hybrid supercapacitors, Electrochem. Solid-State Lett. 14 (2011) A139, https://doi.org/10.1149/1.3609259.

[54] C. Yuan, X. Zhang, L. Su, B. Gao, L. Shen, Facile synthesis and self-assembly of hierarchical porous NiO nano/micro spherical superstructures for high performance supercapacitors, J. Mater. Chem. 19 (2009) 5772–5777, https://doi.org/10.1039/B902221J.

[55] D.Y. Momodu, F. Barzegar, A. Bello, J. Dangbegnon, T. Masikhwa, J. Madito, N. Manyala, Simonkolleite-graphene foam composites and their superior electrochemical performance, Electrochim. Acta 151 (2015) 591–598, https://doi.org/10.1016/j.electacta.2014.11.015.

[56] U.M. Patil, M.S. Nam, S. Kang, J.S. Sohn, H.B. Sim, S. Kang, S.C. Jun, Fabrication

of ultra-high energy and power asymmetric supercapacitors based on hybrid 2D MoS_2/graphene oxide composite electrodes: a binder-free approach, RSC Adv. 6 (2016) 43261–43271, https://doi.org/10.1039/c6ra00670a.

[57] T.M. Masikhwa, M.J. Madito, A. Bello, J.K. Dangbegnon, N. Manyala, High performance asymmetric supercapacitor based on molybdenum disulphide/graphene foam and activated carbon from expanded graphite, J. Colloid Interface Sci. 488 (2017) 155–165, https://doi.org/10.1016/j.jcis.2016.10.095.

[58] Y. Zhou, H. Xu, N. Lachman, M. Ghaffari, S. Wu, Y. Liu, A. Ugur, K.K. Gleason, B.L. Wardle, Q.M. Zhang, Advanced asymmetric supercapacitor based on conducting polymer and aligned carbon nanotubes with controlled nanomorphology, Nano Energy 9 (2014) 176–185.

[59] W. Sun, X. Chen, Preparation and characterization of polypyrrole films for three-dimensional micro supercapacitor, J. Power Sources 193 (2009) 924–929, https://doi.org/10.1016/j.jpowsour.2009.04.063.

[60] H. Li, J. Wang, Q. Chu, Z. Wang, F. Zhang, S. Wang, Theoretical and experimental specific capacitance of polyaniline in sulfuric acid, J. Power Sources 190 (2009) 578–586, https://doi.org/10.1016/j.jpowsour.2009.01.052.

[61] P.L. Taberna, P. Simon, J.F.F. Fauvarque, Electrochemical characteristics and impedance spectroscopy studies of carbon-carbon supercapacitors, J. Electrochem. Soc. 150 (2003) A292–A300, https://doi.org/10.1149/1.1543948.

SUPPORTING INFORMATION

Asymmetric supercapacitor based on vanadium disulfide nanosheets as a cathode and carbonized iron cations adsorbed onto polyaniline as an anode

M. N. Rantho, M. J. Madito, F. O. Ochai-Ejeh and N. Manyala*

Department of Physics, Institute of Applied Materials, SARChI Chair in Carbon Technology and Materials, University of Pretoria 0028, South Africa.

*Corresponding author's email: ncholu.manyala@up.ac.za, Tel.: + (27)12 420 3549; Fax: + (27)12 420 2516

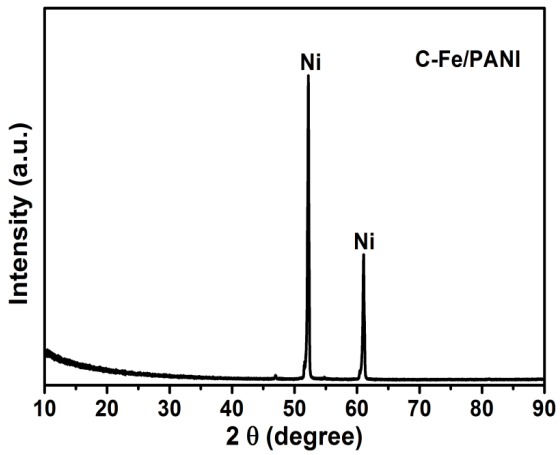

Figure S1. The XRD pattern of the as-synthesized C-Fe/PANI with a current collector.

The EIS for VS_2 in different electrolytes was carried out to evaluate the factors that influence the capacitive performance of the working electrode (i.e. the electronic resistance of the electrode and an ionic resistance of the electrolyte), as shown in figure S2. From the figure, the electrolyte/solution resistance, R_S values are 0.99 Ω and 2.14 Ω for 1 M KOH and 1 M Na_2SO_4 electrolytes, respectively. This reveals that the equivalent series resistance is lower for KOH electrolyte compared to the Na_2SO_4 electrolyte.

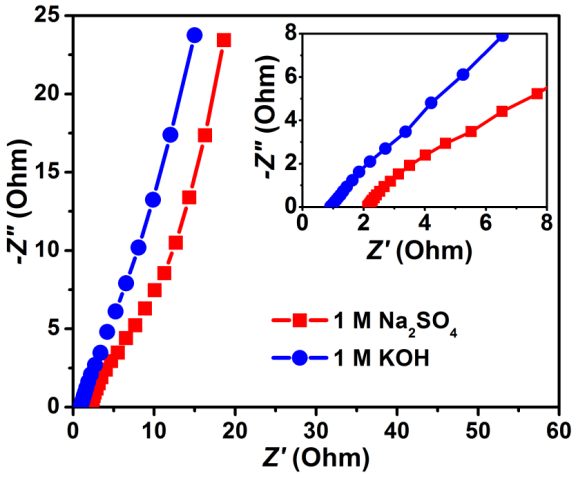

Figure S2. The Nyquist plots for VS_2 in different electrolytes. The inset shows the enlarged high-frequency region of the plot.

Figure S3(a) and S3(b) show the cycling performance of the C-Fe/PANI in comparison to C-PANI over 3000 charge-discharge cycles at a current density of 5 A g^{-1}. Figure S3(a) shows the few cycles for both electrodes and figure S3(b) displays the corresponding specific capacities for both electrodes.

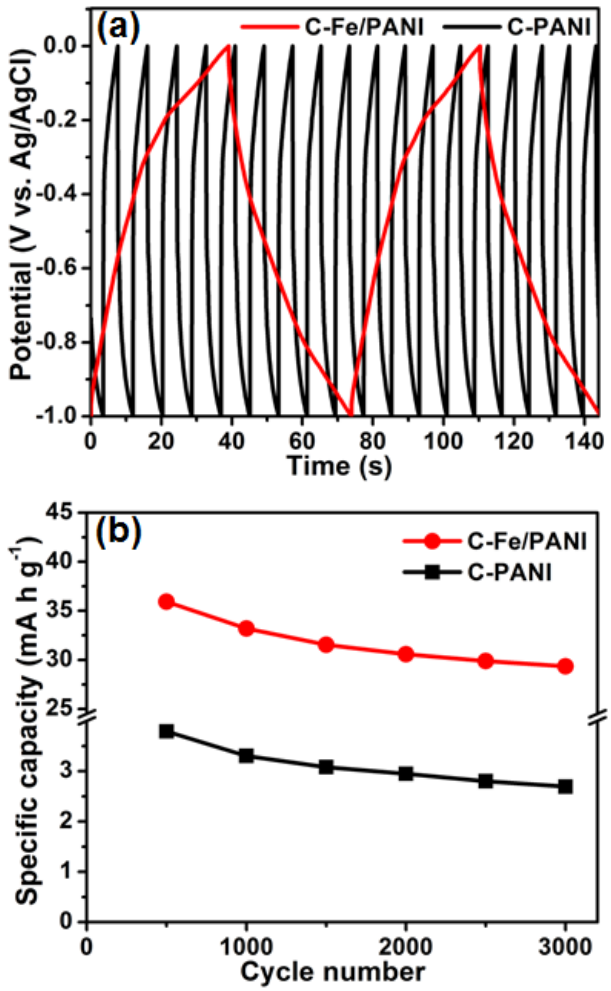

Figure S3. (a) GCD curves of both C-Fe/PANI and C-PANI at 5 A g^{-1}. (b) The specific capacity of both C-PANI and C-Fe/PANI as a function of a cycle number at a current density of 5 A g^{-1}.

Chapter 7

General conclusions and future work

7.1 General conclusions

In this work, the electrochemical properties of both VS_2 and C-Fe/PANI electrode materials were investigated for supercapacitor applications. The VS_2 nanosheets electrode material was successfully synthesized by the hydrothermal method, and the C-Fe/PANI electrode material was directly synthesized on a current collector by pyrolysis of the iron-PANI mixture coated on nickel foam in a tube furnace under the N_2 atmosphere.

The structural and morphological characterization of the as-synthesized electrode materials was carried out using X-ray diffraction (XRD), Raman spectrometer, Fourier transform infrared (FT-IR) spectrometer, scanning electron microscopy (SEM), energy-dispersive X-ray spectrometer (EDS), transmission electron microscopy (TEM) and X-ray photoelectron spectroscopy

(XPS). The XRD analysis of the as-synthesized C-Fe/PANI electrode material confirmed the diffraction peaks of Fe-compounds and a broad diffraction peak of graphitized PANI. The Raman and FTIR vibration spectra of C-Fe/PANI revealed features of the graphitized carbon material, PANI functional groups, and Fe-PANI vibration bands. The SEM images of the C-Fe/PANI sample showed agglomerated nanograins. Additionally, the EDS analysis of the sample confirmed main elements of the sample (Fe and C), TEM images further confirmed the dispersion of Fe on the PANI structure. The XPS analysis confirmed the presence of Fe^{3+} and Fe^{2+} oxidation states in the sample which could be mainly due to iron-carbide, iron-sulfide and iron-nitride configurations. Similarly, the structural and morphological characterization of the as-synthesized VS_2 electrode showed characteristic XRD peaks of VS_2. Furthermore, the Raman and FTIR vibration spectra also showed the characteristic vibration bands of VS_2. The SEM images of the VS_2 sample showed that is composed of a large number of nanosheets. The XPS analysis confirmed the V^{4+} and S^{2-} oxidation states in the VS_2 electrode material revealing the formation of a pure VS_2 phase.

The electrochemical behavior of each working electrode was analyzed in a three-electrode cell configuration using different electrolytes (1 M Na_2SO_4, 1 M Li_2SO_4, 6 M KOH), and 6 M KOH electrolyte was preferred since it showed high current response compared to the other electrolytes. A symmetric device was successfully fabricated using C-Fe/PANI as a positive and negative electrode.

To further evaluate the electrochemical performance of C-Fe/PANI with a metal disulfide material (VS_2), a hybrid (asymmetric) device was successfully fabricated using VS_2 nanosheets as the positive electrode and C-Fe/PANI as a negative electrode. Both devices (symmetric and asymmetric) showed excellent electrochemical performance and the energy and power densities obtained from both devices are comparable with those found in the previously published reports as shown in figure 7.1 and 7.2.

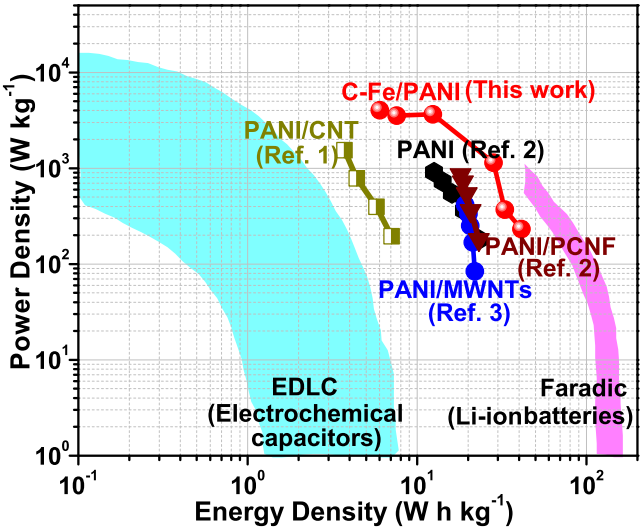

Figure 7.1: Ragone plot of the energy and power densities of the C-Fe/PANI symmetric device and those found in the previously published report on PANI based symmetric devices (PANI/CNT [1], PANI [2], PANI/PCNF [2] and PANI/MWNTs [3]).

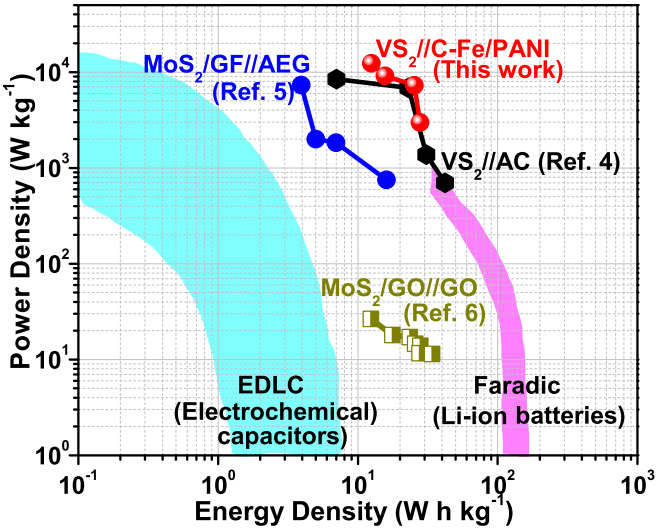

Figure 7.2: Ragone plot of the energy and power densities of the VS_2//C-Fe/PANI asymmetric device and those found in the previously published report on VS_2//AC asymmetric device [4], and metal disulfide based asymmetric devices (MoS_2/GF//AEG [5] and MoS_2/GO//GO [6]).

7.2 Future work

Future research is necessary to further develop and understand the influence of surface chemistry on the electrochemical properties of the electrode materials investigated in this work. The surface chemistry of the electrode materials can be modified by altering or nanostructuring the surface of the electrodes. Additionally, explore new electrolytes and coupled electrolyte additives, which offers an alternative approach for the design of an efficient electrochemical energy storage device that operates over a wide voltage window. Generally, effects of electrode thickness, dimensionality and chemistry among other factors are likely to be significant and need further study [7]. There is relatively little understanding of the self-discharge

mechanisms and how it can be minimized in hybrid devices containing redox electrolytes, particularly, the use of redox electrolytes may lead to faster self-discharge and new approaches to modifying this effect are necessary.

Bibliography

1. S.K. Simotwo, C. Delre, V. Kalra, Supercapacitor Electrodes Based on High-Purity Electrospun Polyaniline and Polyaniline-Carbon Nanotube Nanofibers, ACS Appl. Mater. Interfaces. 8 (2016) 21261-21269. doi:10.1021/acsami.6b03463.

2. M. Dirican, M. Yanilmaz, X. Zhang, S. Mondal, K. Barai, N. Munichandraiah, et al., Free-standing polyaniline-porous carbon nanofiber electrodes for symmetric and asymmetric supercapacitors, RSC Adv. 4 (2014) 59427-59435. doi:10.1039/C4RA09103E.

3. H. Mi, X. Zhang, S. An, X. Ye, S. Yang, Microwave-assisted synthesis and electrochemical capacitance of polyaniline/multi-wall carbon nanotubes composite, Electrochem. Commun. 9 (2007) 2859-2862. doi:10.1016/j.elecom.2007.10.013.

4. T.M. Masikhwa, F. Barzegar, J.K. Dangbegnon, A. Bello, M.J. Madito, D. Momodu, et al., Asymmetric supercapacitor based on VS_2 nanosheets and activated carbon materials, RSC Adv. 6 (2016) 38990-39000.

doi:10.1039/C5RA27155J.

5. U.M. Patil, M.S. Nam, S. Kang, J.S. Sohn, H.B. Sim, S. Kang, et al., Fabrication of ultra-high energy and power asymmetric supercapacitors based on hybrid 2D MoS_2/graphene oxide composite electrodes: a binder-free approach, RSC Adv. 6 (2016) 43261-43271. doi:10.1039/c6ra00670a.

6. G. Wang, L. Zhang, J. Zhang, A review of electrode materials for electrochemical supercapacitors, Chem. Soc. Rev. 41 (2012) 797-828. doi:10.1039/C1CS15060J.